SURFACE ENGINEERING OF ZINC METAL ANODES IN AQUEOUS RECHARGEABLE BATTERIES

YU JINGYA

PhD

The Hong Kong Polytechnic University

2025

The Hong Kong Polytechnic University

Department of Industrial and Systems Engineering

Surface Engineering of Zinc Metal Anodes in Aqueous Rechargeable Batteries

Yu Jingya

A thesis submitted in partial fulfillment of the requirements for the degree

of Doctor of Philosophy

April 2025

CERTIFICATE OF ORIGINALITY

I hereby declare that this thesis is my own work and that, to the best of my knowledge and belief, it reproduces no material previously published or written, nor material that has been accepted for the award of any other degree or diploma, except where due acknowledgement has been made in the text.

_____(Signed)

Yu Jingya (Name of student)

Abstract

Global efforts to lessen the carbon footprint have stimulated the transition from fossil fuels to renewable energy sources and the adoption of electrified transportation. Aqueous zinc ion batteries are regarded one of the most promising next generation battery technologies for safe and low-cost energy storage applications. However, Zn metal anode faces challenges of dendritic deposition, surface passivation and hydrogen evolution in aqueous electrolytes, leading to short cycle life and low Coulombic efficiencies (CEs), particularly at high depth of discharge (DOD). This thesis aims to design a series of reliable artificial interface layers and to investigate their stabilization strategies and reaction mechanisms. This research supports the development of selection criteria for interface materials, which is of considerable significance for enhancing the stability and utilization efficiency of zinc anodes.

Firstly, the MXene-porous polydopamine interfacial layer was designed to engineer the Zn metal surface. The MPP architecture leverages its high density of functional groups to sequester water molecules, thereby mitigating aqueous corrosion of Zn through dual desolvation and anticorrosion mechanisms. Integrated experimental and computational simulations demonstrate that the MPP coating simultaneously reduces nucleation overpotentials, achieves uniform electric field distribution, and regulates Zn^{2+} flux. These synergistic effects promote horizontally aligned, dendrite-free Zn deposition morphology. The optimized MPP-Zn electrodes demonstrate an extended cycle life exceeding 1000 hours (10-fold enhancement versus bare Zn) alongside superior rate performance in both symmetric and asymmetric cell configurations. When paired with $NH_4V_4O_{10}$ cathodes in full-cell assemblies, the MPP-Zn anodes enable a specific capacity of 368 mAh g^{-1} with minimal capacity degradation (<5%) over 300 cycles, electrochemical performance that surpass current benchmarks in Zn-ion battery literature. This multifunctional integration strategy presents a promising pathway toward practical implementation of high-performance Zn metal battery systems.

Secondly, a bifunctional transition metal (TM) interface inspired by the Sabatier principle was constructed, enabling uniform zinc dissolution during discharge and dendrite-free zinc deposition during charge. Among various TM-coated Zn (TM@Zn) electrodes, Cu@Zn exhibits the highest reversibility and structural stability, attributed to the optimal interaction between Cu and Zn. The heteroatomic interaction-dependent electrochemical performance parallels the Sabatier principle. Morphological analyses reveal that bare Zn anodes display detrimental etching pits during stripping, which is different from the uniform dissolution for Cu@Zn electrodes. During subsequent plating, the conductive interface serves as a secondary current collector for uniform Zn deposition for Cu@Zn, thus demonstrating a bifunctional nature. Atomic observations disclose the working mechanisms of this interface as a gradual phase transition from Cu to $CuZn_5$ during cycling. The Cu@Zn anodes exhibit an ultralong cycling lifespan of over 8000 h at a low current of 1 mA cm^{-2} and over 250 h at a high depth of discharge of 80 %. They also demonstrate practical feasibility by maintaining 88.7 % capacity retention after 1000 cycles in Cu@Zn||VO_2 full cells. This work provides new insights into the Sabatier chemistry inspired bifunctional layers for Zn metal battery system.

Thirdly, a bilayer metal interface has been developed, integrating the dual advantages of buffering capacity and uniform zinc ion deposition. As commonly recognized in Zn ion battery research, the prevalent practice of applying excess zinc to maintain continuous active material supply at the anode inevitably results in severely compromised zinc utilization efficiency (<5%). This deliberate overengineering not only introduces substantial material cost penalties but also fundamentally constrains the achievable practical energy density of zinc-ion battery systems. Under electrochemical conditions, a hollow-structured Cu_6Zn_{13} alloy was formed on the electrode surface. This phenomenon differs significantly from scenarios where single-layer metals are employed as buffer layers, which can be attributed to the ultrathin atomic sieve effect exhibited by the Ag interlayer. Owing to the dual protective mechanism, a stable zinc anode is

attained even at high utilization rates. The Cu/Ag@Zn anodes exhibit an ultralong cycling lifespan of over 5500 h at a high current of 5 mA cm^{-2} and over 500 h at a high depth of discharge of 90 %. They also demonstrate practical feasibility by maintaining 84.3 % capacity retention after 1000 cycles in Cu/Ag@Zn||VO_2 full cells. This work proposes a novel strategy to enhance the utilization efficiency of zinc anodes and advance the commercialization of aqueous zinc batteries for large-scale energy storage applications.

This thesis presents a series of research achievements addressing the critical challenges faced by zinc anodes in aqueous zinc-ion batteries. By constructing a multifunctional integrated interfacial layer on the anode surface, a dendrite-free zinc anode has been successfully achieved. Furthermore, guided by the Sabatier principle, this study establishes material selection criteria for optimal interfacial layers. Through rational selection of heterometallic materials, high utilization efficiency of zinc anodes has been realized. These strategies provide fundamental insights and practical solutions for developing high-performance, long-lasting zinc metal batteries.

List of Publications

† Equal contribution first author; * Corresponding author.

1. **J. Yu,** †Z. Song,† Q. Qi, X. Hui, K. Qi, Y. Ma, F. Chen, Q. Meng, R. Li, L. Zhuang, K. C. Chan, Z. Chen, B. Y. Xia, Z.L. Xu*, Sabatier Principle Inspired Bifunctional Alloy Interface for Stable and High-Depth Discharging Zinc Metal Anodes, **Angew Chem. Int. Ed.** 2025, 64, e202423236.

2. **J. Yu,** C. Chen, F. Shi, R. Li, F. Chen, J. Tang, KC Chan, Z.L. Xu*, A multifunctional MXene-porous polydopamine interface for stable and dendrite-free zinc metal batteries, **Energy Storage Mater.**, 2023, 63,102966.

3. **J. Yu,** †Z. Song,† X. Hui, C. Deng, Q. Qi, X. Li, K. Qi, Y. Ma, F. Chen, R. Li, L. Zhuang, K. C. Chan, Z. Chen, B. Y. Xia, Z.L. Xu*, Atomic Sieve-Mediated Bilayer Cu/Ag Interface Enables High-Utilization Zinc Anodes for Stable and Long-Cycling Aqueous Zinc Batteries, submitted.

4.H. Lin,† **J. Yu,**† F. Chen,† R. Li, B.Y. Xia, Z.L. Xu*, Visualizing the Interfacial Chemistry in Multivalent Metal Anodes by Transmission Electron Microscopy, **Small Method.** 2023, 7, 2300561.

5. F. Shi,† **J. Yu,**† C. Chen,† SP Lau, W. Lv, Z.L. Xu.* Advances in understanding and regulation of sulfur conversion processes in metal-sulfur batteries, **J. Mater. Chem. A**, 2022, 10, 19412-19443.

6.Q. Qi,† F. Shi,† **J. Yu**, Y. Ma, F. Chen, W. Lv, W. Law, S. P. Lau*, Z.L. Xu*, Understanding the dynamics of sulfur droplets formation in lean-electrolyte and low-temperature lithium sulfur batteries, **Adv. Sci.** 2024, 12, 2410628.

7. R. Li, **J. Yu**, F. Chen, Y. Su, KC Chan, Z.L. Xu,* High-Power and Ultrastable Aqueous Calcium-Ion Batteries Enabled by Small Organic Molecular Crystal Anodes, **Adv. Funct. Mater.**, 2023, 33, 2214304.

8. F. Chen, **J. Yu,** R. Li, F. Shi, X. Che, K. Chan, Y. Sun, W. Xue, Z.L. Xu* Direct crystallization of deep eutectic solvent into solid-state electrolyte for magnesium metal batteries, **J. Power Sources.** 2024, 611, 234780.

9. Y. Ma, Q. Qi, Q. Meng, Y. Yi, H. Lin, **J. Yu**, C. F. Cheung, Z.L. Xu*, A Small Molecular

Cathode for High-Performance Calcium Metal Batteries, **Adv. Funct. Mater.** 2024, 35, 2411715.

10. R. Li, Y. Lee, H. Lin, X. Che, X. Pu, Y. Yi, F. Chen, **J. Yu**, K. C. Chan, K.-Y. Park, Z.L. Xu*, KxVPO4F (x∼0): a new high-voltage and low-stain cathode material for ultrastable calcium rechargeable batteries, **Adv. Energy Mater.** 2024, 14, 2302700.

11. F. Shi,† X. Guo,† C. Chen, L. Zhuang, J. **Yu, Y**. Zhu, Z.L. Xu*, S.P. Lau, Unlocking liquid sulfur chemistry for fast charging lithium-sulfur batteries, **Nano Lett.**, 2023, 23, 17, 7906–7913.

12. R.T. Liu, Z.L. Xu*, F.M. Li, F.Y. Chen, **J.Y. Yu**, Y. Yan, Y. Chen, B.Y. Xia, Recent Advances in Proton Exchange Membrane Water Electrolysis, **Chem. Soc. Rev.**, 2023, 52, 5652-5683.

13. F. Shi,† L. Zhai,† Q. Liu, **J. Yu**, SP Lau,* B.Y. Xia,* Z.L. Xu.* Emerging catalytic materials for practical lithium sulfur batteries, **J. Energy Chem.**, 2022, 76, 127-145.

Conference

1. **Yu, J.**, Xu, Z. L.*, A Multifunctional Mxene-Based Material for High-Performance Aqueous Zinc Batteries, 243rd ECS Meeting, Boston, USA, May 2023, poster.

2. **Yu, J.**, Xu, Z. L.*, Heterointerfaces chemistry of transition metal shielded zinc anode for high performance aqueous zinc batteries, 245th ECS Meeting, San Francisco, USA, May 2024, oral presentation.

3. **Yu, J.**, Xu, Z. L.*, Interface modification of zinc anode for high performance aqueous zinc batteries, 22nd National Electrochemical Congress In 2024, Hainan, China, November 2024, oral presentation.

Table of Contents

List of Figures

List of Tables

Acknowledgements

Time flies, and in the blink of an eye, my four-year doctoral journey is drawing to a close. Yet I still vividly remember the joy of receiving my admission letter. When I first arrived in Hong Kong during the COVID-19 pandemic, my heart brimmed with both anticipation and anxiety as I ventured far from home to pursue studies in the South. The new research direction and unfamiliar living environment weighed heavily on me. I recall that when I joined the research group, our team was small and the laboratory was still in its infancy. Together with fellow group members, we set up equipment, purchased essential laboratory supplies, and completed various certification trainings. Many challenges required self-directed learning, and I am grateful for this period that accelerated my growth.

First and foremost, I extend my heartfelt gratitude to my Chief Supervisor, Professor Zhenglong Xu. During the initial stages of my doctoral research when progress was challenging and obstacles frequent, his academic guidance and patient encouragement enabled me to maintain perseverance. His support ultimately inspired my decision to continue pursuing scientific research.

I am deeply thankful to all group members whose kindness and enthusiasm motivated me throughout this journey. Special appreciation goes to Dr. Fangyi Shi, whose assistance during my early days in the group brought warmth and encouragement when I faced significant difficulties. My sincere thanks also go to Dr. Chunhong Chen, Dr. Renjie Li, Ms. Feiyang Chen, Dr, Lyu Linlong, Dr. Yuyang Yi, Dr. Xiangjun Pu, Ms. Huijun Lin, Mr. Yingkau Hua, Mr. Pengyan Jiang, Dr. Xiaobin Hui, Dr. Guocheng Li, Mr. Qi Meng, Ms. Chuheng Cao, Dr. Dongjun Li, and Mr. Mengcheng Wu for their professional and academic support. I gratefully acknowledge my collaborator Mr. Zizheng Song for his substantial contributions to my research. Particular recognition is owed to Ms. Qi Qi and Ms. Yiyuan Ma, who witnessed and

accompanied me through numerous challenges, enriching my daily life with their steadfast companionship.

I also wish to thank the scientific officers from the Department of Industrial and Systems Engineering and the university's research facility for materials characterization and device fabrication, whose expertise proved invaluable during sample analysis.

My profound gratitude extends to my parents and family for their unwavering support that allowed me to focus fully on my research. To my friends – thank you for your companionship and understanding throughout these years. Finally, I acknowledge my resilient self for maintaining self-belief when confronting adversities. May I continue to face the future with optimism and perseverance.

Chapter 1 Introduction

1.1 Background

The rapid development of human society cannot be separated from the consumption of fossil resources such as oil, natural gas and coal. Presently, fossil fuels remain the predominant source of global energy supply. However, as society progresses, we are confronted with the gradual depletion of these resources and escalating environmental pollution. Furthermore, the extensive consumption of fossil fuels results in significant carbon dioxide emissions, exacerbating the greenhouse effect and contributing to global warming[1, 2]. The significant reduction in fossil energy reserves, coupled with increasing environmental concerns, has catalyzed the development of renewable and clean energy sources, such as wind, solar, and tidal energy. Concurrently, the demand for efficient and reliable power storage systems is on the rise[3]. Prominent forms of green secondary energy include solar energy, wind energy, and chemical energy. While renewable energy sources like solar and wind offer advantages such as being clean and safe, they also present challenges related to storage and transportation. Additionally, their effectiveness is often contingent upon geographical and climatic conditions[4-6]. Chemical energy stands out due to its high energy density, safety, efficiency, and accessibility, rendering it a prominent subject of contemporary research. Consequently, the development of innovative energy storage devices is essential to ensure a stable energy supply for individuals, households, and businesses.

Propelled by superior energy density and cycle life, lithium-ion batteries (LIBs) have become the cornerstone technology for portable electronics. This momentum is extending their application into the realm of electric and hybrid vehicles[7]. However, the limited availability of lithium resources poses significant challenges for lithium-ion batteries (LIBs) in meeting the anticipated future market demand[8]. Additionally, the issue of dendrite formation on lithium

cathodes can lead to battery short-circuiting, potentially resulting in the combustion and explosion of organic electrolytes, thereby compromising safety performance[9]. Sodium and potassium, both abundant and inexpensive, share similar chemical properties with lithium, positioning organic sodium and potassium batteries as promising alternatives to lithium-ion batteries. Nonetheless, the use of organic electrolytes presents inherent safety challenges that remain difficult to fully resolve[10-12]. Aqueous batteries are electrochemical energy storage systems that utilize a water-based electrolyte in place of an organic electrolyte. Organic electrolytes are toxic and flammable, posing significant safety risks. Moreover, their assembly requires stringent anhydrous conditions, which contribute to increased production complexity and costs. Aqueous batteries offer a significant competitive advantage due to their use of a water-based electrolyte. Their primary benefits include: (1) Cost-effectiveness, as they do not require anaerobic and dry assembly lines, resulting in reduced electrolyte and manufacturing expenses[13]; (2) Environmental friendliness, being non-toxic and non-flammable due to the non-volatile nature of water; (3) Superior ionic conductivity of the water-based electrolyte (~1 S cm^{-1}), which is two orders of magnitude higher than that of non-aqueous electrolytes (~1-10 mS cm^{-1}), facilitating rapid charging and high power density[14]; (4) High resilience to electrical and mechanical mishandling, allowing for rapid discharge, bending, cutting, and cleaning without catastrophic consequences[15]. The lead-acid battery, invented in 1859 by French physicist Gaston Planté, remains widely used in automotive power supply accessories, low-speed electric vehicles, and backup power supplies due to its affordability, safety, and stable performance[16]. However, lead-acid batteries convert chemical energy into electrical energy through reactions between electrode materials and the electrolyte, resulting in an energy

density typically around 30 Wh kg^{-1}. This low energy density limits their suitability for deep discharge and high-current charging, thereby constraining their application in large-scale energy storage systems[17]. Additionally, the use of heavy metals such as lead and sulfuric acid in these batteries poses significant environmental pollution risks. Consequently, the development of environmentally friendly, long-lasting aqueous batteries with energy densities comparable to or exceeding those of lead-acid batteries holds substantial value and significance. Based on the valence states of different metals, aqueous batteries can be divided into two categories: aqueous alkali metal ion batteries (including aqueous lithium, aqueous sodium, and aqueous potassium ion batteries) and aqueous multivalent ion batteries (including aqueous zinc ion batteries, aqueous calcium ion batteries, aqueous magnesium ion batteries, and aqueous aluminum ion batteries). The development of rechargeable aqueous lithium-ion batteries began in 1994, marked by the pioneering work of the Dahn Jeff group, who reported on the VO_2//$LiMn_2O_4$ aqueous lithium-ion battery utilizing the lithium-ion intercalation/deintercalation mechanism[18]. The battery system operates at an average voltage of 1.5 V, maintaining a capacity retention of 80% after 100 cycles. Since this initial development, various aqueous electrolytes, including $LiNO_3$ and Li_2SO_4 solutions, have been explored. Additionally, a range of positive electrode materials, such as manganese oxides, layered oxides, polyanionic compounds, and Prussian blue derivatives, have been investigated. Similarly, negative electrode materials, including vanadium-based compounds, polyanionic materials, and organic electrodes, have been reported in succession[19]. Despite numerous studies, the issue of capacity decline in aqueous lithium-ion batteries remains a significant challenge, hindering their development. Given the limited reserves of lithium salts in the Earth's crust, sodium and potassium present more attractive options for large-scale energy storage due to their greater abundance. However, the large cationic radii of sodium and potassium

compounds make it difficult to identify suitable electrode materials that can effectively pair with these elements[20]. New opportunities are arising in the field of aqueous metal batteries that utilize multivalent metal ions as charge carriers (such as Zn^{2+}, Mg^{2+}, Ca^{2+}, and Al^{3+}). As shown in Figure 1.1[21], these ions are attractive not only due to their abundance in the Earth's crust but also because of their enhanced safety and high energy density. However, the advancement of magnesium, calcium, and aluminum-based aqueous batteries has been impeded by the formidable challenge of accommodating their large solvated cations. Furthermore, the reversibility of magnesium, calcium, and aluminum has proven to be suboptimal. In contrast to these metals, zinc exhibits excellent tolerance to oxygen and water, coupled with a high volumetric specific capacity (5855 mAh cm^{-3}), a low redox potential (-0.76 V versus the standard hydrogen electrode), abundant reserves, and environmental friendliness. These attributes make zinc an ideal candidate for direct use as an anode in aqueous zinc-ion batteries[22]. These advantages have facilitated remarkable advancements in aqueous zinc-ion batteries (AZBs) in recent years, positioning them as promising candidates for large-scale electronic energy storage.

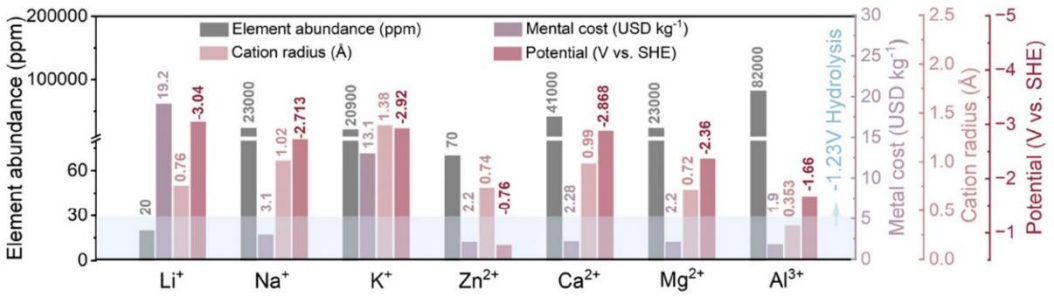

Figure 1.1 Comparison of element abundance, metal cost, cation radius and potential of the typical metal-ion carriers[21].

1.2 Basics of aqueous zinc ion batteries

The development of aqueous zinc-ion batteries has a long and storied history, shown in Figure 1.2. In 1800, the Italian scientist Alessandro Volta invented the world's first chemical battery, the Voltaic pile, which consisted of alternating layers of silver and zinc discs separated by

sheets of paper or cloth soaked in saltwater. This invention laid the groundwork for the use of metallic zinc in batteries. Subsequently, John Daniell invented the zinc-copper battery, in which zinc metal was immersed in zinc sulfate solution as the negative electrode, and copper metal was placed in copper sulfate solution as the positive electrode, connected by a salt bridge to form a primary cell. This invention led to the zinc-copper battery being commonly referred to as the Daniell cell[23]. The world's first zinc-manganese battery was invented in 1866, utilizing zinc as the negative electrode and manganese dioxide distributed on carbon rods as the positive electrode, with a viscous ammonium chloride solution serving as the electrolyte. The advent of zinc-manganese batteries marked a significant advancement in battery technology. Subsequent modifications by researchers have led to the development of the alkaline zinc-manganese batteries commonly used today[24, 25]. In 1986, Shoji et al. developed a zinc-manganese dioxide battery system operating in a mild zinc sulfate electrolyte[26]. Subsequently, in 2012, Kang et al. first proposed the concept of "Zinc-Ion Batteries" (abbreviated as ZIB), a technology enabling reversible zinc-ion insertion and extraction in manganese dioxide (MnO_2)[27]. As research has advanced, an increasing number of storage mechanisms have been proposed, offering theoretical support for the application of aqueous zinc-ion batteries.

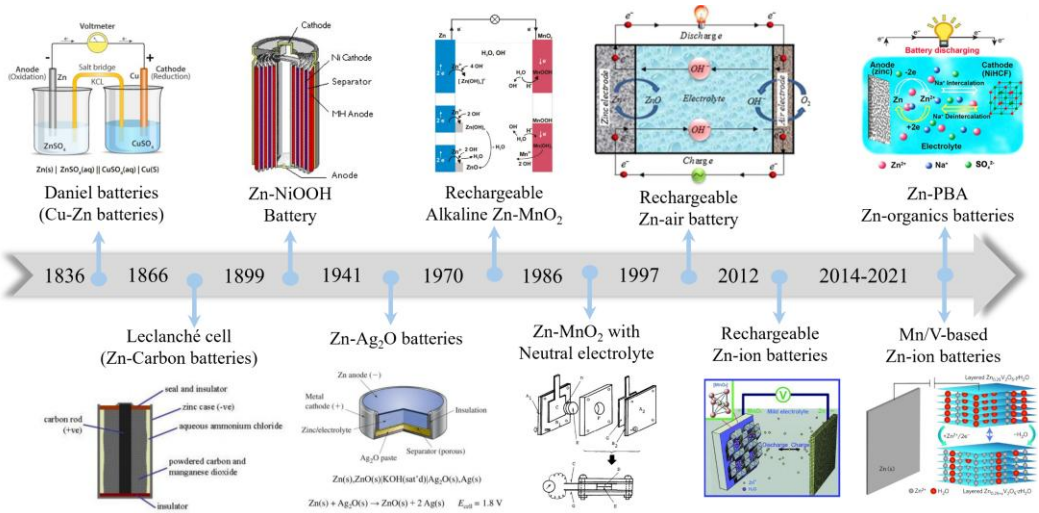

Figure 1.2 History of zinc-based batteries.

1.2.1 The working principle of aqueous zinc ion batteries

Aqueous zinc-ion batteries comprise four primary components: the cathode material, zinc electrode, aqueous electrolyte, and separator. The cathode material includes the active material, conductive agent, and binder, which are uniformly coated onto the current collector. The anode typically consists of zinc foil of varying thicknesses or metallic zinc deposited on flexible conductive substrates. The electrolyte is generally an aqueous solution containing dissolved zinc sulfate or zinc trifluoromethanesulfonate, while gel-like electrolytes are employed in flexible cells. Current research on separators is focused on materials such as glass fibers, with Zn-Nafion membranes also being utilized in zinc-ion batteries. These separators usually possess a microporous structure that permits the free passage of ions while preventing electron flow. Similar to lithium-ion batteries, aqueous rechargeable zinc-ion batteries (AZIBs) are also referred to as "rocking-chair batteries." Figure 1.3 illustrates the structure and operational mechanism of these devices[28]. During discharge, Zn^{2+} ions are stripped from the anode and intercalated into cathode materials, such as α-MnO_2, through a glass fiber or cellulose separator. Conversely, during charging, Zn^{2+} ions are extracted from the cathode material and deposited onto the surface of the zinc anode. The electrolyte typically consists of a neutral or slightly acidic metal salt containing Zn^{2+} ions, which shuttle between the cathode and anode to complete the circuit and achieve energy storage. The specific reaction mechanism can be expressed as follows:

$$\text{Cathode:}\quad Zn^{2+}(aq) + 2e^- + 2\alpha\text{-}MnO_2 \leftrightarrow ZnMn_2O_4 \tag{1-1}$$

$$\text{Anode:}\quad Zn\ (s) \leftrightarrow Zn^{2+}(aq) + 2e^- \tag{1-2}$$

$$\text{Overall Reaction:}\quad Zn\ (s) + 2\alpha\text{-}MnO_2 \leftrightarrow ZnMn_2O_4 \tag{1-3}$$

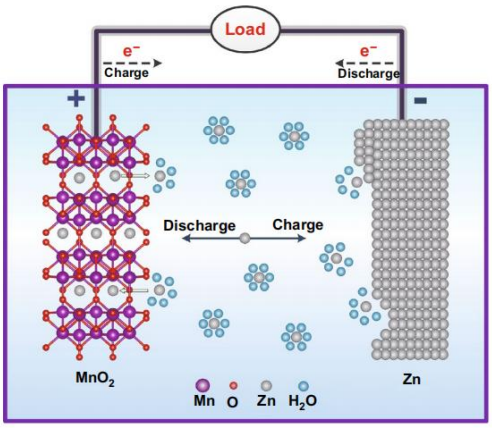

Figure 1.3 Aqueous zinc ion battery working mechanism simulation diagram[29].

1.2.2 Electrode materials for aqueous Zn ion batteries

Anode Material:

After decades of persistent research, the electrochemical performance of cathode materials in aqueous zinc-ion batteries has significantly improved. However, the practical application of anode materials remains in its nascent stages due to an incomplete understanding of the anode reaction mechanisms and inherent issues associated with the zinc anode itself. These challenges have emerged as bottlenecks, impeding the commercialization of aqueous zinc-ion batteries[30]. Zinc ion battery anode materials can be broadly categorized based on the electrochemical behavior of zinc ions during the charging and discharging processes. These categories include zinc metal anodes, which facilitate zinc ion deposition and dissolution, and zinc ion intercalation anodes, which enable ion insertion and extraction. Among these, zinc metal is the most extensively studied and commonly utilized anode material in zinc ion batteries.

Zinc Metal Anode: Metallic zinc (Zn) is considered an excellent anode material for aqueous batteries due to its high theoretical specific capacity of 820 mAh g^{-1}, low redox potential (-0.762 V compared to the standard hydrogen electrode), high abundance, low toxicity, and the inherent safety provided by its aqueous nature[31]. Most importantly, the low cost of zinc and its significantly higher abundance in the Earth's crust compared to lithium are key factors

driving the considerable interest in zinc-ion batteries. Researchers often employ zinc foil directly as the zinc anode; however, zinc foil's limited specific surface area fails to ensure sufficient contact with the electrolyte. Additionally, the uneven deposition of zinc ions on the surface of the zinc metal cathode can result in dendrite formation and side reactions, thereby reducing the battery's discharge capacity and coulombic efficiency[32, 33]. Therefore, uniform plating/stripping of zinc ions in the zinc cathode is important for battery performance and cycle life.

The highly reversible deposition and dissolution behavior of zinc metal can be effectively achieved in neutral or mildly acidic solutions. For energy storage applications, the cathode material is paired with zinc metal[34]. The reaction mechanism of zinc anodes in aqueous zinc-ion batteries (ZIBs) involves the reversible plating and stripping of zinc ions on the electrode, analogous to the processes observed in lithium-ion batteries (LIBs)[30]. As illustrated in Figure 1.4a, zinc ions can rapidly and reversibly dissolve and precipitate on the surface of the zinc anode[35]. Additionally, these ions can be inserted into or extracted from the manganese dioxide tunnel. Generally, the anode reaction of an aqueous zinc-ion battery in a neutral electrolyte can be summarized as follows:

$$Zn \leftrightarrow Zn^{2+} + 2e^{-} \quad (1\text{-}4)$$

In an alkaline environment (pH > 11), the solubility of zinc increases, promoting the formation of zinc ions and allowing the oxidation-reduction reaction to dominate the corrosion process at the negative electrode. However, in alkaline electrolytes, zinc undergoes a solid–liquid–solid reaction involving Zn, $Zn(OH)_4^{2-}$, and ZnO. The insulating ZnO formed on the surface can easily lead to the passivation of the underlying zinc. Similar to what occurs in mild electrolytes, the non-uniform dissolution and deposition of zinc can take place at various locations on the electrode surface, resulting in significant variations in electrode morphology[36]. The reaction at the anode side of a zinc ion battery in an alkaline electrolyte can be represented by the

following equation:

$$Zn+4OH^{-}\leftrightarrow Zn(OH)_4^{2-}+2e^{-} \quad (1\text{-}5)$$

$$Zn(OH)_4^{2-}\leftrightarrow ZnO+H_2O+2OH^{-} \quad (1\text{-}6)$$

Zinc ion intercalation anode: Zinc-ion deintercalation anodes do not contain metallic zinc; instead, they consist of materials with large tunnel structures that facilitate the insertion and extraction of zinc ions, including $ZnMo_6S_8$[37], Mo_6S_8[38], $Na_{0.14}TiS_2$[39], etc. In this battery system, zinc ions are present in the electrolyte or cathode, and energy storage is facilitated through the insertion and extraction of zinc ions within the TiS_2 negative electrode material, as shown in Figure 1.4b. At the onset of the discharge phase, zinc ions preferentially occupy octahedral sites with lower energy barriers within each crystal unit. By the end of discharge or during the charging process, the anode material undergoes a phase transition, demonstrating good reversibility. For instance, in the case of the Mo_6S_8 negative electrode, the incorporation of zinc ions occurs in a two-step process, with each intercalation step occupying distinct sites within the Mo_6S_8 structure[38]. The corresponding electrochemical reactions can be summarized as follows:

$$Zn^{2+}+Mo_6S_8+2e^{-}\rightarrow ZnMo_6S_8 \quad (1\text{-}7)$$

$$Zn^{2+}+ZnMo_6S_8+2e^{-}\rightarrow Zn_2Mo_6S_8 \quad (1\text{-}8)$$

Research on zinc ion deintercalation in negative electrodes is limited, primarily due to the scarcity of suitable layered negative electrode materials that offer both good ionic and electronic conductivity. For high-performance deintercalation negative electrodes, critical parameters include sufficient capacity, high initial coulombic efficiency, appropriate potential, stable cyclability, and robust rate performance. Additionally, the slow kinetics of zinc ion insertion and extraction in the anode material can directly impair battery performance. Although the ample space within deintercalation anodes provides an ideal host for zinc ions and enhances insertion/extraction kinetics, the mechanical strength of materials with such large

internal structures tends to be low[40]. Repeated battery operation poses a significant risk of structural collapse. Direct contact between the anode material and the electrolyte can lead to material dissolution, severely impacting the battery's performance and lifespan. Furthermore, the high intercalation potential of the anode electrode, along with the inclusion of the current collector, substantially diminishes the overall energy density of the battery. Consequently, our research primarily concentrates on the zinc metal anode.

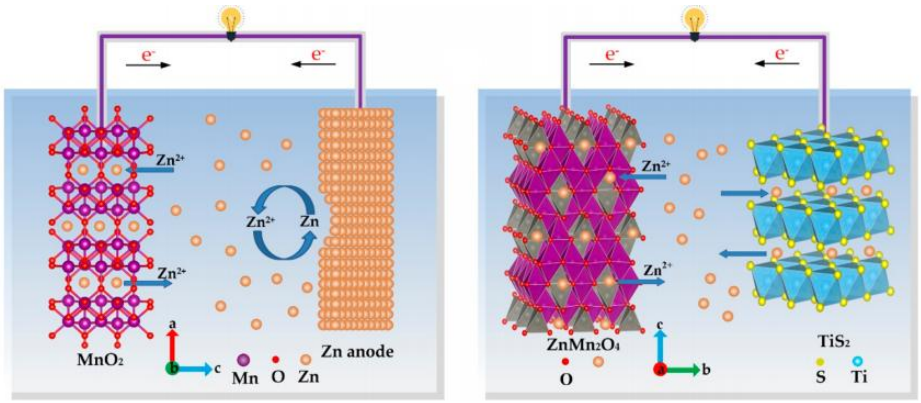

Figure 1.4 Schematic illustrations of the reaction mechanism of the (a) Zn anode and (b) Zn^{2+}-intercalated anode[41].

1.3 Challenges and research progress for zinc metal anodes

1.3.1 Key Challenges for Zinc Metal Anodes

The complex interfacial chemistry is the core challenge limiting the practical application of zinc anodes. During charge/discharge processes, the zinc anode undergoes reversible Zn^{2+} deposition/dissolution reactions, but different electrolyte environments can trigger side reactions: under acidic or neutral conditions, the HER at the interface leads to zinc corrosion and electrolyte decomposition; under alkaline conditions, the formation of a $ZnO/Zn(OH)_2$ passivation layer hinders ion transport and reduces reaction kinetics. Additionally, uneven zinc deposition promotes dendrite growth, which can pierce the separator and cause short circuits, while dynamic changes in the Zn^{2+} solvation structure in the electrolyte further exacerbate interfacial pH fluctuations and the accumulation of byproducts.

Dendrite formation:

Currently, the growth of zinc dendrites poses a significant challenge, directly impacting the cycle performance and Coulombic efficiency of zinc-ion batteries. Achieving uniform zinc deposition is crucial for attaining high Coulombic efficiency and extending the lifespan of the zinc anode[42]. However, uneven zinc deposition is practically unavoidable. This irregular deposition not only increases the volume of the negative electrode due to its loose structure but also creates additional reaction sites, resulting in increased consumption of both the electrolyte and zinc metal. Furthermore, flaky or needle-like zinc dendrites, which are loosely attached to the zinc metal, can easily detach from the surface, forming "dead zinc" that reduces coulombic efficiency and shortens battery life[43]. Additionally, the vertical growth of dendrites increases the thickness of the anode electrode, and large dendrites can penetrate the separator, leading to short-circuiting and potentially severe safety incidents. Zinc dendrites develop through a two-stage process, beginning with nucleation and progressing into subsequent growth phases[44]. While zinc electrodeposition demonstrates distinct electrochemical pathways in alkaline versus neutral media, the fundamental crystallization dynamics governing dendritic growth demonstrate remarkable consistency. For comparative analysis of dendritic formation mechanisms across these electrolytes, all solution-phase ionic species participating in cathodic reduction are formally categorized as zinc species. This systematic approach reveals that during the nucleation regime, zinc species undergo electrophoretically driven migration toward electrode interfaces, preferentially accumulating at lattice defect sites through field-induced interfacial kinetics. This accumulation initiates heterogeneous nucleation, establishing the foundational architecture for subsequent dendritic propagation[45]. Subsequently, these zinc ions receive electrons from the zinc anode and deposit onto the nucleation sites by overcoming the energy barrier of zinc nucleation, provided that the overpotential exceeds this barrier. The initial zinc atoms then diffuse freely across the electrode surface, either accumulating with

other newly formed zinc atoms or relocating to energetically favorable sites to form the initial zinc core[46]. Furthermore, the current density significantly affects the distribution of zinc ion concentration near the zinc anode. At high current densities, a concentration gradient of zinc ions develops between the reaction zone and the bulk solution, promoting uneven zinc nucleation.

Realistic electrode interfaces exhibit inherent morphological heterogeneity, manifesting as stochastic surface asperities that generate charge localization phenomena and nucleation energy barriers. As a result, zinc ions at the interface preferentially deposit at more active sites, forming dispersed zinc crystalline nuclei during the initial nucleation phase. The deposition of these protrusions further exacerbates the uneven distribution of electric fields and ion fluxes at the interface, ultimately leading to dendrite formation. Phase-field modeling quantitatively validates that supra-critical nuclei induce disproportionate field distortion through three mechanisms: (i) geometric screening effects altering equipotential surfaces, (ii) ionic concentration polarization via electroconvective vortices, and (iii) Butler-Volmer kinetics modulation. This finding underscores the importance of preventing the heterogeneous formation of large zinc cores (Figure 1.5a-f)[47]. Furthermore, dendrite growth becomes more pronounced at high current densities due to the limited diffusion process and the influence of critical current density (Figure 1.5g-l)[47].

In the diffusion model, Sand's time (τ) is related to the nature of the transfer of Zn^{2+} ions and electrons[48], as demonstrated in Eq.:

$$\tau = \pi D \frac{eC_0(\mu_a + \mu_{Zn^{2+}})^2}{2 J \mu_a} \tag{1-9}$$

where τ represents the time at which zinc dendrite growth begins, D denotes the diffusion coefficient, C_0 is the initial concentration of the zinc salt, μ_a and μZn^{2+} represent the transference numbers of the anion and Zn^{2+}, respectively, and J is the effective electrode current

density. According to the equation, a smaller effective electrode current density (J) and a larger zinc ion transference number (μZn^{2+}) result in a larger τ, indicating that the zinc anode has a longer cycle life before the onset of zinc dendrite growth[49]. A higher concentration of zinc ions and an increased ion diffusion rate help mitigate concentration polarization. Consequently, relying solely on the concentration polarization and ion diffusion model is inadequate for accurately describing the actual zinc deposition behavior in zinc-ion cells[48]. The rate of zinc ion deposition and electrochemical polarization must also be considered. In practice, zinc ion deposition during charging is governed by mixed polarization, consistent with experimental observations. Therefore, from a kinetic perspective, enhancing the Zn^{2+} diffusion rate while reducing voltage and concentration polarization facilitates uniform zinc deposition.

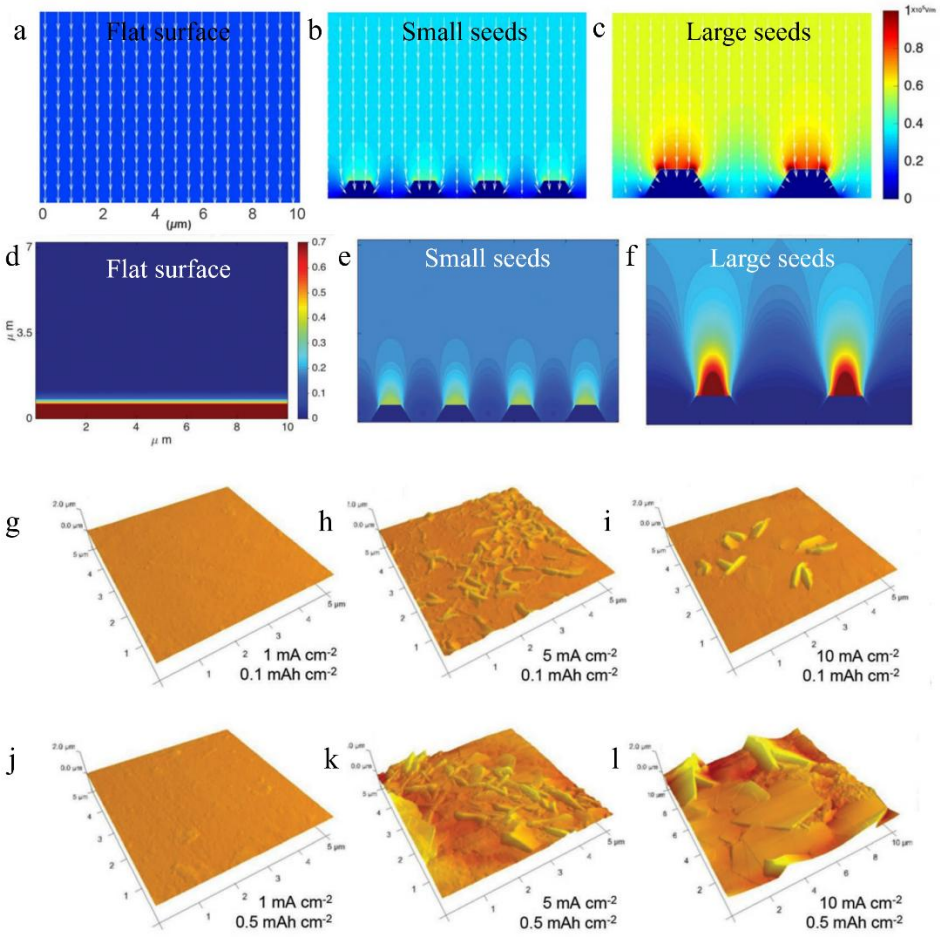

Figure 1.5 Simulation of Zn-ion diffusion and distribution along the 2D surface of electrodes

with different conditions of dendrite formation[50]: (a) flat surface, (b) small dendritic seeds, (c) large dendritic seeds. Simulation of electric field on the surface of Zn electrodes after the first charging process with 0.1 mAh cm^{-2} at different current densities of (d) 1 mA cm^{-2}, (e)5 mA cm^{-2}, (f)10 mA cm^{-2}. (g–i) AFM images of Zn electrodes cycled at 1, 5, 10 mA cm^{-2} with a constant capacity of 0.1 mAh cm^{-2} to observe the nucleation behavior at the initial stage. (j–l) AFM images of Zn electrodes cycled with an increased capacity of 0.5 mAh cm^{-2} to investigate the growth behavior of Zn dendrites at various current densities.

Electrode corrosion:

In mildly acidic electrolytes (pH 4-6), the zinc anode undergoes competing electrochemical processes: the hydrogen evolution reaction (HER) occurs concomitantly with anodic dissolution. This corrosion persistently degrades the electrode surface, thereby increasing resistance and consequently limiting the cycle life of the zinc anode. Thus, the electrochemical corrosion of the zinc anode presents a significant challenge. At the sites of corrosion, zinc metal undergoes dissolution due to electron loss, while the H_2O in the electrolyte accepts electrons, resulting in the production of hydrogen gas and hydroxide ions (OH^-) [51]. When zinc metal contains impurities and zinc electrodes are in contact with the electrolyte, numerous microscopic galvanic cells are established at the zinc metal/electrolyte interface. In these cells, the zinc metal acts as the anode, while the impurities serve as the cathode. Hydroxide ions (OH^-) accumulate progressively and react further with the electrolyte, leading to the formation of by-products on the surface of the zinc cathode. For instance, in a zinc sulfate electrolyte, the electrochemical corrosion reaction can be represented as follows[52]:

$$4Zn^{2+} + 6OH^- + SO_4^{2-} + xH_2O \leftrightarrow Zn_4SO_4(OH)_6 \cdot xH_2O \qquad (1\text{-}10)$$

In contrast to the dense solid electrolyte interphase (SEI) layer observed on other metals, the surface byproduct interface layer on zinc metal is porous and fails to function as an effective SEI, thereby allowing the electrolyte to continue corroding the zinc anode surface. This corrosion reaction between the electrolyte and zinc metal significantly impairs the

electrochemical performance of zinc-ion batteries. Similarly, in other zinc salt electrolytes, a loose byproduct layer forms on the zinc anode surface due to zinc corrosion. For example, in zinc trifluoromethanesulfonimide ($Zn(TFSI)_2$) electrolyte, $TFSI^-$-based complexes can form, akin to the $Zn_4SO_4(OH)_6 \cdot xH_2O$ byproduct layer, which also fails to prevent the electrolyte from corroding the zinc surface. Furthermore, the interfacial impedance induced by this byproduct layer hinders electron and ion diffusion, creating a substantial energy barrier for zinc deposition and severely degrading the battery's electrochemical performance[53]. A critical understanding emerges that zinc dendrite proliferation, hydrogen evolution reaction (HER), and anodic corrosion constitute an interdependent degradation triad, wherein each phenomenon exhibits positive feedback effects on the others. Accelerated hydrogen evolution and electrode corrosion originate from the loose, porous architecture of zinc dendrites. This structure expands the electrode-electrolyte interface, supplying more reaction sites while concurrently reducing local current density and overpotential. Uneven zinc deposition and an elevated overpotential can stem from hydrogen bubbles that cling to the anode, subsequently inhibiting the nucleation of zinc ions. Concurrently, the hydrogen evolution reaction leads to the accumulation of hydroxide ions (OH^-), which can expedite the corrosion process. Corrosion increases the surface roughness of the zinc anode, further exacerbating dendrite formation. Additionally, the large curvature and irregularity of byproduct layers increase the contact area, thereby accelerating the occurrence of hydrogen evolution side reactions.

Hydrogen Evolution Reaction:

Theoretically, the equilibrium potential of Zn^{2+}/Zn (-0.76 V) is consistently lower than that of H_2O/H_2 (0 V) across the entire pH range, indicating the inevitable occurrence of spontaneous hydrogen evolution reactions and corrosion on the zinc surface. Furthermore, the hydroxyl radicals generated due to local pH fluctuations, resulting from increased OH^- concentration, are a significant source of byproduct formation on the Zn anode surface, such as $Zn_4SO_4 \cdot xH_2O$

and $Zn(OH)_2$, as illustrated in Figure 1.6a. As the pH increases, the coexistence of Zn and H_2O becomes thermodynamically unstable, leading to the automatic reduction of water and the production of hydrogen gas[54]. It is crucial to recognize that this reaction represents a significant competitive process occurring on the surface of the zinc metal anode during galvanization. The resultant hydrogen evolution leads to battery swelling and expansion, as depicted in Figure 1.6b[55]. The presence of adhered hydrogen bubbles exacerbates the irregularity of the zinc metal anode's surface, thereby diminishing battery performance. Furthermore, the hydrogen evolution reaction (HER) contributes to the limited electrochemical window of zinc-ion batteries (ZIBs), inherently constraining their practical voltage and energy outputs. Typically, the mechanism of HER at a metal electrode in an acidic medium involves the following three steps:

$$H^+_{(aq)} + e^- \rightarrow H_{ads} \quad (1\text{-}11)$$

$$H_{ads} + H^+_{(aq)} + e^- \rightarrow H_2 \uparrow \quad (1\text{-}12)$$

$$2H_{ads} \rightarrow H_2 \uparrow \quad (1\text{-}13)$$

As illustrated in Figure 1.6c[56], the initial step is the Volmer or discharge stage, where a surface-adsorbed hydrogen atom (H_{ads}) forms when a proton receives a single electron at the interface. Following the formation of H_{ads}, the reaction can proceed via the protonation of H_{ads} coupled with a single electron transfer (Heyrovsky step) and/or through the recombination of two H_{ads} to produce H_2 during desorption (Tafel step)[57, 58]. Consequently, this process not only diminishes the battery's performance but also undermines the inherent safety features of zinc-ion batteries, transforming otherwise safe aqueous cells into potentially hazardous ones. These byproducts, characterized by low ionic conductivity and a loose structure, not only impede zinc plating and stripping but also facilitate contact between the zinc anode and the electrolyte. Therefore, the occurrence of HER continuously consumes active zinc species and electrolytes, resulting in reduced coulombic efficiency[56]. Moreover, HER exacerbates the inhomogeneity

of the zinc anode surface and increases electrode polarization, thereby promoting the formation of dendrites with a loose, porous zinc structure, ultimately leading to the failure of zinc-ion cells.

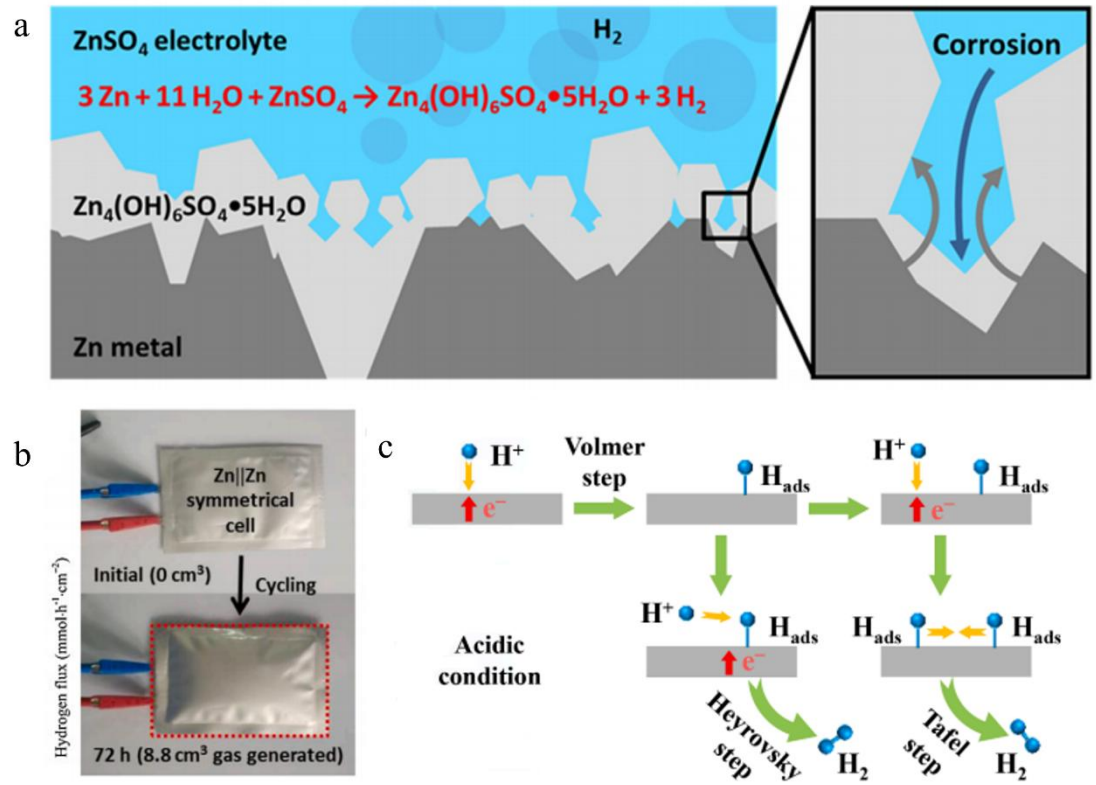

Figure 1.6 (a) A schematic showing the chemical oxidation of Zn metal anodes in batteries employing neutral electrolytes (e.g., $ZnSO_4$). (b) Digital images of the symmetric pouch cell before and after cycling[55]. (c) Schematic pathways for HER under acidic conditions[56].

1.3.2 Current optimization strategies

Electrolyte regulation of zinc coordination environment:

The coordination environment of zinc ions usually depends on the composition of the electrolyte (different salts or solvents)[59]. On this basis, concentrated electrolytes emerge as the most effective approach for modulating the Zn^{2+} solvation structure at molecular scale. In such systems, metal cations preferentially form anion-coordinated complexes instead of aqueous solvation shells, effectively eliminating direct water-anode contact and consequently inhibiting HER originating from water reduction[60]. Meanwhile, the absence of generated OH^-

can effectively inhibit the generation of inactive $Zn(OH)_2$ and ZnO, enhance CE and reduce interfacial resistance.

Firstly, high concentration electrolytes can effectively reduce the number of water molecules ligated around Zn^{2+}, but the development of high concentration electrolyte depends heavily on the salt solubility[61, 62]. LiTFSI (TFSI, bis(trifluoromethanesulfonyl) imide) is an ideal candidate salt because of its high solubility in water (solubility >20 mol kg^{-1} at 25 °C) and excellent hydrolytic stability. Moreover, the high concentration of LiTFSI largely weakened the reactivity of water and regulated its redox potential in water, which inhibited the occurrence of HER[63]. The highly reversible zinc negative electrode originates from the special solvated sheath structure of Zn^{2+}, where Zn^{2+} is surrounded by a large number of bulky anions, causing the coordination form of $[Zn(H_2O)_6]^{2+}$ to be suppressed, forcing TFSI to enter the surroundings of Zn^{2+}, presenting more favorable ions (Zn-TFSI). These advantages bring an unprecedented high reversibility (>4000 cyclys) with $LiMn_2O_4$ as the cathode electrode for full zinc batteries[64]. However, expensive fluorine-based salt electrolytes are very unsuitable for practical mass production. Subsequently, Ji et al.[65] proposed a low-cost aqueous salt electrolyte (30M $ZnCl_2$) in which zinc ions are mainly present in the form of $[ZnCl_4]^{2-}$ to achieve a dendrite free and high CE zinc metal anode. And the incomplete hydration layer of Zn^{2+} inhibits the formation of electrochemical by-products of $Zn(OH)_2$ and ZnO. The significant increase in viscosity of the high-concentration electrolyte leads to reduced ion migration rates, thereby impairing the battery's rate capability and fast charge/discharge performance.

Uniform interface electric field:

It has been shown that the charge transfer resistance in Li-ion batteries is highly dependent on the energy barrier of Li-ion dissolution. Lowering the desolvation energy barrier of Zn^{2+} has also been shown to be beneficial in enhancing the kinetic and electrochemical capacity of the

cell by Linda F. Nazar et al[66]. Zhou et al.[67] prepared zinc negative electrodes by constructing three-dimensional nanoporous ZnO structures in situ on zinc plates, and this porous layer could modulate the structure of the solventized sheath layer of Zn in the bilayer. First principles calculations show that the additional surface charge concentration reduces the desolvation energy barrier of Zn^{2+} and accelerates the Zn^{2+} deposition on the Zn@ZnO 3D Zn anode. The results show that the electrostatic attraction of Zn^{2+} on the anode surface of zinc is greater than that of solventized or hydrated Zn^{2+}, which can effectively suppress the side reactions and enhance the CE of the cell. Notably, artificial organic polyamide (PA) coatings containing abundant polar groups can effectively destabilize the solvation sheath structure of Zn^{2+}. Owing to the robust hydrogen-bonding network within PA, hydrated Zn^{2+} ions preferentially bind to ligand water molecules (prone to triggering parasitic reactions) as they traverse the interfacial layer[68]. The regulation of the anode surface charge is more conducive to lowering the dissolution barrier and further enhance the electrochemical performance of the battery.

Electrochemical reactions at the zinc anode interface are well-established to depend on Zn^{2+} deposition/dissolution dynamics. Specifically, zinc deposition follows an electrochemically driven nucleation and growth mechanism. To achieve uniform Zn^{2+} nucleation and spatially balanced deposition, rapid homogenization of the interfacial electric field is critical for enhancing cycling stability. Crucially, the non-uniform nucleation pattern on the zinc anode directly disrupts the equilibrium of surface electric field distribution during the initial growth stage[69]. The results of finite difference simulations show that the concentration of zinc ions is low at locations with small electric field strength and high at locations with high electric field strength, and the effect of electric field strength becomes more and more significant as the size of zinc nuclei increases. Therefore, a uniform electric field at the electrolyte-anode interface provides a strategic approach for suppressing zinc dendrite growth. Specific strategies include the construction of highly conductive layers (e.g. rGO[70], MXene[71]) on the surface of zinc

negative electrodes and the preparation of three-dimensional structures of zinc negative electrodes. Building a highly conductive layer on the surface of zinc metal electrode can accelerate the charge transfer on the surface of zinc anode, avoiding charge buildup and providing a uniform surface electric field. Wang[72] and Liu[73] proposed a strategy to coat the zinc surface with layered reduced graphene oxide, which can significantly reduce the local current density and achieve a uniform and dendrite free galvanization process. In addition, Wang et al.[74] reported a self-supporting carbon nanotube (CNT) paper material with high flexibility and conductive properties for use between the zinc cathode and the diaphragm prior to battery assembly. During zinc stripping/plating, the deposition sites of Zn^{2+} are mechanically regulated by the porous backbone of the scaffold and the conducting carbon nanotube network maintains a particularly stable electric field, thus mitigating the formation of protrusions/dendrites and the occurrence of some side reactions. In addition, the construction of a three-dimensional structure of the zinc anode is another effective measure for uniform interfacial electric field distribution. The construction of a three-dimensional structure can effectively increase the specific surface area of the zinc anode and significantly reduce the local electric field even at very high current densities[75]. The results show that replacing the planar Zn anode with a porous electrode can lead to a more uniform charge distribution and interfacial electric field distribution at the electrode, and the large contact area between the electrolyte and the electrode can balance the Zn ion flux. Therefore, the construction of three-dimensional zinc metal anode can achieve high performance dendrite free AZIBs. Lu et al.[76] showed that 3D carbon nanotubes act as a Zn support framework to achieve a highly reversible Zn anode. In addition to the three-dimensional carbon-based zinc anode, Xu[77] and Zhou[78] reported the use of a three-dimensional porous copper skeleton as a support material for the zinc anode. Due to the good conductivity and large specific surface area, the anode surface current distribution is uniform and shows reduced polarization and stable Zn plating/stripping performance even at

high current densities and abundant electroactive sites, which can prevent the growth of dendrites.

Induced homogeneous Zinc deposition/plating:

During Zn plating/stripping cycles, modulating the electrochemical supersaturation at the working electrode enables precise control of nucleation overpotential, thereby inducing dendrite-free Zn deposition[79]. Zinc deposition typically requires overcoming nucleation barriers. The initial deposition occurs at a minimal nucleation overpotential (Δη), defined as the potential difference between the stabilization potential and the tip potential[80]. Subsequently, the uneven growth of zinc can lead to the growth of zinc branch products, which can even puncture the diaphragm and lead to a short circuit in the battery[81]. Therefore, the uniform deposition of zinc ions on the zinc anode surface is guided by providing abundant and uniform nucleation sites to achieve the growth of zinc dendrites and obtain a flat zinc deposition surface. The specific methods include (1) modulation of surface polar groups; (2) construction of zinc-friendly surfaces; (3) construction of self-healing electrostatic shields; (4) epitaxial electrodeposition; and (5) optimization of ion flux.

The introduction of abundant polar functional groups (via coating processes) on zinc anode surfaces can accelerate Zn^{2+} diffusion and regulate zinc ion deposition sites. Polishing agents typically exhibit strong synergistic effects with Zn^{2+}, forming a diffusion layer on the electroplating substrate during deposition. This layer provides abundant active sites for nucleation, ultimately leading to the formation of flat zinc deposits. Cui et al.[82] reported that a large number of adsorption sites were obtained in the Zn anode clad PA layer, and a close bond between the PA layer and the Zn metal anode could be achieved due to the ability of coordination between Zn^{2+} and the carbonyl group (C=O) in PA. Furthermore, surface-adsorbed Zn^{2+} (generated via localized electrochemical reduction) displayed confined 2D surface diffusion, analogous to the PEG-mediated mechanism reported in prior studies[83].

Ultimately, based on the high density and suitable size of the nucleated particles, a uniform and dense zinc layer can be formed, matching with the MnO_2 cathode to provide excellent battery performance. Similar to organic polar groups, inorganic polar groups can also be used as effective adsorption sites for Zn^{2+}.

It has been shown that the substrate has a strong influence on the electrodeposition of zinc[84]. It is well-established that Zn nucleation and ordered growth are governed by interfacial binding energy, with enhanced binding energies promoting preferential nucleation. However, interfaces exhibiting higher Zn-binding energies necessitate elevated hydrogen evolution overpotentials (HER), which are characteristic of Znophilic interfaces optimized for stable cycling[85]. Therefore, the construction of pro-Zn hosts is also an important strategy to induce Zn stripping/plating. Recent advances demonstrate that Sn-modified multifunctional 3D carbon substrates exhibit superior Znophilicity compared to conventional metallic substrates (e.g., Ti, Ag), enabling uniform Zn deposition with high Coulombic efficiency (CE). The strong Zn adsorption energy of Sn atoms, combined with their robust electronic coupling effects, synergistically suppresses parasitic reactions (e.g., HER) while enhancing Zn^{2+} migration kinetics and dendrite-free Zn plating, thereby significantly improving the cycling stability and energy efficiency of aqueous zinc-ion batteries (AZIBs)[86]. In addition, it has been shown that the zinc-friendly monolayer graphene layer substrate has a strong affinity for zinc, allowing for a dendrite free zinc deposition process. Moreover, due to the good lattice compatibility of graphene and Zn, the single graphene layer provides a lower nucleation overpotential site for Zn electrodeposition and finally achieves uniform planar Zn deposition[87]. The self-healing electrostatic shielding effect on the zinc anode surface can also induce dendrite free growth of zinc. For example[88], when sodium citrate (Na_3CA) is introduced as an electrolyte additive, sodium ions (Na^+) form an electrostatic shielding layer on the zinc surface, suppressing the growth of zinc dendrites. Meanwhile, the zincophilic citrate anions (CA^{3-}) displace water

molecules in the solvation shell via a leveling effect, thereby reducing side reactions. Additionally, these anions adsorb onto the electrode surface, promoting uniform zinc deposition.

In recent years, a small amount of work on zinc epitaxial growth has been reported. Most of the zinc anodes for AZIBs currently use commercially produced zinc foils with exposed crystal faces dominated by (101) weave[89] and no fixed crystal face orientation[90]. The textured zinc anode exhibits heightened susceptibility to dendrite propagation during cycling, ultimately inducing cell failure via internal short circuits. Furthermore, Zn(002) crystal planes demonstrate superior corrosion resistance compared to (101) and (100) orientations, attributed to their higher planar atomic stacking density that effectively impedes electrolyte penetration[91, 92]. During epitaxial electrodeposition, the strongest orientation dependence is achieved by direct nucleation and growth of epitaxial layers on substrates with minimal lattice strain over-applied. Archer et al.[93] developed a novel strategy for achieving Zn epitaxial electrodeposition on horizontally oriented graphene substrates. By leveraging the minimal lattice mismatch between graphene and the underlying metallic substrate, they engineered macroscopic alignment of the graphene basal plane with the substrate surface. This crystallographic coherence drives epitaxial Zn deposition, preferentially orienting Zn (002) crystal planes through lattice-guided growth. On the graphene sheet layer, the zinc deposition process proceeds sequentially with heterogeneous epitaxial growth and homogeneous epitaxial growth, and it is clear that these results indicate that the epitaxial growth strategy is highly reversible for zinc negative electrodes at moderate or even high current densities.

1.4 Remaining challenges and research objectives

Based on the discussion and summary of previous reports, the stability of zinc anodes is closely correlated with side reactions, electric field distribution uniformity, and electrode interface morphology. However, significant research gaps remain in several critical aspects. For instance,

the use of high-concentration electrolytes inevitably increases costs, while long-term cycling may lead to the depletion of additives through deposition, thereby losing their regulatory function. Constructing artificial interphase layers on zinc anodes is a common approach to enhance stability. However, the diversity of materials significantly complicates the screening process. Most artificial SEI layers (e.g., ZnF_2[94], ZnO[95]) exhibit insufficient ionic conductivity ($<10^{-3}$ S/cm), while highly conductive materials (e.g., rGO[70], CNT[74]) may exacerbate side reactions. Poor mechanical stability is another critical challenge—rigid coatings (e.g., Al_2O_3[96]) are prone to cracking during Zn deposition/dissolution, leading to localized current concentration. Thus, there is an urgent need to develop a rational screening mechanism to guide interphase material selection.

Additionally, most current research focuses primarily on the deposition process, often neglecting the stripping process. In reality, an asymmetry exists between deposition and stripping—non-uniform dissolution during stripping can directly induce electrode volume changes or even structural collapse, triggering localized current concentration and dendrite growth. In practical applications, since most cathode materials are zinc-free, the zinc anode must first undergo stripping. Therefore, optimizing this process is crucial, particularly under high zinc anode utilization, which accelerates failure. Therefore, we aim to design well-controlled experiments to uncover the underlying mechanisms of these unresolved issues and leverage these findings to improve zinc metal anodes. The primary objectives of this thesis are as follows:

(i) To create a series of high-quality anode surfaces through building an interfacial layer which is needed to exhibit good homogeneity. We introduces a multifunctional integrated MXene-porous polydopamine membrane that not only homogenizes the electric field distribution and zinc ion flux for dendrite-free zinc plating/stripping, but also effectively captures water molecules to suppress corrosion reactions. This synergistic effect leads to significantly

enhanced stability of aqueous zinc anodes.

(ii) Through a systematic series of experiments, we investigate the mechanistic principles governing interface material selection. This study delves into the interfacial evolution of zinc anodes during electrochemical processes, employing micro-scale visualization of deposition/stripping dynamics to establish a robust screening framework. We established a like Sabatier principle for screening optimal TM interface for high DOD cycling Zn anodes. It is proved that a moderate TM-Zn interaction strength can favor the uniform stripping of Zn anodes. The flat and zincophilic interphase further regulates a dendrite-free and uniform Zn metal plating process.

(iii) To achieve long-term cycling and high utilization rate battery, the mechanism of the action of the interfacial layer will be explored by characterization, electrochemical tests and theoretical calculations. We propose an innovative bilayer metallic interface architecture that leverages in situ alloying reactions between metal layers to synergistically combine stress buffering capability with dual advantages in regulating uniform Zn^{2+} deposition, thereby providing new insights for achieving stable zinc anodes with high utilization efficiency.

Chapter 2 Experimental Methods

The main chemicals and reagents for the series work are listed in this chapter. This chapter also describes the material preparation, structure, composition, and main experimental measurements. The specific method for each work was listed.

2.1 Chemicals and reagents

Table 2.1 Chemistry and reagents required for the experiment

Chemical	Molecular formula	Specifications	Manufacturer
Zinc sulfate monohydrate	$ZnSO_4 \cdot H_2O$	AR	Aladdin
Absolute ethyl alcohol	CH_3CH_2OH	AR	Aladdin
Acetone	CH3COCH3	AR	Guoyao
MXene	$Ti_3C_2T_x$	/	11 Technology Co., Ltd
Dopamine hydrochloride	$C_8H_{11}NO_2 \cdot HCl$	AR	Aladdin
1,3,5-Trimethylbenzene	C_9H_{12}	AR	Aladdin
Pluronic® F-127	$(C_3H_6O \cdot C_2H_4O)_x$	AR	Sigma
Ammonia solution	$NH_3 \cdot H_2O$	AR	Aladdin
Polyvinylidene fluoride	$(C_2H_2F_2)_n$	AR	Aladdin
1-Methyl-2-pyrrolidinone	C_5H_9NO	AR	Aladdin
Conductive carbon	C	AR	Aladdin
PEG4000	$(C_2H_4O)nH_2O$	AR	Aladdin
Vanadium (V) oxide	V_2O_5	AR	Aladdin
Oxalic acid dihydrate	$C_2H_2O_4 \cdot 2H_2O$	AR	Aladdin
Carbon nanofiber	CNF	/	Taobao
N-methyl-2-pyrrolidones	NMP	99.9%	Aladdin
Zinc foil	Zn	99.99%	Taobao

Copper foil	Cu	99.99%	Taobao
Titanium	Ti	99.99%	Taobao

2.2 Material synthesis

Preparation of cathode material $NH_4V_4O_{10}$: In a typical experimental procedure, $NH_4V_4O_{10}$ was synthesized by a simple hydrothermal reaction[97]. First, ammonium metavanadate (10 mmol, NH_4VO_3, Aladdin) was dissolved into deionized water (60 mL) and stirred for 20 min under room temperature. Then added the oxalic acid (4 mmol, $H_2C_2O_4 \cdot 2H_2O$, Aladdin) to the above solution with magnetic stirring for 40 min. The above solution was then transferred into a Teflon-lined container (100 mL) and heated at 180 ºC for 6 h. At the end of the reaction, the precipitate was collected and washed 5 times using deionized water with the help of a centrifuge and placed in a vacuum-drying oven at 60°C for 24 hours. The powder obtained was then fixed with conductive carbon (Super P) and binder (PVDF) at the weight ratio of 7:2:1, in which N-methyl-2-pyrrolidones as the dispersants. The slurry was cast onto carbon paper (HCP030N, Shanghai Hesen Electric Co., Ltd) and subsequently dried in a vacuum oven at 60 °C for 24 hours. The mass loading is about 2.5-3.0 mg cm^{-2}.

Synthesis of MXene-porous polydopamine: In a typical progress, 1 mL MXene (Ti_3C2T_x) aqueous solution (6 mg mL^{-1}) was diluted in deionized water (5 mL) by sonicating in an ultrasound machine for 30 minutes to ensure a homogeneous dispersion of MXene. 0.1 g of F127 (supplied by Sigma) was added to the above solution with magnetic stirring for 1 h. Thereafter, 0.15 g dopamine hydrochloride ($C_8H_{11}NO_2 \cdot HCl$, supplied by Aladdin) and 3 mL ethanol were added and stirred for 30 min. 400 μL tetramethylbenzidine (TMB, supplied by Aladdin) and 0.375 mL ammonia solution ($NH_3 \cdot H_2O$, supplied by Aladdin) were added in the mixture under constant stirring. After 2 h of full reaction, the MPP hybrids were collected by centrifugation and rinsed with deionized water and ethanol. MPP-Zn electrodes were prepared by a spray coating method. Typically, the MPP ethanol dispersion with a certain concentration

of 1 mg mL-1 was sprayed on a Zn foil and dried at 50 ℃. In order to verify the role of mesopores on MPP layer, PDA without pores was also coated on MXene flakes. The pore formation precursors including F127 and TMB were not added for the synthesis procedure.

Fabrication of TM@Zn anode : Cu@Zn electrodes were prepared by the magnetron sputtering method. Firstly, 100 and 10 μm zinc foils were sonicated in alcohol for 20 min and then dried. Subsequently, a DC target mode with a power of 60 W was selected, Ar gas with a flow rate of 30 sccm, and held for 515 seconds. For zinc foils used to DOD testing, the same sputtering operation was performed on both sides of the zinc foil. Ag (50 W, 343s), Au (80 W, 277s), Ti (150 W, 800s) and Al (70 W, 900 s) are modified to zinc foil using the same method.

Synthesis of vanadium dioxide (VO_2) cathode material : In this study, uniform VO_2 nanorods were synthesized by a simple hydrothermal method[98]. The specific experimental procedure is as follows: 9.6 mmol of oxalic acid ($H_2C_2O_4 \cdot 2H_2O$, Aladdin), 4 mmol of Vanadium (V) oxide (V_2O_5, Aladdin) and 3.4 mmol of PEG-4000 (M_n3500-4500, average M_n4000, Aladdin) were added into 66 mL deionized water. This was followed by continuous magnetic stirring in a water bath at 40 ºC for 24 h to obtain a homogeneous solution. Subsequently, the above samples were transferred to a 100 mL Teflon-lined container and held at 180 ºC for 24 h. Afterward, when the samples were naturally cooled to room temperature, they were washed several times with deionized water and ethanol. Finally, the final product was collected after drying at 70 ºC for 24 h. The powder was mixed with carbon nanofiber (CNF) and binder (PVDF) at the weight ratio of 7:2:1, in which N-methyl-2-pyrrolidones (NMP) as dispersants. The slurry was cast onto carbon paper (TORAY, TGP-H-060) and dried in a vacuum oven at 60 ºC. The mass loadings of cathode materials are about 1.2~2.0 mg cm^{-2}.

Fabrication of Cu/Ag@Zn anode : Cu/Ag@Zn electrodes were prepared by the magnetron sputtering method. Firstly, 100 and 10 μm zinc foils were sonicated in alcohol for 20 min and

then dried. Subsequently, Cu target at a DC target mode with a power of 60 W was selected, Ar gas with a flow rate of 50 sccm, and held for 1028 seconds. Then, Ag target at a DC mode with a power of 50 W. Ar gas with a flow rate 50 sccm, and held for 686 s.

2.3 Material Characterization Methods

X-ray diffraction analysis (XRD): X-ray diffraction analysis (XRD) is a technique used in materials science to determine the crystallographic structure of a material. XRD works by irradiating a material with incident X-rays and then measuring the intensities and scattering angles of the X-rays that leave the material. Crystallographic information for all samples presented in this paper was obtained by x-ray diffraction (xrd) using Cu-ka radiation on a Rigaku Ultima IV diffractometer. The measured XRD data obtains the corresponding crystal structure information.

Scanning Electron Microscope (SEM): Operating through the process of scanning a focused electron beam over the surface, the scanning electron microscope (SEM) is an analytical tool used for obtaining detailed images of samples. In this paper, the Tescan VEGA3 and Tescan MIRA electron Microscope are used to observe the microscopic morphology of the material.

Transmission Electron Microscope (TEM) and scanning transmission electron microscope (STEM) : Transmission electron microscope (TEM) is mainly used to observe the internal structure of the crystal material, and its working principle is mainly for the electron beam penetrating through the crystal material to produce secondary imaging. In order to achieve a good test effect, the test samples should not be scattered as far as possible to reduce the scattering of the electron beam. In this paper, JEM-2100f model transmission electron microscope and spectra 300 STEM were used. In work 1, before testing, sonicate the sample in absolute ethanol, and then dry the sample in a copper mesh with a pipete gun. In work 2 and 3, Helios 5 CX DualBeam FIB system was used to prepare the cross-sectional STEM samples.

X-ray Photoelectron Spectroscopy (XPS) : Employing the photoelectric effect, X-ray

Photoelectron Spectroscopy (XPS) is a surface-sensitive quantitative spectroscopic technique designed to elucidate the elemental composition, chemical states, and overall electronic structure of a material's surface. In this paper, Thermo Fischer, ESCALLAB Xi^+ model optoelectronics, spectrometer for XPS test and Al kα as x light source.

Atomic force microscopy (AFM) : Atomic force microscopy (AFM) is a powerful technique that enables the imaging of almost any type of surface, including polymers, ceramics, composites, glass and biological samples. In this paper, AFM will be used to measure the thickness of the material and the surface roughness of the electrode.

Contact angle (CA): Conventionally measured through the liquid, the contact angle quantifies the angle between the tangent to the liquid-vapor interface and the solid surface at their point of contact. It quantifies the wettability of a solid surface by a liquid via the Young equation. In this paper, Kruss DSA100 was used to test the change of the wettability of the material.

2.4 Cell assembly and electrochemical measurement

Battery Assembly: Type CR2032 battery can be assembled in air at room temperature. Put the anode and cathode electrode battery shell and stainless steel gasket into the beaker, add excessive absolute ethanol to the material, ultrasonic cleaning twice, and then put it in the oven 80 ^oC dry, dry for backup. The full cells are assembled in the order of positive shell, $NH_4V_4O_{10}$ cathode electrode (work 1), VO_2 cathode electrode (work 2 and 3), glass fiber (thickness of 1 mm and diameter of 19 mm) as the separator, electrolyte, Zn metal (100 um). The symmetrical cells are assembled in the order of positive shell, negative disc, separator, electrolyte, negative disc, stainless steel gasket and negative shell. The half-cells are assembled in the order of positive shell, copper or stainless steel gasket, separator, electrolyte, stainless steel gasket, negative disc and negative shell. Whatman glass microfibre filter paper, 90 mm diameter, was used for all diaphragms. The electrolyte for all types of cells is 2.0 mol-L^{-1} $ZnSO_4$ aqueous solution. Add 6 to 8 drops of electrolyte when assembling symmetrical cells and full cells.

Electrochemical Impedance Spectroscopy (EIS) : Electrochemical Impedance Spectroscopy is one of the most important electrochemical techniques where the impedance in a circuit is measured by ohms (as resistance unit). Over the other electrochemical technique, EIS offers several advantages reliant on the fact that it is a steady-state technique, that it utilizes small signal analysis, and that it is able to probe signal relaxations over a very wide range of applied frequency, from less than 1 mHz to greater than 1 MHz, using commercially available electrochemical working stations. In this work, Electrochemical impedance spectra (EIS) was measured by CHI760E with the frequency range from 100 kHz to 10mHz, and the amplitude was 5 mV.

Tafel testing : To measure the corrosion rate, the liner sweeping curves were tested by a three-electrode configuration in 2 M ZnSO4 aqueous electrolyte, in which bare Zn or modified Zn as the working electrodes, Pt foil as the counter electrode and Ag/AgCl as the reference electrode. The voltage window was set from -1.1 to -0.6 V at a scan rate of 2 mV s^{-1}[99].

Chronoamperometry (CA): An electrochemical technique characterized by monitoring the transient faradaic current, as a function of time, following the application of a potential step to the working electrode. The potentiostatic current-time transient curves were obtained at a fixed overpotential of -150 mV.

Cycling testing: The electrochemical experiments of all type cells were tested using a CR2032 coin cell. Cycling measurements were conducted on Neware CT-3008 battery testers. A repetitive loop of charging and discharging is called a cycle. The constant current charge/discharge test is carried out in a multi-channel battery test system with different current densities and charge/discharge times to test the discharge capacity and cycle life of the battery. The experiment is used to test the long-term cycle life of symmetrical cells, the multiplier performance, the cycling performance and the stability of the full cell. The range of voltages for Zn||$NH_4V_4O_{10}$ full cells is 0.6 to 1.8 V. The range of voltages for Zn||VO_2 full cells is 0.1 to

1.2 V. The CEs values were calculated by dividing the stripped capacity (Q_s) over the plating capacity (Q_p) for each cycling in asymmetric cells at a fixed plating capacity of 1 mAh cm^{-1} and a cutoff voltage of 0.8 V for stripping reaction. Average CEs are calculated using the equation: $CE_{ave} = \frac{1}{n}\sum_1^n \frac{Q_s}{Q_p}$.

2.5 Calculation

The binding energy for water molecules to MXene, MPP, and Zn^{2+}:

Unless otherwise specified, this calculation is carried out by Dmol3 under Materials Studio. Firstly, the structural model of each component was constructed, and the (0 0 2) crystal plane of $Ti_3C_2T_x$ was cut, then the structure was optimized, and the optimized structure was used to expand the cell to a suitable size. Using GGA-PBE method and DN basis set, the binding energy (E) was calculated under the conditions of convergence energy of 1.0×10^{-4} and k-point of 3×3×3.

$$E=E_{ab}-E_a-E_b$$

Where, E_{ab} is that total energy of the combine substance, and E_a and E_b are the respective energies of the first two substances.

Geometrical specifics for modeling the Zn ion concentrations through MXene layer and MPP layer:

During Transport of Diluted Species Interface calculation, the parameters are referring to the geometric factors of MXene and the MPP flakes. The Zn ion migration kinetics follow Fick's law and the Nernst-Einstein relationship. The width boundaries were set to meet periodic conditions, and upper boundary is the bulk electrolyte concentration. The solution procedure is based on the free triangle meshing. The solver converges used PARDISO (parallel sparse direct solver) and the Newton's method. The relative tolerance is set to be 10-6 to ensure accuracy and reliability.

Table 2.2 The parameters for modeling of the Zn ion concentrations

Symbol	Parameter	Model_Exp	Unit
D_{Zn}	Diffusion coefficient	1×10^{-7}	$m^2\ s^{-1}$
Z_{Zn}	Transfer number	1	
F	Faraday constant	96485	mol^{-1}
i_0	Exchange current density	400	$A\ m^{-2}$
α_a	Cathodic charge transfer coefficients	0.5	
α_b	Anodic charge transfer coefficients	0.5	
T	Working temperature	300	K

Electric field distribution and current density distribution on the bare Zn and MPP-Zn : The steady-state electrochemical deposition process on the metal electrode surface was calculated using finite element simulation in a simplified two-dimensional model. The simulation is carried out based on the Tertiary Current Distribution (TCD) module in COMSOL 6.0. Specifically, the electrode surfaces of the test and control samples are set with the same degree of bulging to represent the initial unevenness of the metal electrode, and the test model additionally incorporates an artificial coating on the outer side of the metal electrode. The upper boundary of the simulation area is set as a constant electrolyte potential to refer to the bulk electrolyte, and the lower boundary is set as the reaction electrode, where the electrochemical reduction process occurs on the surface under the overpotential bias. The current characteristics of the electrochemical reduction process follow the Butler-Volmer equation and the Nernst equation, and the ion migration follows the Nernst-Planck equation. The solution process is based on the PARDISO solver, and the relative tolerance and residual factors are set to 10^{-8} and 1.0, respectively. Boundary layer meshes are set on the surface of the simulated electrode, and the rest of the simulated area is meshed based on the free triangle division method to ensure the accuracy of the simulation results.

There are three coupling physical fields for Zn electrodeposition modeling, including: (i) potential and current density distribution in plating layer and electrolyte, (ii) ion transport in electrolyte following concentration diffusion and migration mechanisms under electric field, and (iii) electro-deposition process of Zn ions to form Zn metal phase. The Zn2+ diffusion follow the Fick's law as shown in Equation 2.1 and 2.2:

$$J_i = -D_i \nabla c_i \tag{2.1}$$

$$\frac{\partial c_i}{\partial t} + \nabla \cdot J_i = R_{i,tot} \tag{2.2}$$

Where J_i, D_i , c_i, ∇c_i refers to the ion flux, diffusion coefficient ($D_{Zn} = 1 \times 10^{-7}$ m^2 s^{-1}), ionic concentration and concentration gradient..

The relation between the diffusion coefficient and electric mobility follow the Nernst-Einstein equation:

$$N_i = -D_i \nabla c_i - z_i u_{m,i} F c_i \nabla \phi_l \tag{2.3}$$

Where z_i is the transfer number ($z_{Zn} = 1$), $u_{m,i}$ is the electric mobility coefficient, F is the Faraday constant (96485 C mol^{-1}), ϕ is the electrolyte potential.

The equilibrium potential of the electrode surface follows the Nernst equations:

$$E_{eq} = -\frac{\Delta G}{nF} \tag{2.4}$$

$$E_{eq} = E_{eq,ref} - \frac{RT}{nF} \ln \prod_i \left(\frac{a_i}{a_{i,ref}}\right)^{v_i} \tag{2.5}$$

Where E_{eq}, $E_{eq,ref}$, ΔG, R, T, n, a_i, $a_{i,ref}$, v_i is the electrode potential, the standard electrode potential, the Gibbs free energy change, the ideal gas constant, the temperature (T = 300 K), the electron transfer molar number, the electrode reactive ion concentration, the standard electrode reactive ion concentration, and the reaction stoichiometric number, respectively.

The electrode reaction for the electrode surface follows the Butler-Volmer kinetics expression:

$$i_{loc} = i_0 \left(\exp\left(\frac{\alpha_a F \eta}{RT}\right) - \exp\left(\frac{-\alpha_c F \eta}{RT}\right)\right) \tag{2.6}$$

Where i_{loc} is the local current density at the electrode/electrolyte interface, i_0 is the exchange current density, α_a and α_c is the cathodic and anodic charge transfer coefficients ($\alpha_a = \alpha_c = 0.5$), η is the overpotential.

Table 2.3 The simulation parameters for the Electric field distribution and current density distribution

Symbol	Parameter	Model_Exp.	Unit
D_{Zn}	Diffusion coefficient	1×10^{-7}	$m^2\ s^{-1}$
Z_{Zn}	Transfer number	1	
F	Faraday constant	96485	mol^{-1}
i_0	Exchange current density	400	$A\ m^{-2}$
α_a	Cathodic charge transfer coefficients	0.5	
α_b	Anodic charge transfer coefficients	0.5	
T	Working temperature	300	K

Electric field distribution and current density distribution on the bare Zn and Cu@Zn :
The simulation of Zn electrodeposition dynamics was conducted utilizing the finite element method based on COMSOL Multiphysics 6.1. A two-dimensional electrochemical deposition model was established, incorporating two initial configurations of 1) triangular nuclei and 2) homogenous layer, as depicted in Figure X. To accurately simulate the transient behaviors associated with electrochemical deposition on the electrode surface with two initial configurations, the model employed both the tertiary current distribution and phase field modules[100]. The migration and diffusion of charged species were quantitatively described by the Nernst–Planck transport equation and the electrochemical kinetics at the electrode interface were modeled using the concentration-dependent Butler–Volmer equation. The deposition process was simulated over a duration of 200 seconds, under an exchange current density parameter set at 15 $A\cdot m^{-2}$. The computational domain was discretized using an 'extra fine' mesh of free triangles which meets the requirement of mech convergence.

Chapter 3 A Multifunctional Interface for Dendrite-Free Zinc Metal Anodes

3.1 Introduction

The combustion of fossil fuels accounts for approximately 80% of global energy consumption, which has raised growing concerns about global warming, air pollution, and unsustainable development[101]. To mitigate these challenges, exploring renewable energy sources such as solar and wind power has become mainstream, although they still struggle with intermittent supply[102]. To integrate green energy with established power grids, energy storage systems serve as a critical hub. Lithium-ion batteries, with their balanced electrochemical performance and energy costs, have dominated the rechargeable battery market for decades[103], but the safety concerns of organic electrolyte burning[81] and the scarce abundance of lithium in the Earth's crust [104] stimulated the imperative explorations of Li-free aqueous rechargeable battery technologies. Among the limited options available, aqueous zinc-ion batteries (AZIBs) stand out as a promising solution for large-scale energy storage systems, thanks to their low cost, environmental friendliness, high energy density, and inherent safety advantages[105],[106]. Zinc metal is considered an ideal anode material for AZIBs due to its high theoretical capacity (820 mAh g^{-1}) and low redox potential (-0.76 V vs. standard hydrogen electrode)[107].However, zinc metal faces persistent challenges, including inevitable zinc dendrite formation, corrosion, and hydrogen evolution. These dendrites can penetrate separators, leading to internal short circuits[108].

To mitigate these challenges, relentless efforts over the past decades have significantly enhanced the performance of zinc metal batteries. These strategies can be categorized into three approaches: engineering the structure of zinc metal, designing electrolyte architectures, and manipulating interfacial chemistry[109]. Among these strategies, surface modification of zinc

metal has demonstrated to be both straightforward and effective in mitigating undesirable side reactions at the Zn/electrolyte interface[110]. For instance, surface coatings employing carbonaceous materials, metal compounds, and polymers have been developed to enhance the electrochemical performance of zinc metal anodes. Nevertheless, these conventional coatings often fail to simultaneously fulfill the multifunctional requirements of ideal interlayers. While alloy-based metallic coatings (e.g., Ag, Au) can effectively isolate the electrolyte from direct contact with Zn metal to mitigate corrosion, their practical application is limited by structural degradation caused by repetitive volume expansion/contraction during cycling, ultimately leading to coating disintegration and pulverization[111]. To achieve dendrite-free zinc deposition, highly conductive porous carbon architectures—particularly graphene foams and carbon nanofibers—have been strategically employed as surface coatings on zinc metal anodes. These carbon-based interlayers effectively regulate zinc ion flux distribution and promote homogeneous deposition morphology. However, their inherent porosity simultaneously facilitates undesirable hydrogen evolution reactions by providing diffusion pathways for water molecules through the carbon matrix[112]. Despite their demonstrated efficacy in mitigating both corrosion and dendrite formation, hydrophobic polymer coatings—including polyamides, poly(vinyl butyral), and phytic acid—present significant limitations due to inherently low ionic conductivity and extended Zn^{2+} diffusion pathways[113]. Consequently, the development of multifunctional interfacial layers capable of concurrently enabling dendrite-free zinc deposition and effective corrosion inhibition presents a significant scientific challenge.

MXene, an emerging two-dimensional (2D) transition metal carbide/nitride, has garnered significant research attention owing to its exceptional electronic conductivity and abundant surface functional groups, both of which contribute synergistically to enhanced zinc metal anode protection[114, 115]. However, pristine MXene nanosheets are inherently susceptible to van der Waals-driven restacking phenomena, which inevitably reduces interlayer spacing and

diminishes accessible surface area[116]. This structural degradation consequently restricts the availability of electrochemically active sites and compromises ion transport pathways, ultimately impairing the kinetics of zinc deposition[117, 118], which strategy has yet been reported in AZIBs. In addition, dopamine is a low-cost, green and readily available monomer that can self-polymerize into polydopamine at room temperature[119]. The mesoporous polydopamine (PDA) framework possesses a high density of surface functional groups that serve as effective coordination sites for modulating zinc ion diffusion kinetics through strong chelation interactions.

Herein, we rationally designed a MXene-porous polydopamine (MPP) hybrid interfacial layer on zinc metal substrates via spin-coating deposition. This engineered architecture demonstrates three critical functions: (1) the ordered mesoporous polydopamine matrix functionalizes the surface chemistry through its abundant catechol groups, (2) expands the interlayer spacing to facilitate ion transport, and (3) stabilizes the MXene sheets against restacking through interfacial interactions. With excellent hydrophilicity and zincophilicity, MPP can not only homogenize the electric field distribution and Zn ion flux for dendrite-free Zn metal plating/stripping but also effectively trap water molecules to suppress corrosion reactions. The MPP-Zn composite anodes demonstrate exceptional electrochemical performance, exhibiting: (i) extended cycling stability (>1000 h in symmetric cells and 900 cycles in asymmetric configurations), (ii) outstanding rate capability (up to 8 A cm^{-2}), and (iii) significantly enhanced durability compared to unmodified Zn electrodes. When integrated with $NH_4V_4O_{10}$ cathodes in coin cell assemblies, the MPP-Zn based full cells maintain superior specific capacity retention over 300 cycles, with minimal capacity fade, highlighting their potential for practical energy storage applications. This interface layer, which enables desolvation, uniform electric field and homogeneous zinc ion diffusion, will promote the development of a multifunction-in-one concept in the field of Zn anode surface engineering.

3.2 Results and discussion

3.2.1 MXene-porous polydopamine interfacial layer

Figure 3.1 schematically illustrates the rational design of the MPP interfacial layer for regulating Zn deposition behavior in aqueous electrolytes, in comparison with conventional bare Zn anodes. For bare Zn electrodes, Zn^{2+} ions preferentially nucleate at high-energy charge transfer sites, forming initial protrusions that subsequently grow through autocatalytic deposition to minimize surface energy. This self-amplifying process leads to severe electric field inhomogeneity and uncontrolled dendritic growth.

Furthermore, in neutral or mildly acidic electrolytes (pH 4-7), the combined action of free H_2O molecules and dissolved O_2 induces inevitable corrosion of the Zn metal surface through coupled electrochemical reactions[120]. Consequently, the side reactions altered the local PH values and the surface chemical structures (Figure 3.1a), rendering poorly stable Zn electrodes as demonstrated in the literature[121]. In contrast, the MPP interfacial layer demonstrates multifunctional protection for Zn anodes through three synergistic mechanisms (Figure 3.1b): (i) Structural Regulation:The porous polydopamine-coated MXene framework provides abundant nitrogenous functional groups that significantly enhance surface hydrophilicity, thereby homogenizing Zn^{2+} concentration gradients across the electrode-electrolyte interface. (ii) Electrokinetic Control: The conductive MPP matrix uniformly redistributes the electric field while simultaneously reducing nucleation overpotential through enhanced Zn^{2+} diffusion kinetics, effectively inhibiting dendritic growth morphologies. (iii) Molecular Engineering: Strong chemisorption between MPP's functional groups and H_2O molecules promotes complete desolvation of $[Zn(H_2O)_6]^{2+}$ complexes prior to deposition, achieving dual functionality of corrosion suppression and improved deposition efficiency.

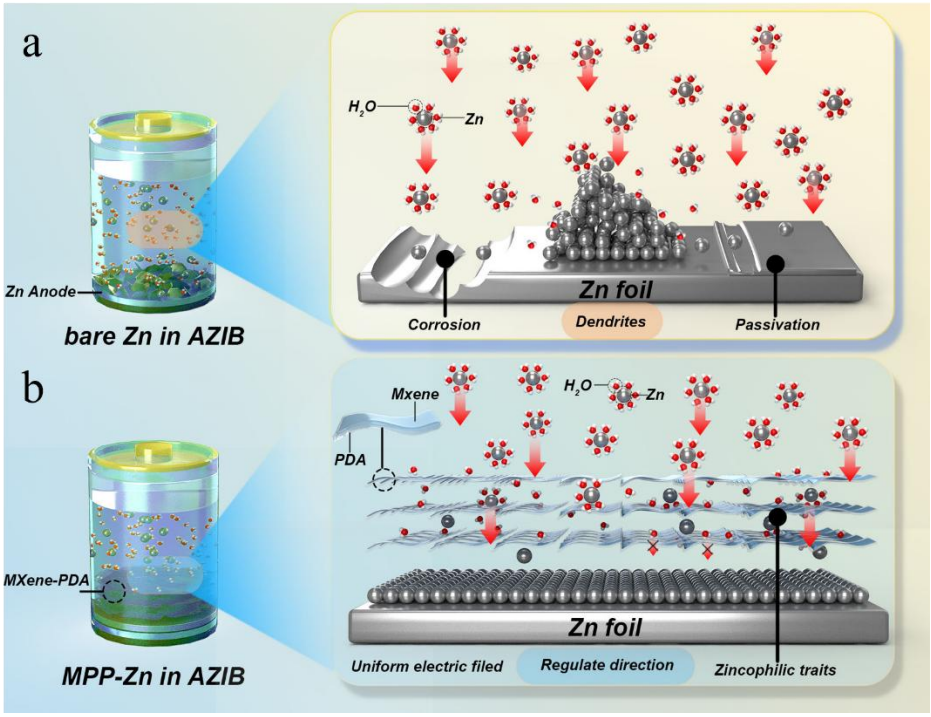

Figure 3.1 Schematic illustrations of Zn metal plating behaviors on (a) bare Zn and (b) MPP-Zn electrodes. The fundamental challenges for bare Zn cycling in aqueous electrolytes and the strategies to overcome them in MPP-Zn are described.

Figure 3.2a-c present comprehensive morphological characterizations of the MXene precursor and resulting MPP composite. The chemically exfoliated MXene displays an atomically thin, defect-free morphology with characteristic smooth surface topography, confirming high phase purity and successful delamination. Subsequent polydopamine functionalization yields a conformal, nanoporous coating that uniformly encapsulates individual MXene sheets while perfectly preserving their two-dimensional architecture, as evidenced by the maintained lamellar spacing and edge sharpness in high-resolution images (Figure 3.2b and 3.2c). Figure 3.2c reveals a highly ordered mesoporous architecture in the MPP layer through high-resolution HRTEM imaging, exhibiting uniform pore diameters of 12 nm. From a rational interphase engineering standpoint, the precisely ordered mesoporous architecture with significantly enhanced surface area serves dual critical functions: (i) as a nanoconfined porous buffer layer that mitigates localized current density fluctuations through spatial charge redistribution, and

(ii) as a selective ion-sieving filter that regulates Zn^{2+} flux distribution via combined steric confinement and surface charge effects, thereby enabling spatially homogeneous nucleation and deposition[122]. It was reported that the introduction of dopamine can also significantly improve the antioxidant and anti-stacking capability of MXene sheets[123].

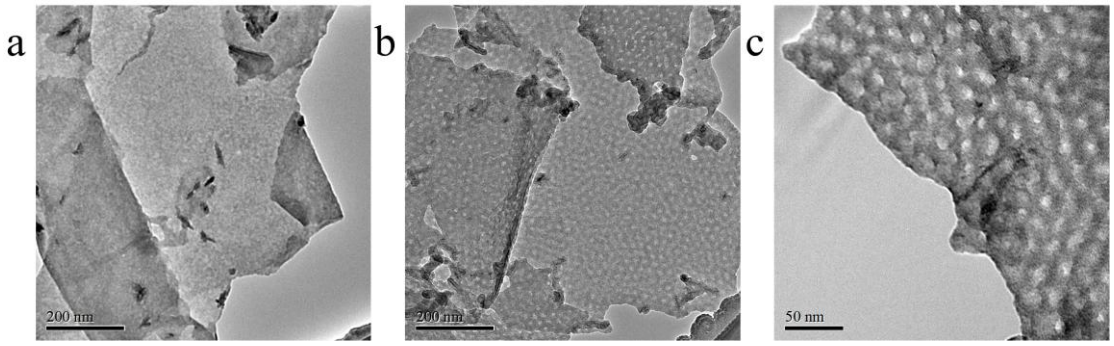

Figure 3.2 TEM images of (a) MXene, (b, c) MPP sheets.

Comprehensive microscopic and spectroscopic characterization confirms the successful formation of the MPP composite structure. High-resolution TEM imaging coupled with EDS elemental mapping (Figure 3.3) unambiguously demonstrates the conformal coating of mesoporous polydopamine (PDA) on MXene-derived MPP flakes, as evidenced by: (i) homogeneous nitrogen distribution throughout the composite, and (ii) well-defined interfacial boundaries between components. AFM result (Figure 3.4a) reveals the composite thickness to be 20 nm. A comparative analysis of the X-ray diffraction (XRD) patterns for MXene, polydopamine (PDA), and the MPP composite (Figure 3.4b) reveals a systematic shift of the (002) diffraction peak to lower 2θ angles in MPP relative to pristine MXene. This peak displacement provides direct evidence for the successful intercalation of PDA molecules between MXene layers, resulting in an expanded gallery spacing that facilitates enhanced ion accessibility[124]. The enlarged *d*-space of MPP can facilitate electrolyte penetration and Zn ion migration through the MPP interlayers to Zn metal anode to be discussed later.

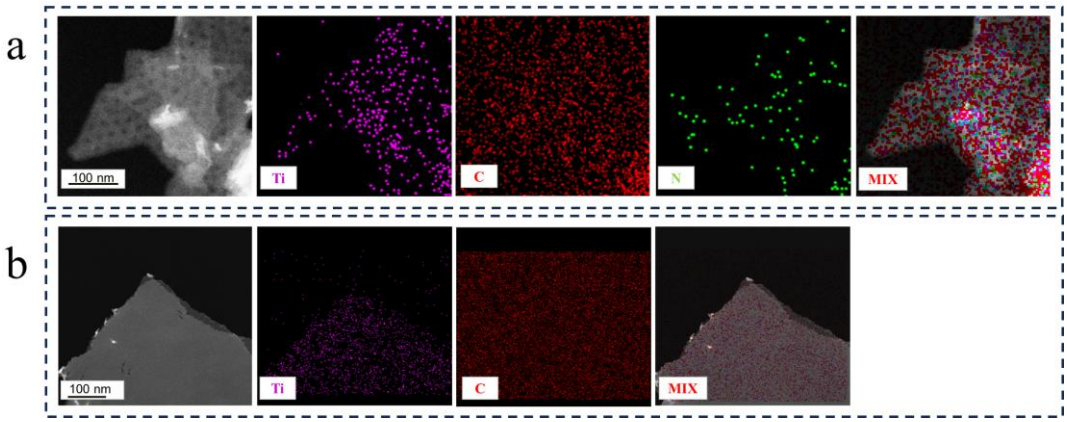

Figure 3.3 TEM images and EDS elemental mappings of (a) MPP and (b) MXene flakes. Note that the carbon film substrate in the TEM grid may disturb the carbon elemental detection.

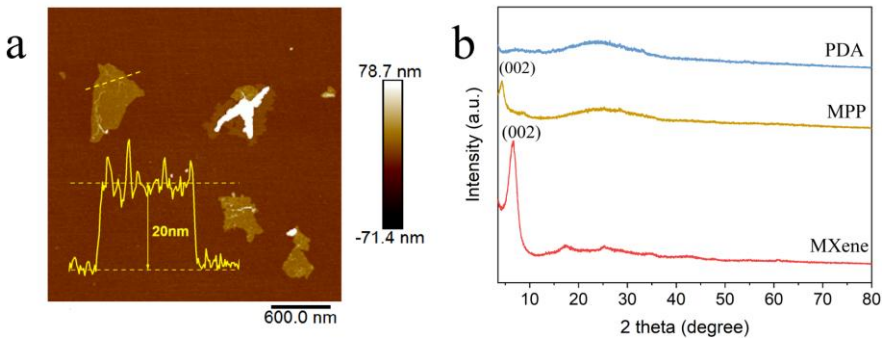

Figure 3.4 (a) AFM image and the thickness profile for MPP flakes. (b) XRD patterns of PDA, MXene and MPP.

The chemical composition and bonding states of the MPP composite were systematically investigated by X-ray photoelectron spectroscopy (XPS). As shown in Figure 3.5a, the survey scan of MPP exhibits significantly enhanced N 1s (399.5 eV) and C 1s (283.6 eV) core-level intensities compared to pristine MXene, arising from the successfully coated PDA layer. Figure 3.5b shows the deconvoluted N 1s spectra of MXene and MPP. No N peaks were detected in MXene, in contrast, MPP shows significant peaks at 398.7 eV, 400.1 eV and 397.3 eV, referring to the R-NH, R-NH_2 and R=N-R functional groups in PDA[125]. The N-Ti peeks at 396.1 eV in the N 1s curve (Figure 3.5b) and at 455.9 eV in Ti 2p spectrum (Figure 3.5c) indicated the strong chemical binding between the amine groups in PDA and dangling Ti atoms on MXene[126],[127]. The deconvoluted C1s spectra in Figure 3.6a and O1s in Figure 3.6b also

evidenced strong affinity between the MXene skeleton and the PDA layer with catechol-titanium coordination bonds (C-O-Ti) at 286.9 eV and 531.5 eV[128]. The interaction between MXene and PDA was also characterized by Fourier transform infrared (FTIR) as shown in Figure 3.6c. The new peaks at 1482 and 1253 cm^{-1} (ν_{CH2}) for MPP suggested the binding between catechols/quinone groups in PDA and the −OH/−F terminal groups of MXene[129]. The robust chemical interactions within the MPP architecture ensure exceptional structural stability during prolonged cycling in aqueous zinc-ion batteries (AZIBs). Furthermore, the synergistic combination of polydopamine's multifunctional groups (amine, imine, and catechol) with titanium oxide coordination complexes creates a highly efficient ion-trapping network[125], thus homogenizing Zn ion diffusion for smooth Zn metal deposition.

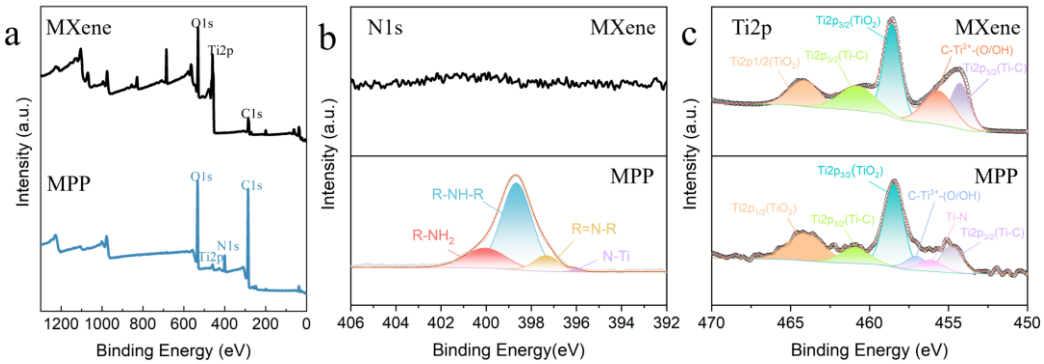

Figure 3.5 (a) Full XPS spectra of MXene and MPP. (b) XPS spectra of N1s peaks for the MXene and MPP. (c) XPS spectra of Ti2p peaks for the MXene and MPP.

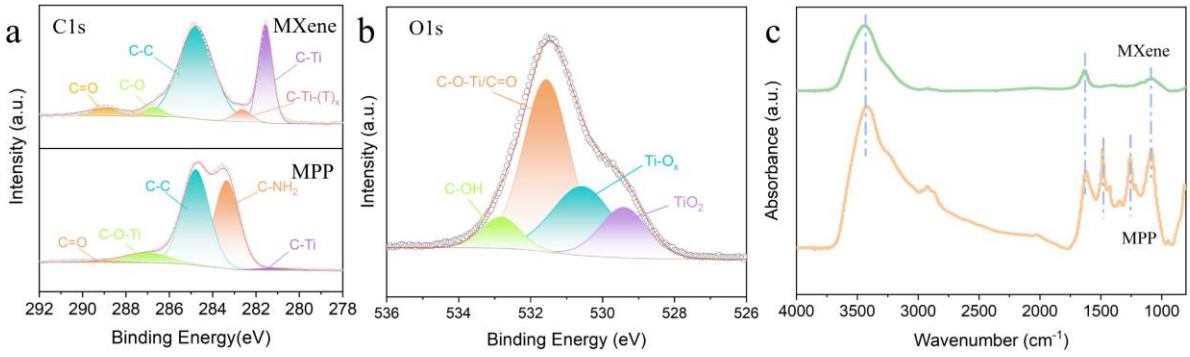

Figure 3.6 (a) XPS spectra of C1s peaks for the MXene and MPP. (b) XPS spectra of O1s peaks for the MPP. (c) FTIR spectra of MXene and MPP.

The exceptional physicochemical properties of the MPP nanocomposite render it an ideal candidate for engineering high-performance zinc metal anodes through surface modification. A uniform MPP coating was precisely deposited on zinc foil substrates via optimized spin-coating parameters, achieving a conformal interfacial layer with an average thickness of 2 μm (Figure 3.7a), which ensures negligible impact of electrochemical inert interlayer on the overall energy density of AZIBs. Comparative analysis reveals that the MPP-modified Zn anode exhibits superior coating uniformity relative to its MXene-coated counterpart (Figure 3.4b), attributable to the synergistic effects of polydopamine's hydrophilic catechol groups (–OH) and zincophilic nitrogen moieties (–NH/N=). High-resolution SEM coupled with EDS elemental mapping (Figure 3.7c-g) demonstrates exceptional spatial homogeneity of the MPP coating, which further reflects the homogeneity of MPP coating. Electrolyte wettability serves as a critical interfacial parameter that fundamentally governs three key electrochemical processes in zinc metal anodes: (i) hydrated Zn^{2+} diffusion kinetics, (ii) maximum power density capability , and (iii) long-term interfacial stability[130]. Figure 3.8 demonstrates significantly enhanced electrolyte wettability of the MPP-modified Zn anode, with the 2M $ZnSO_4$ aqueous electrolyte exhibiting a contact angle of 50° on MPP-Zn compared to 104° on pristine Zn foil, confirming the critical role of MPP's hydrophilic functional groups in establishing an optimal electrode-electrolyte interface for efficient Zn^{2+} diffusion.

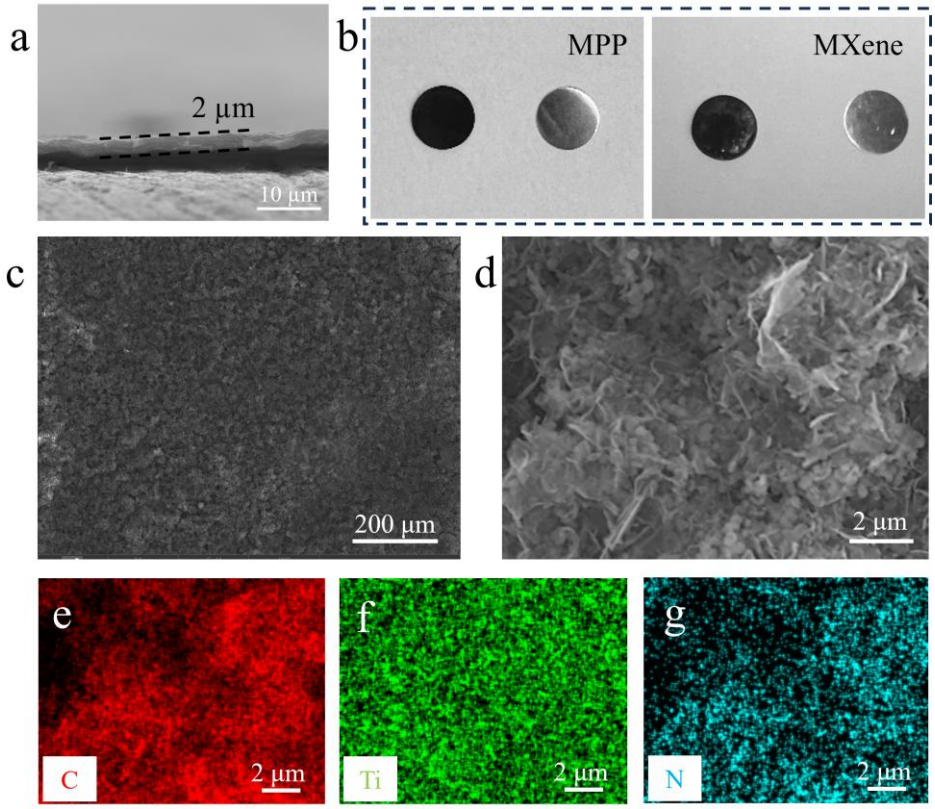

Figure 3.7 (a) Cross-sectional SEM image of MPP-Zn. (b) MPP-Zn and MXene-Zn electrodes in comparison with bare Zn. (c-d) Top view SEM images and (e-g) EDS elemental mappings for MPP-Zn anodes with uniform MPP coating on the surface of Zn metal.

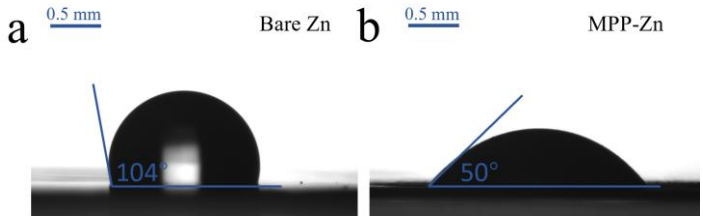

Figure 3.8 Electrolyte/interlayer contact angles for (a) bare Zn and (b) MMP-Zn electrodes.

3.2.2 Morphological evolution of Zn metal deposition

To systematically evaluate the protective efficacy of the MPP interfacial layer on zinc metal anodes, we conducted comprehensive morphological and electrochemical characterization of both MPP-Zn and bare Zn electrodes under varied deposition conditions. Figures 3.9a and 3.9b present comparative scanning electron microscopy (SEM) images and corresponding electrochemical deposition profiles of Zn||Zn symmetric cells with and without MPP protective interlayers, evaluated at three discrete areal capacities (1, 3, and 5 mAh cm^{-2}) under a constant

current density of 1 mA cm^{-2}. Throughout the plating process, the MPP-Zn electrode maintains a lamellar morphology completely devoid of dendritic protrusions or metallic whiskers (Figure 3.9a), as further corroborated by cross-sectional analysis revealing exceptionally dense and smooth zinc deposition layers. In stark contrast, bare Zn electrodes exhibit irregular, granular zinc deposition that progressively deteriorates with increasing areal capacity. Under 5 mAh cm^{-2} deposition conditions, severe morphological degradation manifests as loosely aggregated, porous zinc clusters penetrating the glass fiber separator. The uncontrolled deposition behavior observed on bare Zn anodes originates from the preferential Zn^{2+} nucleation at initial protrusions, where subsequent deposition follows the energetically favorable growth pathways, ultimately exacerbating dendritic and mossy zinc formation through a self-amplifying mechanism[131].

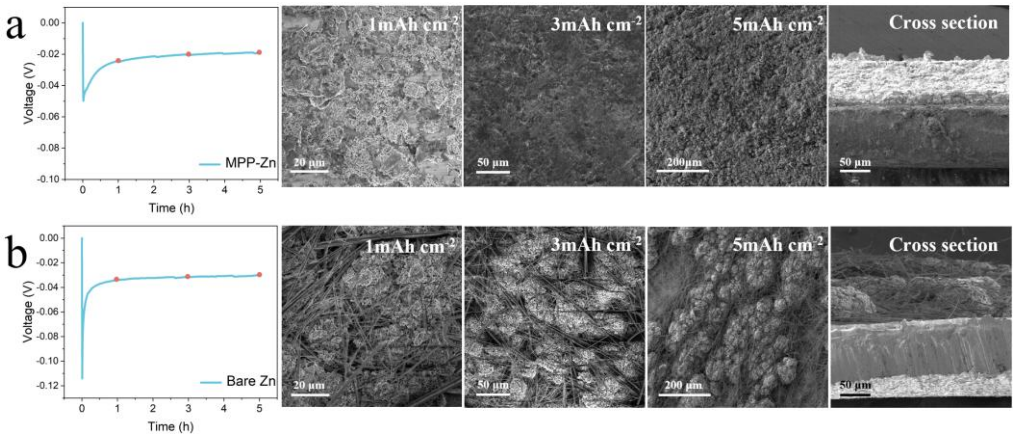

Figure 3.9 The first Zn deposition voltage profiles and SEM images of plated Zn on (a) MPP-Zn and (b) bare Zn in symmetric cells at increasing capacities of 1, 3, and 5 mAh cm^{-2}. Right of (a, b) showing cross-section view of 5 mAh cm^{-2} plated Zn.

Furthermore, we employed *in situ* optical microscopy to monitor the macroscopic morphological evolution at the electrode/electrolyte interface for both bare Zn and MPP-Zn electrodes during various plating stages (Figure 3.10). Both pristine electrodes exhibited flat surfaces initially. Upon galvanostatic deposition at 1 mA cm^{-2} for 30 minutes, microscopic protrusions became discernible on the bare Zn surface. These pre-existing protrusions

subsequently exacerbated the heterogeneous distribution of both electric fields and ion fluxes at the electrode/electrolyte interface. After 60 minutes of electrodeposition, the bare Zn electrode surface became densely covered with severe zinc dendrites, exhibiting pronounced morphological heterogeneity. In contrast, the MPP-Zn electrode maintained an exceptionally smooth surface topography throughout the entire plating process without observable dendritic formation. These results demonstrate that the MPP interlayer can effectively mitigate the dendritic growth issues inherent to zinc metal anodes.

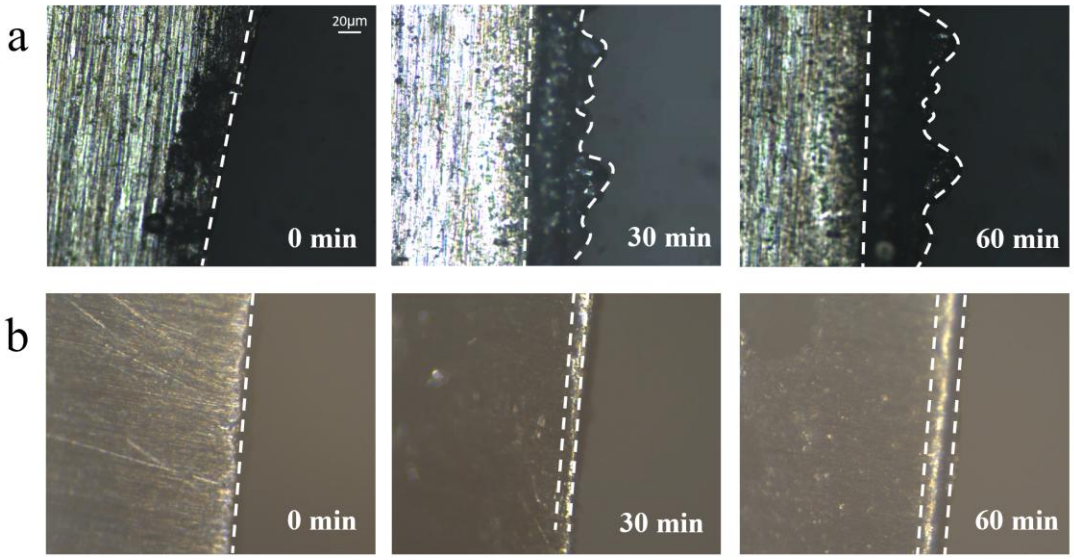

Figure 3.10 In-situ optical microscopic visualization of the Zn plating behaviors on (a) bare Zn and (b) MPP-Zn at 1 mA cm^{-2} for 60 min.

To elucidate the zinc deposition mechanism at the molecular level, we performed chronoamperometric (CA) analysis (Figure 3.11a). This electrochemical technique precisely monitors current-time transients at a fixed overpotential, enabling quantitative characterization of both nucleation kinetics and dynamic surface evolution during electrodeposition[68]. Upon application of a -150 mV overpotential to the bare Zn electrode, the current density exhibited sustained growth over 500 seconds, indicative of prolonged two-dimensional propagation through rough deposition processes. This phenomenon suggests that Zn^{2+} ions adsorbed near the metal surface undergo lateral diffusion to locate energetically favorable sites for charge

transfer, consistent with progressive surface roughening mechanisms observed in unregulated deposition systems. Due to the "tip effect", surface protrusions exhibit enhanced electric field intensity, which directs Zn^{2+} ion diffusion toward these sites to minimize both surface energy and exposed area, ultimately leading to localized zinc accumulation and dendritic growth. In contrast, the MPP-Zn electrode demonstrates distinct deposition kinetics: (i) rapid nucleation and lateral diffusion occurring within the initial 100 s, followed by (ii) a three-dimensional diffusion phase maintaining a stable current density of 17.5 mA cm^{-2}, indicative of spatially homogeneous deposition behavior. This distinct behavior originates from the abundant N- and O-containing functional groups on the MPP film surface, where zincophilic sites effectively capture and redistribute Zn^{2+} ion fluxes, thereby enabling uniform three-dimensional diffusion of zinc ions across the electrode interface[132]. Post-cycling characterization of the interphase components via XPS analysis revealed C-N=O bonding signatures derived from PDA-$[Zn(H_2O)_6]^{2+}$ interactions (Figure 3.11b), providing direct spectroscopic evidence for both Zn^{2+} ion capture and redistribution mechanisms at the functional interface[133] and the N-Zn bond in the N1s spectra indicating that N atoms in the MPP can chemically bond with Zn ions (Figure 3.11c)[134].

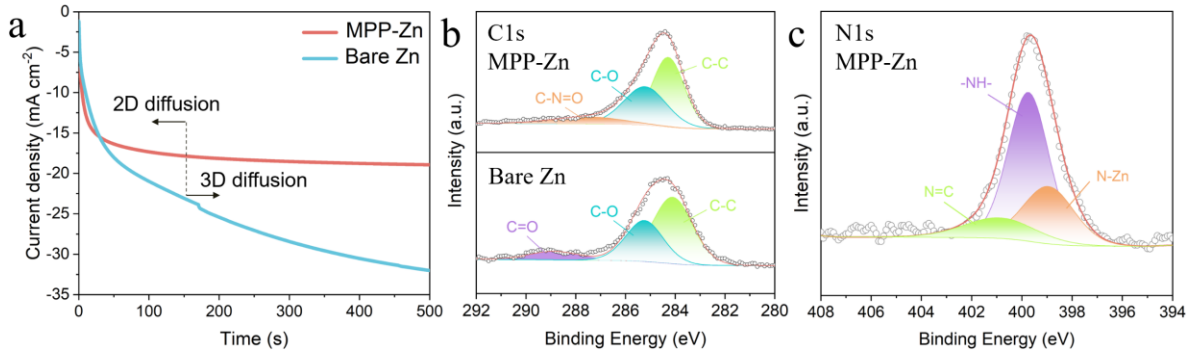

Figure 3.11 (a) Chronoamperometry curves of MPP-Zn and bare Zn electrodes under an overpotential of -150 mV. (b) C 1 s spectra for MPP-Zn and bare Zn electrodes after 5 hrs plating. (c) The high-resolution N 1s XPS spectra of cycled MPP-Zn.

The homogeneous Zn^{2+} diffusion and three-dimensional current distribution enabled by the MPP layer ultimately yielded smooth, compact zinc metal deposition on the electrode surface.

This distinct growth mechanism was further verified through comparative AFM characterization of both bare Zn and MPP-Zn electrodes (Figure 3.12a and 3.12b). After 50 deposition/stripping cycles, the morphological contrast between MPP-Zn and bare Zn electrodes became markedly pronounced, with the latter exhibiting extensive zinc aggregates and large dendritic crystallites (Figure 3.12c and 3.12d). As demonstrated in Figure 3.13, the MPP interlayer maintains exceptional structural integrity after repeated zinc plating/stripping cycles, with no observable morphological degradation, confirming the outstanding electrochemical durability of this engineered interface material.

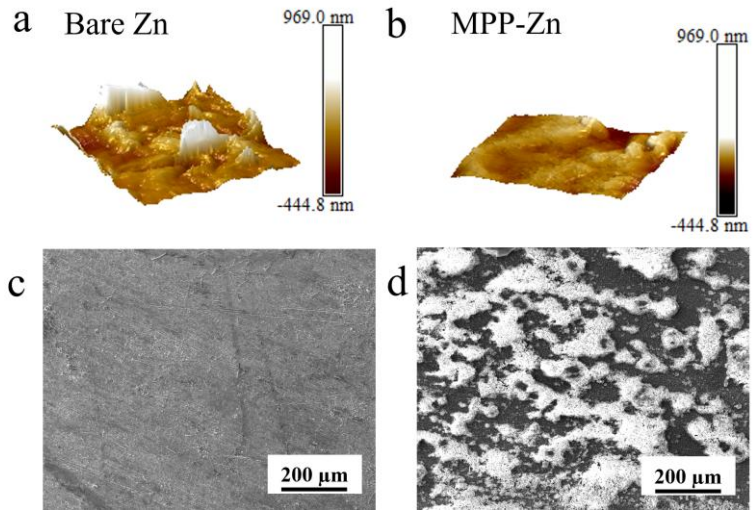

Figure 3.12 AFM images of (a) bare Zn and (b) MPP-Zn anode after 5h Zn plating process. SEM images of (c) MPP-Zn and (d) bare Zn after 50 cycles at 1 mA cm^{-2}.

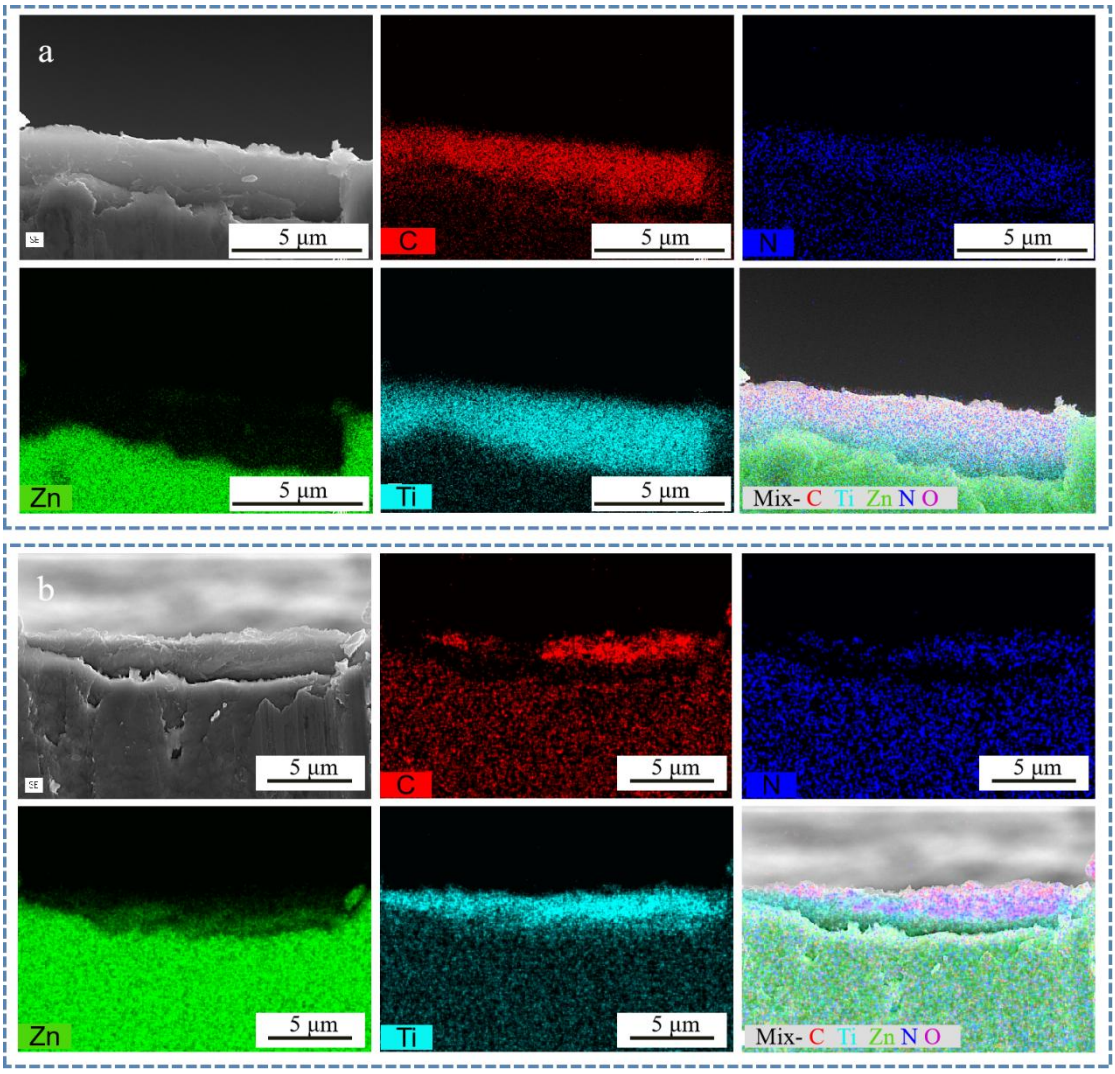

Figure 3.13 Cross sectional SEM images and EDS mappings for MPP-Zn electrodes (a) before and (b) after 50 cycles at 1 mA cm^{-2} and 1 mAh cm^{-2}. The conformal MPP nanocoating maintains uniform coverage across the zinc substrate without observable degradation after electrochemical cycling. It should be noted that the apparent edge delamination observed at the MPP/Zn interface constitutes a preparation artifact arising from mechanical sectioning and thermal drying protocols, which induce localized wrinkling in the ultrathin polymeric film.

3.2.3 Anticorrosion, desolvation and homogenization effects

The parasitic reactions and corrosion of zinc metal in aqueous electrolytes represent another persistent challenge for Zn-based anodes. To systematically evaluate the protective efficacy of the MPP coating, both bare Zn and MPP-Zn foils were subjected to a 10-day immersion test in 2 M $ZnSO_4$ aqueous solution under controlled conditions. As clearly evidenced in Figure 3.14a,

the bare Zn surface developed extensive micro-sized flake-like byproducts, which were unambiguously identified as $Zn_4SO_4(OH)_6 \cdot 5H_2O$ phase through XRD analysis (Figures 3.14b and 3.14c). These corrosion byproducts originate from the detrimental hydrogen evolution reaction (HER) between water and metallic zinc, a parasitic process that significantly compromises both mass transport uniformity and charge transfer kinetics at the electrode-electrolyte interface[135]. In striking contrast, the MPP-Zn anode maintained essentially pristine surface morphology with preserved flatness and smoothness after immersion (Figure 3.15a). The intact interfacial architecture and complete absence of $Zn_4SO_4(OH)_6 \cdot 5H_2O$ corrosion products conclusively demonstrate the MPP coating's dual functionality: (i) exceptional anti-corrosion capability and (ii) robust protective performance, effectively shielding the vulnerable zinc metal from aqueous electrolyte degradation mechanisms[136].

The corrosion inhibition effect of the MPP coating was quantitatively verified through linear polarization experiments. As shown in Figure 3.15b, the MPP-Zn electrode exhibits superior corrosion resistance compared to bare Zn, demonstrating: (i) a more noble corrosion potential (Ecorr = -0.961 V vs -0.974 V) and (ii) a significantly reduced corrosion current density (icorr = 2.83 mA cm^{-2} vs 4.13 mA cm^{-2}). These electrochemical parameters confirm the fundamental corrosion thermodynamics and kinetics - the anodic shift in Ecorr indicates lower thermodynamic corrosion tendency, while the decreased icorr reflects improved kinetic corrosion resistance[137]. Linear sweep voltammetry (LSV) was employed to systematically characterize the hydrogen evolution reaction activity of bare Zn, MXene-Zn, and MPP-Zn electrodes. As demonstrated in Figure 3.15c, the MPP-Zn electrode exhibits the lowest exchange current density, which correlates well with its reduced corrosion current density observed in Figure 3.15b. This consistent electrochemical behavior provides compelling

evidence that the MPP coating effectively suppresses chemical corrosion of zinc metal in aqueous electrolytes through HER inhibition.

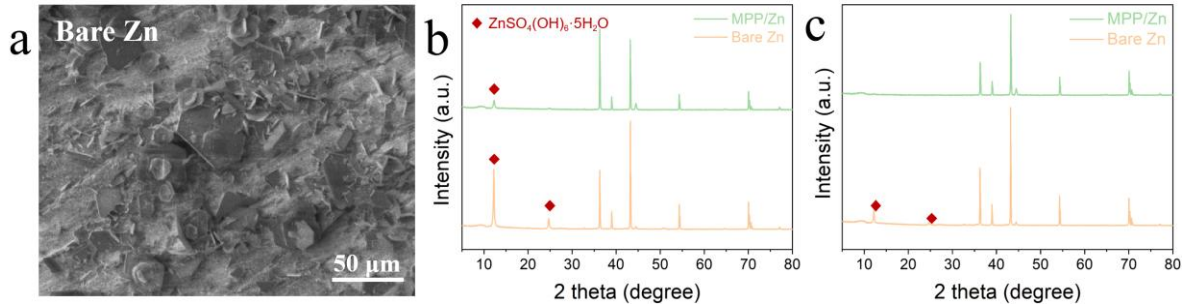

Figure 3.14 (a) SEM image of bare Zn foil immersed in 2 M $ZnSO_4$ aqueous electrolyte for 10 days showing large flaky byproduct. XRD patterns of (b) pristine Zn foil and MPP-Zn after being immersed in 2 M $ZnSO_4$ electrolytes for 10 days and (c) MPP-Zn and pristine Zn after 50 cycles at 1mA cm^{-2}.

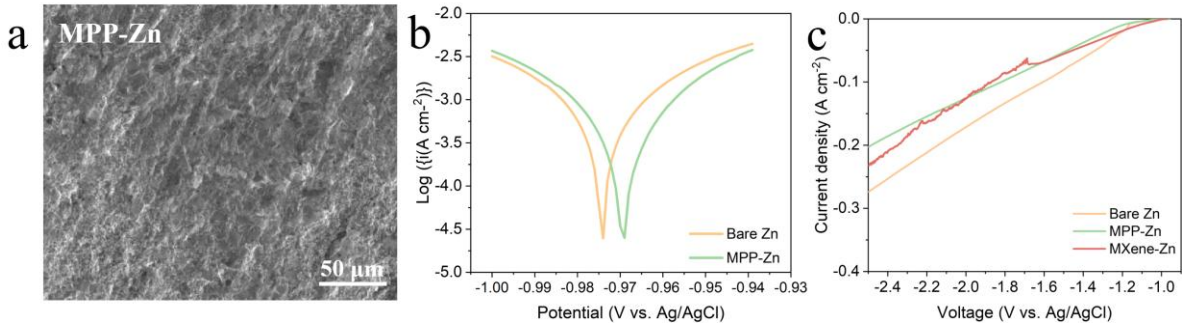

Figure 3.15 (a) SEM image of MPP-Zn electrode soacked in 2 M ZnSO4 electrolyte for 10 days. (b) Linear polarization curves showing corrosion of MPP-Zn and bare Zn electrodes. (c) LSV curves of bare Zn, MPP-Zn, and MXene-Zn at a scan rate of 5 mV s^{-1} in 2 M $ZnSO_4$ aqueous solution.

To systematically validate the corrosion-resistant performance of the MPP layer in cycled aqueous zinc-ion batteries (AZIBs), we conducted comprehensive chemical structure analysis of both cycled bare Zn and MPP-Zn electrodes using X-ray photoelectron spectroscopy (XPS) characterization (Figures 3.16a-c). The deconvoluted O1s spectrum of bare zinc showed strong peaks at 533.4 eV and 531.5 eV referring to the O-H and Zn-OH bonds from the $Zn_4SO_4(OH)_6 \cdot 5H_2O$ byproduct[138, 139]. This comparative analysis reveals significant parasitic reactions occurring on the bare Zn surface during electrochemical cycling, as evidenced by

distinct characteristic peaks. In contrast, the complete absence of such degradation signatures in the MPP-Zn spectra confirms the effective passivation capability of the engineered interfacial layer. The Zn 2p3/2 peak at 1021.9 eV for MPP-Zn (Figure 3.16c) refers to Zn metal, whereas the deconvoluted Zn 2p3/2 for bare Zn consists two peaks at 1022.2 and 1023.1 eV, corresponding to ZnO and $Zn(OH)_2$, respectively[140]. During electrochemical cycling, the accumulation of insoluble interphase compounds (e.g., ZnO or $Zn(OH)_2$) on bare Zn electrodes progressively passivates the active surface, resulting shorten cycle life and increased polarizations.

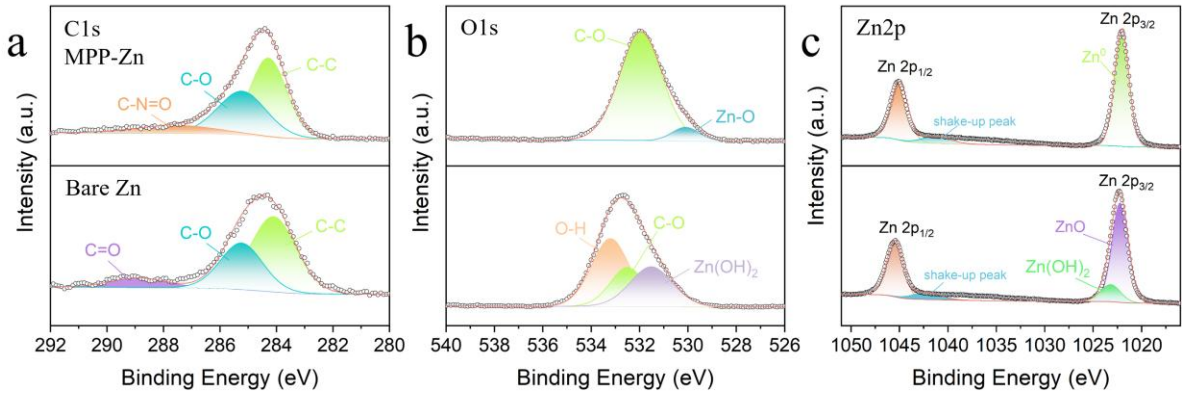

Figure 3.16 (a) C 1s, (b) O 1s, and (c) Zn 2p spectra for MPP-Zn and bare Zn electrodes after 5 hrs plating.

The anti-corrosion capability can be related to the desolvation effect of MPP coating layer on the Zn metal. In an aqueous system, the Zn^{2+} ions are coordinated with six water molecules to form $[Zn(H_2O)_6]^{2+}$, which needs to be de-solvated before being reduced on the Zn metal surface. As revealed by density functional theory (DFT) calculations in Figure 3.17a, the adsorption energies of water molecules on MXene, MPP, and Zn^{2+} were determined to be -0.36 eV, -0.46 eV, and -0.23 eV, respectively. This energetics analysis demonstrates that MPP exhibits exceptionally strong interactions with water molecules in solvated Zn^{2+} complexes, surpassing both MXene and bare zinc ions in hydration affinity. Furthermore, the MPP coating demonstrates exceptional wettability toward the $[Zn(H_2O)_6]^{2+}$ electrolyte (Figure 3.8), enabling: (i) enhanced permeation of solvated zinc complexes, (ii) effective water molecule

trapping via hydrogen bonding networks, and (iii) direct Zn^{2+} reduction on the metallic substrate - a synergistic mechanism that optimizes interfacial ion transport and deposition kinetics. To mitigate water decomposition on the metal anode, strategic reduction of Zn^{2+}-water coordination strength proves effective. DFT calculations reveal strong binding between MPP and Zn atoms (Figure 3.17b), facilitated by the material's abundant functional groups. Consequently, the desolvated Zn^{2+} ions undergo stabilization and homogenization within the MPP matrix, followed by directed diffusion to the metallic substrate for subsequent deposition reactions, a process that ensures spatially uniform zinc plating with improved nucleation density.

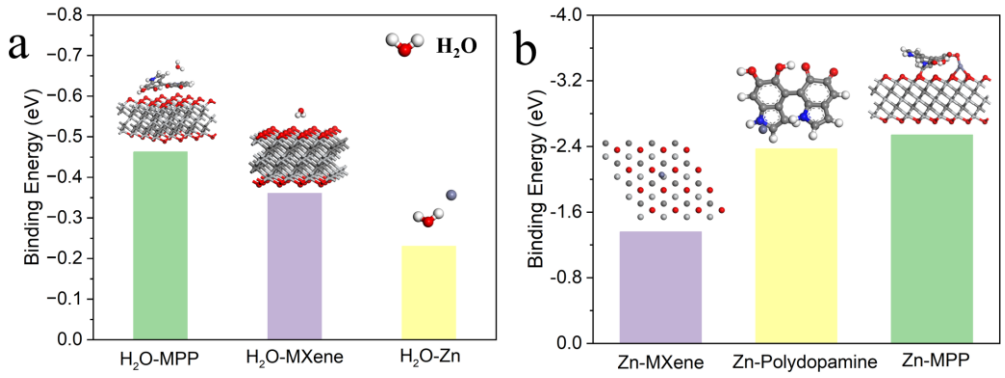

Figure 3.17 DFT calculated binding energies of (a) MXene, MPP, and Zn metal to H2O molecules, (b) binding energies of MXene, PDA and MPP to Zn atoms.

MPP can further effectively regulate the Zn ion diffusion and deposition through homogenizing and redistibuting functions. In contrast, while MXene exhibits exceptional electrical conductivity that facilitates zinc metal deposition on the MXene-Zn electrode surface (Figure 3.18a). This configuration proves undesirable as it ultimately compromises the surface-protective functionality of MXene, leading to progressive degradation of electrode performance. In contrast, no Zn metal deposits were observed within and on the surface of MPP layer (Figure 3.18b). The difference can be ascribed to the conformal coating of MXene with poorly conductive PDA[141]. Therefore, MPP layer synergies the merits of MXene and PDA by excluding potential snags. Moreover, the effect of mesopores on PDA on Zn^{2+}

distribution is investigated by the Transport of Diluted Species Interface calculation. Figures 3.19a and 3.19b comparatively visualize the spatial distribution profiles of Zn^{2+} concentration gradients across MXene and MPP interlayers, respectively, revealing fundamentally distinct ion transport mechanisms between these two architectures. In contrast to the tortuous Zn^{2+} diffusion pathways along inter-MXene sheet gaps observed in MXene-Zn, the mesoporous architecture of MPP enables effective redistribution of vertically aligned, field-driven ion fluxes through its interconnected channels - a structural advantage that ensures more homogeneous ion transport. Furthermore, quantitative analysis reveals that the Zn^{2+} ion concentration profile through the MPP interlayer exhibits significantly reduced fluctuation amplitude compared to MXene under equivalent testing conditions (Figures 3.20a and 3.20b), demonstrating superior ionic flux regulation capability of the mesoporous polymer architecture. Therefore, the mesopores on MPP also plays notable roles in homogenizing the Zn^{2+} diffusion for uniform Zn metal deposition.

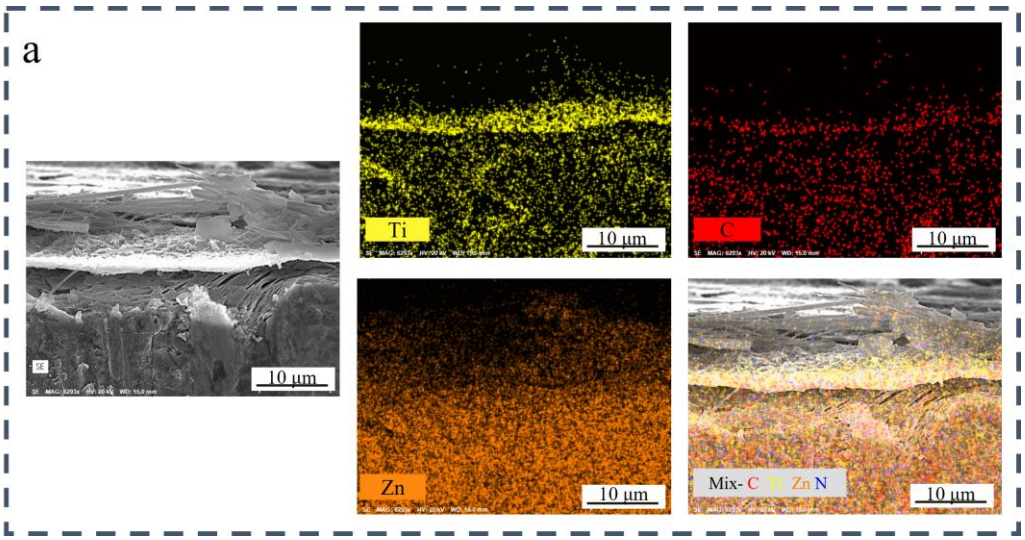

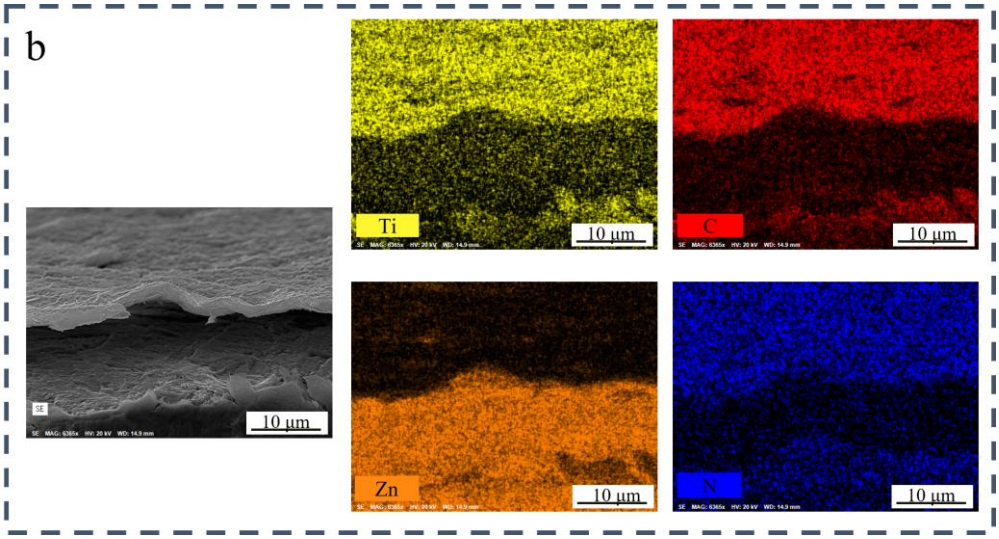

Figure 3.18 Cross sectional SEM images and EDS elemental mappings of (a) MXene-Zn and (b) MPP-Zn electrodes after 20 cycles at 1 mA cm^{-2} and 1mAh cm^{-2}.

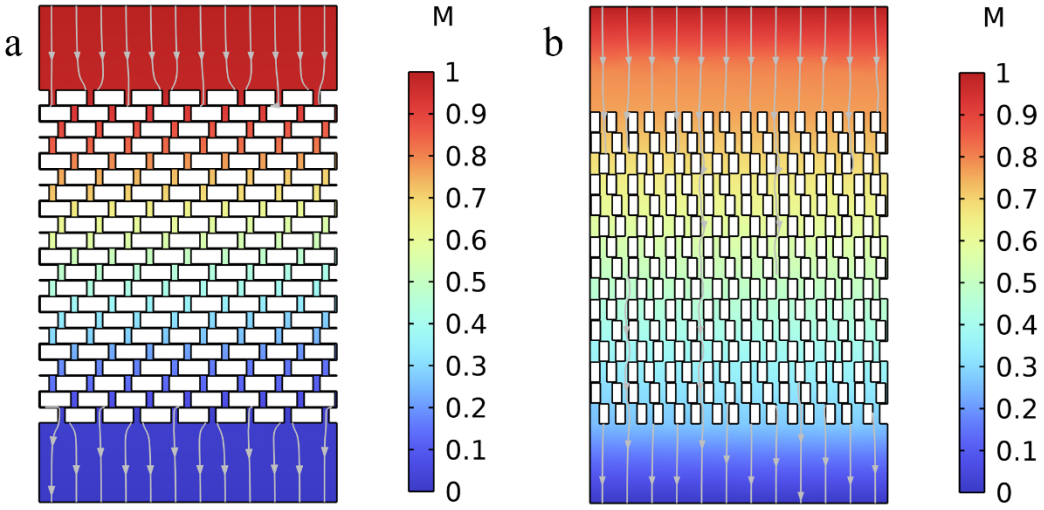

Figure 3.19 Model diagram of Zn ions diffusion through (a) MXene layer and (b) MPP layer (Inset: the color represents different concentration of Zn ions).

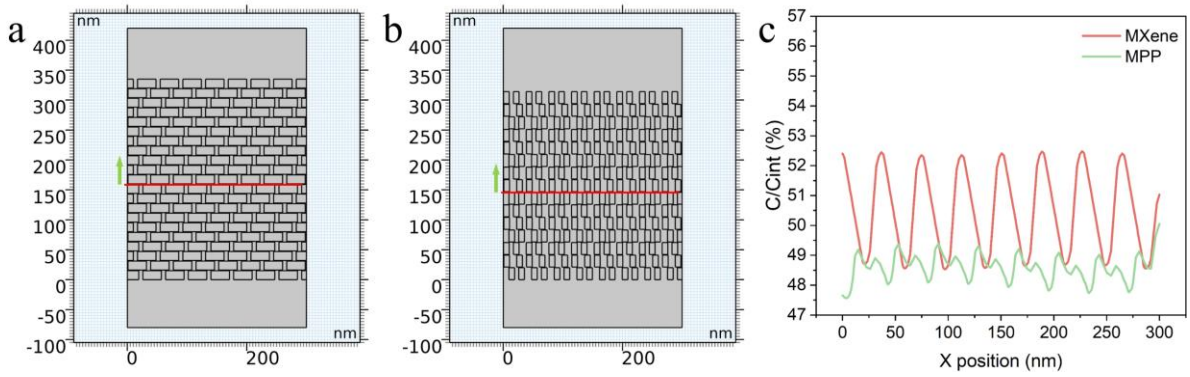

Figure 3.20 Geometrical specifics for modeling the Zn ion concentrations through (a) MXene layer and (b) MPP layer. (c) The relative concentration profiles of Zn ions beneath MXene and MPP layer at the same horizontal position.

The electric field distribution at the anode-electrolyte interface exerts significant influence on the reduction kinetics and deposition behavior of Zn^{2+} ions, governing both nucleation thermodynamics and subsequent growth morphology[142]. To elucidate the Zn^{2+} redistribution mechanism through the MPP interlayer, we performed COMSOL Multiphysics simulations to comparatively analyze the interfacial electric field and current density distributions between bare Zn and MPP-Zn electrodes, revealing fundamental differences in their ion regulation capabilities. For the MPP-coated zinc, the moderate conductivity of the PDA-incorporated MPP interlayer facilitates the establishment of a homogeneous electric field distribution (Figure 3.21b). This optimized field configuration enables: (i) uniform Zn^{2+} deposition and (ii) effective electrode protection against tip-induced field concentration - consistent with the smooth and compact zinc plating morphology observed in Figure 3.9a. In stark contrast, the bare Zn electrode exhibits pronounced local electric field heterogeneity concentrated at surface protrusions (Figure 3.21a), creating preferential Zn^{2+} deposition sites that exacerbate morphological instability. This intensely concentrated local electric field accelerates Zn^{2+} flux convergence at dendritic protrusions, creating an autocatalytic deposition process that: (i) amplifies dendrite growth and (ii) ultimately induces cell short-circuiting through metallic penetration of the separator. The current density distribution and zinc ion flux are intrinsically governed by electric field intensity. Building upon the simulated electric field profiles, we further modeled the current density distribution at the MPP-Zn interface, which demonstrates significantly improved uniformity compared to bare Zn (Figures 3.21c and 3.21d), confirming the effectiveness of the MPP layer in homogenizing electrochemical deposition. Consequently, under the influence of this homogenized electric field, the MPP film establishes uniform ion transport channels through precise regulation of Zn^{2+} fluxes. We postulate that the desolvation

and redistribution processes of Zn^{2+} across the engineered interphase layer may introduce substantial energy barriers for ion migration, thereby fundamentally altering the deposition thermodynamics[143].

We conducted electrochemical impedance spectroscopy (EIS) measurements on both bare Zn and MPP-Zn symmetric cells. The MPP-Zn configuration exhibited substantially lower charge transfer resistance (R_{ct}) compared to its bare Zn counterpart (Figure 3.22a), providing compelling evidence for the favorable ion transport kinetics enabled by the MPP interlayer architecture. To further elucidate the enhanced zinc deposition kinetics enabled by the zincophilic MPP coating, we quantitatively analyzed the dissociation dynamics of Zn^{2+} through the MPP interlayer by calculating the activation energy (E_a), providing fundamental insights into the interfacial charge transfer mechanisms[144]. Figure 3.22b presents the temperature-dependent electrochemical impedance spectroscopy (EIS) profiles (30-70°C) for four distinct electrode configurations: bare Zn, MPP-Zn, MXene-Zn, and MP-Zn (non-porous polydopamine/MXene composite), providing a comprehensive comparative analysis of their interfacial charge transfer characteristics. Across the investigated temperature range, the MPP-Zn anode demonstrates significantly lower R_{ct} values compared to the other three electrode systems (Figure 3.22c), quantitatively confirming enhanced charge transfer kinetics in the MPP-Zn battery configuration. According to the Arrhenius equation, the activation energy (E_a) for MPP-Zn was determined to be 10.64 kJ mol^{-1}, representing approximately one-third of the value measured for bare Zn (E_a = 33.26 kJ mol^{-1}), which conclusively demonstrates the kinetic advantage of the engineered interphase. Benefiting from the synergistic effects of enhanced dissociation kinetics and homogenized ion flux, the MPP interlayer guarantees rapid and dendrite-free zinc metal plating/stripping processes, establishing an optimal electrochemical environment for reversible zinc deposition. Notably, the non-porous PDA-based MP-Zn electrode exhibits substantially higher activation energy (E_a) and charge transfer resistance (R_{ct})

values compared to its mesoporous MPP-Zn counterpart, unambiguously demonstrating the critical role of mesoporosity in regulating Zn^{2+} dissociation kinetics at the electrode-electrolyte interface.

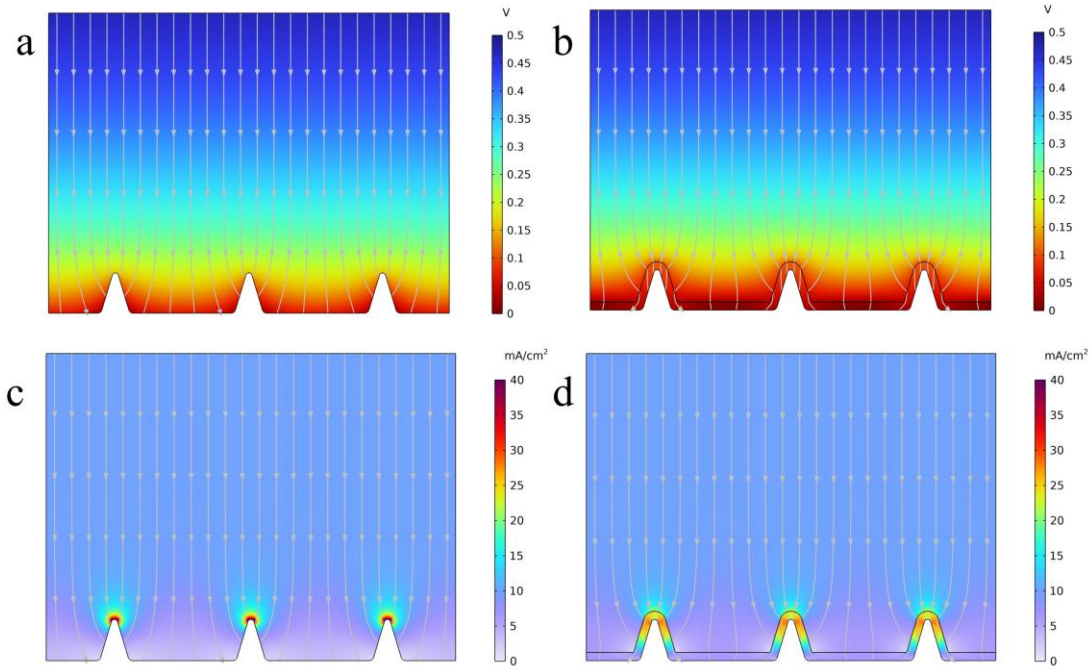

Figure 3.21 COMSOL simulated electric field distributions on the surface of (a) bare Zn and (b) MPP-Zn. The simulations of the electric field distribution and current density distribution on the (c) bare Zn and (d) MPP-Zn.

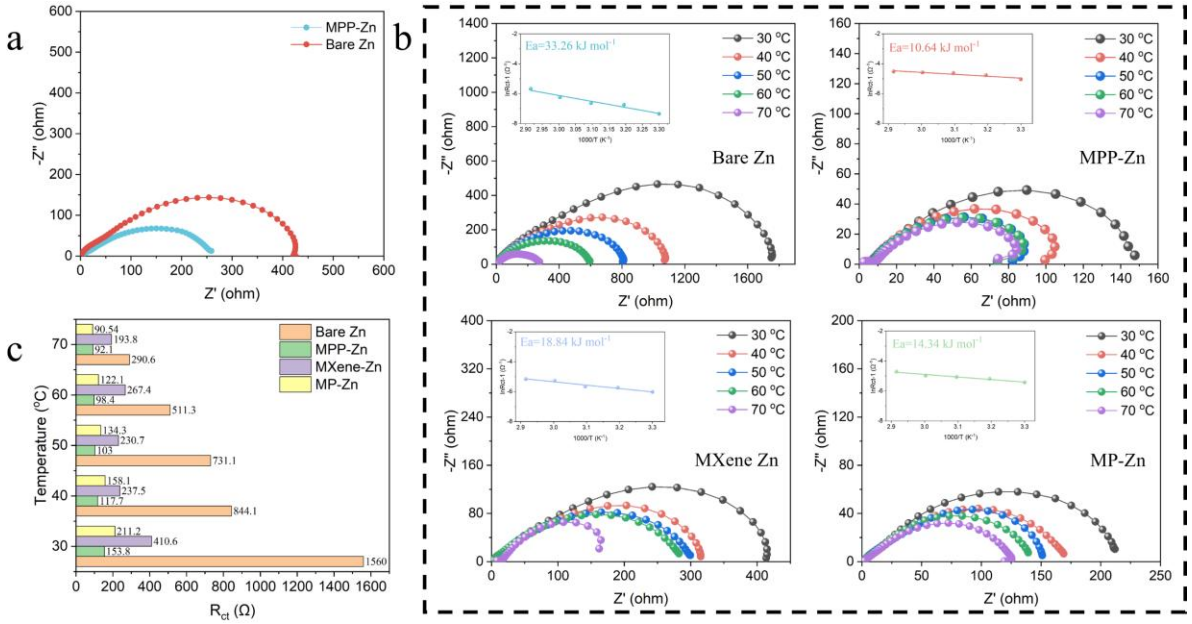

Figure 3.22 (a) Nyquist plots of fresh bare Zn//bare Zn and MPP-Zn//MPP-Zn symmetric cells. (b) Nyquist EIS plots of bare Zn, MPP-Zn, MXene-Zn and MP-Zn electrodes at different

temperatures. Insets are the equivalent circuits and plots to calculate the desolvation activation energies (E_a) by using the Arrhenius equation: $\frac{1}{R_{ct}}=Aexp(\frac{-E_a}{RT})$, where R_{ct}, A, R, T refers the charge transfer resistance at different temperatures, the pre-exponential factor, the universal gas constant, and the absolute temperature, respectively. (c) R_{ct} values of bare Zn, MPP-Zn, MXene-Zn and MP-Zn measured at different temperatures ranging from 30 to 70 ºC.

3.2.4 Electrochemical performance

Figure 3.23a shows the first discharge voltage profiles in asymmetric cells at 1 mA cm^{-2}. The MPP-Zn//Cu cell demonstrates a significantly lower nucleation overpotential (27.9 mV) compared to the bare Zn//Cu configuration (33.3 mV), providing direct electrochemical evidence for the enhanced deposition kinetics enabled by the MPP interface engineering. To systematically demonstrate the advantages of the MPP coating in stabilizing zinc metal anodes, we assembled both symmetric and asymmetric cell configurations for long-term cycling tests under practical operating conditions (1 mA cm^{-2} current density, 1 mAh cm^{-2} areal capacity). As shown in Figure 3.23b, the MPP-Zn symmetric cell achieves an exceptional cycling lifespan exceeding 1000 hours, representing approximately an order-of-magnitude improvement compared to both bare Zn and MXene-Zn based configurations. The pronounced voltage fluctuations observed in both bare Zn and MXene-Zn based symmetric cells originate from three detrimental factors: (i) cumulative parasitic reactions, (ii) progressive interfacial passivation, and (iii) dendrite-induced short-circuiting - collectively reflecting the inherent instability of unmodified zinc anodes under prolonged cycling.

Depth of discharge (DOD) serves as a critical parameter for evaluating the practical viability of zinc metal anodes. Utilizing ultrathin zinc foils (10 μm thickness), both bare Zn and MPP-Zn electrodes were cycled at a high DOD of 20% under 1 mA cm-2 current density (Figure 3.23c), establishing rigorous testing conditions to assess their electrochemical stability limits. Under these demanding testing conditions, the MPP-Zn symmetric cell demonstrates exceptional cycling stability exceeding 500 hours - a performance metric that rivals state-of-

the-art DOD capabilities reported in the literature, thereby validating the practical potential of this interfacial engineering approach[145-147]. Furthermore, we systematically evaluated the Coulombic efficiencies (CEs) of asymmetric Zn//Cu cells to quantitatively assess the plating/stripping reversibility (Figure 3.23b), establishing a critical metric for evaluating the electrochemical stability of zinc deposition processes. The results demonstrate that the MPP-Zn configuration maintains exceptional Coulombic efficiency (CE) above 98.6% over 900 cycles, showcasing outstanding electrochemical reversibility. In stark contrast, both bare Zn and MXene-Zn electrodes experience complete failure after merely 100 and 250 cycles respectively, accompanied by significant CE fluctuations - highlighting the superior cycling stability achieved through MPP interface engineering.

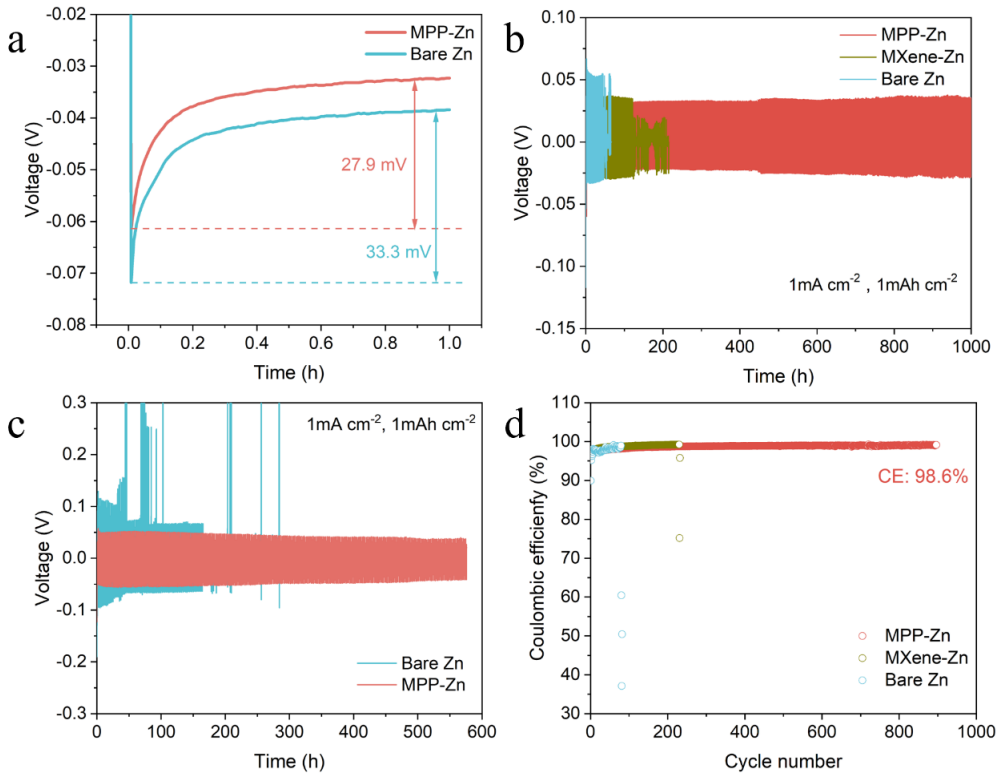

Figure 3.23 (a) Nucleation overpotential of MPP-Zn and bare Zn in asymmetric cell (vs. Cu electrode) at 1.0 mA cm^{-2}. (b) Long-term cycling of bare Zn//bare Zn, MXene-Zn//MXene-Zn, and MPP-Zn//MPP-Zn symmetrical cells at 1 mA cm^{-2} and 1 mAh cm^{-2}. (c) MPP-Zn//MPP-Zn and bare Zn//bare Zn cells cycling at a DOD = 20%. (d) CE profiles of bare Zn||Cu, MXene-Zn//Cu, and MPP-Zn||Cu asymmetric cells at 1 mA cm^{-2}.

Electrode overpotential, particularly under high current density conditions, represents a fundamental parameter for practical full-cell applications. Accordingly, we systematically evaluated bare Zn, MXene-Zn, and MPP-Zn electrodes in symmetric cell configurations across a broad current density range (0.5-8 mA cm^{-2}), as shown in Figure 3.24a, to comprehensively assess their rate capability and interfacial charge transfer characteristics. The MPP-Zn//MPP-Zn symmetric cell consistently maintains the lowest voltage polarization across increasing current densities, demonstrating only marginal hysteresis elevation - a characteristic that underscores its superior kinetic response and interfacial charge transfer efficiency compared to conventional zinc electrodes. We also quantified the overpotentials at different current densities in Figure 3.24b. For the MPP-Zn system, even when subjected to a 40-fold current density increase, the electrode overpotential exhibits only a moderate rise from 50 mV to 113 mV. The overpotentials for MXene-Zn//MXene-Zn and bare Zn//bare Zn cells revealed pronounced differences*, i.e.*, 85 to 492 mV for bare Zn-based cells and 72 to 187 mV for MXene-Zn-based cells. The MXene-Zn//MXene-Zn and bare Zn//bare Zn cells exhibit markedly different overpotential profiles, with the bare Zn configuration showing substantially higher values (85-492 mV) compared to its MXene-Zn counterpart (72-187 mV). Notably, the MPP-Zn electrode exhibits substantially reduced voltage hysteresis compared to other reported coated zinc metal anodes in the literature, demonstrating its superior interfacial charge transfer kinetics and electrochemical stability, *i.e.,* 200 mV for polyamide coated Zn[68], 200 mV for rGO coated Zn[148], and 160 mV for ZrO_2 coated Zn[149] (Figure 3.24c). The MPP-Zn electrode demonstrates superior electrochemical performance, including: (i) enhanced Coulombic efficiency (CE), (ii) extended cycle life, and (iii) exceptional rate capability - all attributable to the synergistic effects of homogeneous zinc deposition, suppressed parasitic reactions, and optimized ion diffusion kinetics at the engineered interface.

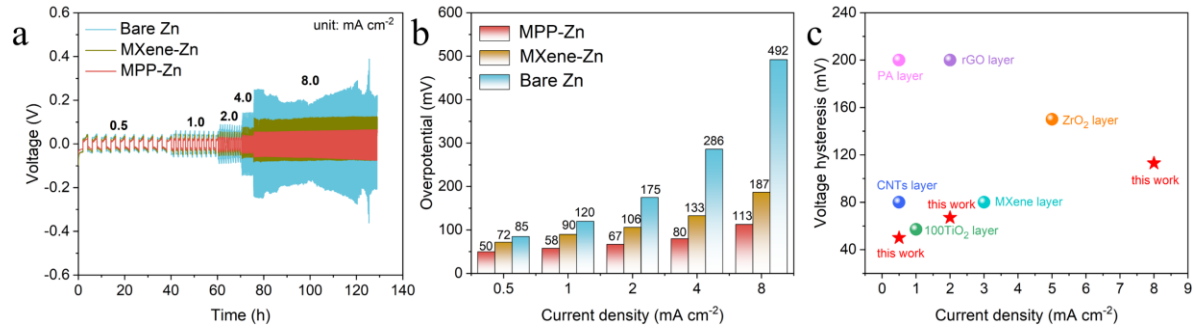

Figure 3.24 (a) Rate performances of the three kinds of symmetric cells at current densities from 0.5 to 8 mA cm^{-2} and a constant capacity of 1 mAh cm^{-2}, (b) the corresponding overpotentials derived from (a). (c) Comparison of voltage hysteresis of MPP-Zn//MPP-Zn symmetric cells cycling at high rates with peer Zn electrodes coated by different materials [68, 148-152].

Finally, to validate the practical applicability of the MPP-Zn electrode, we fabricated full cells by coupling it with $NH_4V_4O_{10}$ cathodes (denoted as MPP-Zn//$NH_4V_4O_{10}$), as illustrated in Figure 3.25a, establishing a complete battery system to evaluate its practical performance metrics. MMP-Zn//$NH_4V_4O_{10}$ exhibited a higher initial capacity of 368 mAh g^{-1} than the 270 mAh g^{-1} for bare Zn//$NH_4V_4O_{10}$ at a high current density of 1 A g^{-1}. Electrochemical impedance spectroscopy (EIS) measurements reveal significantly reduced charge transfer resistance (R_{ct}) in the full cell employing the MPP-Zn electrode (Figure 3.25b), which directly correlates with its enhanced electrochemical activity and minimized polarization - providing mechanistic insights into the superior performance of this optimized battery system[153]. The enhanced zinc deposition/dissolution kinetics at the anode side likely contribute to the superior discharge capacity observed in the MPP-Zn//$NH_4V_4O_{10}$ full cell (Figure 3.25c), demonstrating the critical role of optimized interfacial charge transfer processes in achieving high-performance zinc-ion battery systems[134].

To systematically evaluate the rate capability, the full cell was subjected to stepwise current density cycling from 0.1 to 2 A g^{-1} (Figure 3.25d). The MPP-Zn//$NH_4V_4O_{10}$ full cell demonstrates superior performance compared to its bare Zn-based counterpart throughout the entire testing protocol. Notably, at the high current density of 2 A g^{-1}, the MPP-Zn

configuration delivers approximately 1.5 times higher reversible capacity than the unmodified Zn//$NH_4V_4O_{10}$ system. This superior rate performance can be attributed to the enhanced reaction kinetics and reduced charge transfer resistance (R_{ct}) at the MPP-Zn anode, demonstrating the critical role of optimized interfacial properties in achieving high-rate battery operation. To further elucidate the cycling advantages of the MPP-Zn system, we conducted long-term evaluation of the MPP-Zn//$NH_4V_4O_{10}$ full cell at 195 mA g^{-1}. Remarkably, the system maintained stable capacity retention over 300 cycles without observable voltage profile degradation (Figure 3.26a), demonstrating exceptional electrochemical stability enabled by the engineered interface. In stark contrast, the bare Zn//NH4V4O10 full cell exhibited a substantial 15% capacity loss after 300 cycles (Figure 3.26b) - more than double the degradation observed in its MPP-Zn counterpart (6% capacity loss relative to the activated maximum capacity shown in Figure 3.26c). The excellent stability of MMP-Zn//$NH_4V_4O_{10}$ cells embodied its advantage in suppressing dendrites and side-reactions in the case of full cells applications.

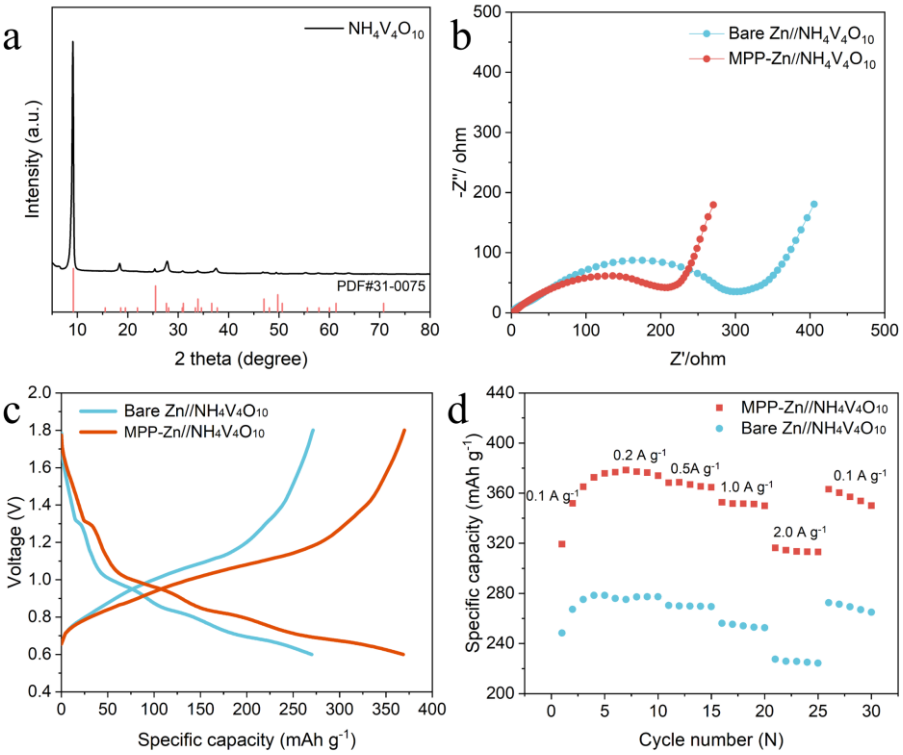

Figure 3.25 (a) XRD patterns of the $NH_4V_4O_{10}$ cathode material. (b) initial Nyquist plot of bare Zn//$NH_4V_4O_{10}$ and MPP-Zn//$NH_4V_4O_{10}$ full cell. (c) Voltage profiles of bare

Zn//$NH_4V_4O_{10}$ and MPP-Zn//$NH_4V_4O_{10}$ full cells. (d) Cyclic rate capacities of bare Zn//$NH_4V_4O_{10}$ and MPP-Zn//$NH_4V_4O_{10}$ full cells.

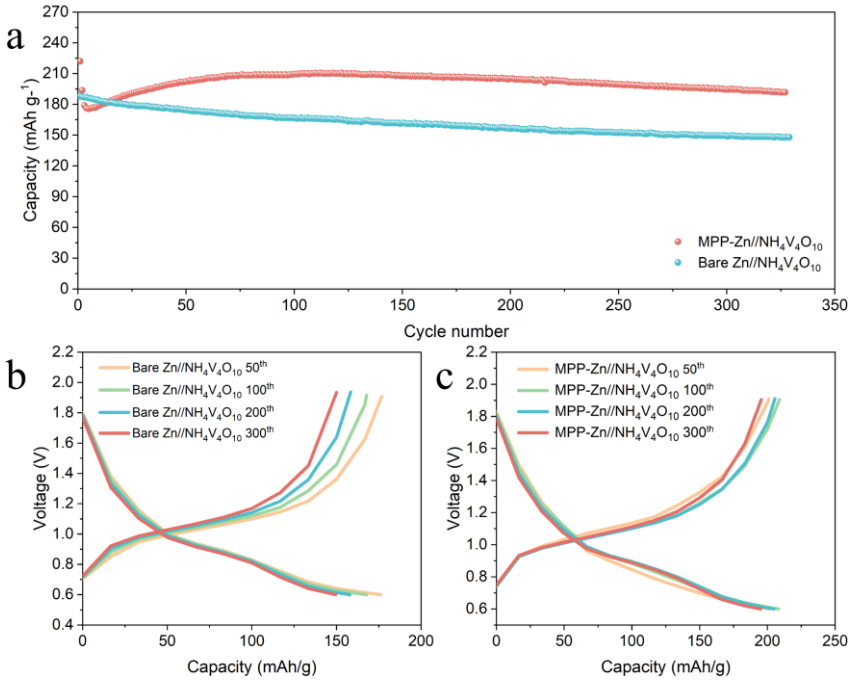

Figure 3.26 (a) cyclic capacities of MPP-Zn//$NH_4V_4O_{10}$ and bare Zn//$NH_4V_4O_{10}$ full cells at 1 A g^{-1}, (b) Galvanostatic charge/discharge curves of bare Zn// $NH_4V_4O_{10}$ full cells at a current density of 1 A g^{-1}. (c) galvanostatic charge/discharge profiles for MPP-Zn//$NH_4V_4O_{10}$ full cells at 1 A g^{-1} for 300 cycles.

3.3 Conclusion

In summary, this work successfully constructs a multifunctional integrated interface layer composed of MPP on zinc anode surfaces. The MPP layer, featuring abundant functional groups and a porous architecture, demonstrates strong binding energy with coordinated water molecules, thereby enabling three synergistic effects: (i) chemical trapping of zinc ions, (ii) homogeneous redistribution, and (iii) optimized desolvation. This comprehensive protection mechanism effectively shields the vulnerable zinc metal anode from water molecule attacks, thereby significantly suppressing parasitic reactions. Furthermore, the MPP interlayer serves dual functions: (i) passivating the electrode-electrolyte interface and (ii) homogenizing electric field distribution - synergistically enabling dendrite-free zinc deposition through precisely

regulated ion flux. The MPP-coated zinc metal electrodes demonstrate exceptional electrochemical performance in both symmetric/asymmetric cells and MPP-Zn//$NH_4V_4O_{10}$ full-cell configurations, rivaling state-of-the-art values reported in the literature. This study establishes an integrated design concept for artificial interphases on zinc metal anodes, offering a strategic blueprint that will significantly advance the development of viable metal anodes for future multivalent battery systems.

Chapter 4 Sabatier Principle Inspired Bifunctional Alloy for Pre-stripping Zinc Anodes

4.1 Introduction

The central challenge in achieving stable cycling of zinc-based batteries lies in the structural integrity and homogeneity of the zinc anode interface. In Chapter 3 of this thesis, we developed a MPP interfacial layer, which effectively realized the homogenization of electric field distribution and optimized regulation of ion concentration gradients on the zinc electrode surface, thereby establishing a stable zinc anode system with dendrite-suppressing capabilities. However, current research frameworks have predominantly focused on kinetic optimization of zinc deposition processes, while systematic investigations into the dynamic interfacial evolution mechanisms during the stripping process and their impact mechanisms on anode cycling stability remain underexplored. This research gap constitutes a critical scientific challenge impeding the advancement of highly reversible zinc anodes. Zn metal anode faces challenges of dendritic deposition, surface passivation and hydrogen evolution in aqueous electrolytes, leading to short cycle life and low Coulombic efficiencies (CEs), particularly at high depth of discharge (DOD)[154]. Most available cathode materials for AZRBs are Zn-free, such as MnO_2, VO_2 and O_2, necessitating the initial stripping of Zn anodes during cycling. This protocol, which mirrors the practical working scenario of AZRBs, is likely to exacerbate the failure of Zn metal anodes[155].

To achieve stabile and dendrite-free Zn metal anodes, various strategies have been proposed, including the electrolyte optimization[156], artificial coatings[157], and functional separators[158][13]. Among these, artificial coatings are considered particularly effective in homogenizing Zn^{2+} flux, suppressing hydrogen evolution reaction, and stabilizing Zn deposition by regulating the electrolyte/electrode interface. Despite these improvements, the

Zn utilization rates, or DODs remain extremely low (*i.e.,* <1% for 100 μm Zn foil), which are not conductive for practical applications. Metallic layers like In-Zn alloy[159] and Bi[160] with high mechanical strength were proposed to stabilize Zn anodes under competitive DODs (i.e., 45%). These artificial layers can gradually decompose and detach in electrolytes during cycling due to the volume fluctuations and the weak interactions with Zn metal, thus failing to provide long-term protection[161]. Transition metal (TM) layers with strong chemical interactions with Zn have also been reported to accommodate the large volume charges of Zn anodes during cycling[162]. Nevertheless, the selection criteria and mechanisms of the heterogeneous interfaces remain unclear, leading to a trial-and-error approach in identifying suitable TM coatings. The affinity (or zincophilicity) between the TM interface and Zn is crucial in determining the initial nucleation and subsequent growth of Zn metal. Conventionally, it is believed that stronger TM-Zn affinity implies lower Zn nucleation energy barriers and facilitated uniform deposition by forming stable TM-Zn interface[160, 163-165]. Inspired by the Sabatier principle, which advocates a 'just right' interaction between catalyst and reactant for effective catalytic reactions[166], it is worth exploring whether similar design principles apply for TM interface selection for robust Zn anodes.

In addition, dendritic Zn deposition has been widely attributed to the inhomogeneous electric field distribution and nonuniform Zn^{2+} ion concentration during the plating process[167, 168]. Similar to Li metal anodes[169], pre-stripping of the Zn metal electrode can induce inhomogeneous plating and dendrite formation during prolonged cycling in Zn//Zn symmetric cells[170]. Few attentions have been paid to the mechanisms of pre-stripping of Zn metal to accelerate the cell failure. While a pre-deposition protocol was proposed to enhance the stability of bare Zn anodes[170], it is considered infeasible for practical AZRBs using Zn-free cathodes. Therefore, new strategies or concepts to stabilize high DOD Zn metal anodes in conjunction with Zn-free cathodes for practical AZRBs are highly wanted.

In this work, we established a like Sabatier principle for screening optimal TM interface for high DOD cycling Zn anodes. We find that Cu demonstrates the highest stability among various TM materials (*i.e.,* Au, Ag, Ti, Sn, Al) due to the suitable Zn-Cu atomic interactions, which parallels the empirical Sabatier principle for TM catalysts. Atomic-scale observations show a gradual phase transition from Cu towards $CuZn_5$ during cycling, which facilitates the diffusion of Zn^{2+} ions and decrease Zn nucleation overpotentials. The Cu nanolayer indicates a bifunctional nature that serves as a buffer for homogeneous Zn metal dissolution during discharging and as a secondary current collector for dendrite-free Zn deposition during charging. Such a bifunctional interface ensures uniform Zn metal stripping and plating processes. As a result, Cu@Zn electrodes present remarkable cyclability (8000 h at 1 mA cm^{-2} in symmetric cells with an accumulative capacity of 8 Ah cm^{-2}), excellent reversibility (average CE of 99.4% over 1400 cycles in asymmetric cells), and outstanding stability at high DOD (250 h at a DOD of 80%). Applications of the optimal Zn electrodes are demonstrated in Cu@Zn||VO_2 full cells that can display an extremely low-capacity fading rate of 0.011 % per cycle over 1000 cycles, paving a promising way for developing practical AZRBs.

4.2 Results and Discussion

4.2.1 Initial plating and stripping of Zn metal anodes

In practical AZRBs, Zn metal anodes always undergo stripping reaction in accompany with Zn^{2+} ion insertion into Zn-free cathode materials. During the following charging process, the pre-stripped anode acts as a current collector for Zn deposition. The morphologies of initially stripped and plated Zn electrodes thus play a vital role in determining the stability of AZRBs. For bare Zn anodes, significant etching pits appear on the surface after initial stripping to 5 mAh cm^{-2} (Figure 4.1a and b) due to the nonuniform dissolution of Zn metal. During the following plating process, the formation and growth of dendritic-Zn clusters will be aggregated around the pre-stripped pits (Figure 4.1c and d). Over successive cycles, the uneven surface of

pre-stripped Zn exacerbates the dendritic Zn deposition and leads to porous Zn anodes (Figure 4.2a), which is detrimental to CEs and battery safety. To accommodate the uneven dissolution and deposition of Zn metal anodes, we proposed a bifunctional TM nanolayer ($\approx$100 nm) on the surface of Zn anode by a magnetic sputtering method. The working mechanisms of TM-coated Zn anodes are schematically illustrated in Figure 4.2b. The mechanically robust TM layer can stabilize Zn metal dissolution during discharging and regulate uniform Zn metal deposition in the following charging process. Thus, the TM layer serves as both a surface protector and a secondary current collector for dendrite-free Zn metal anodes.

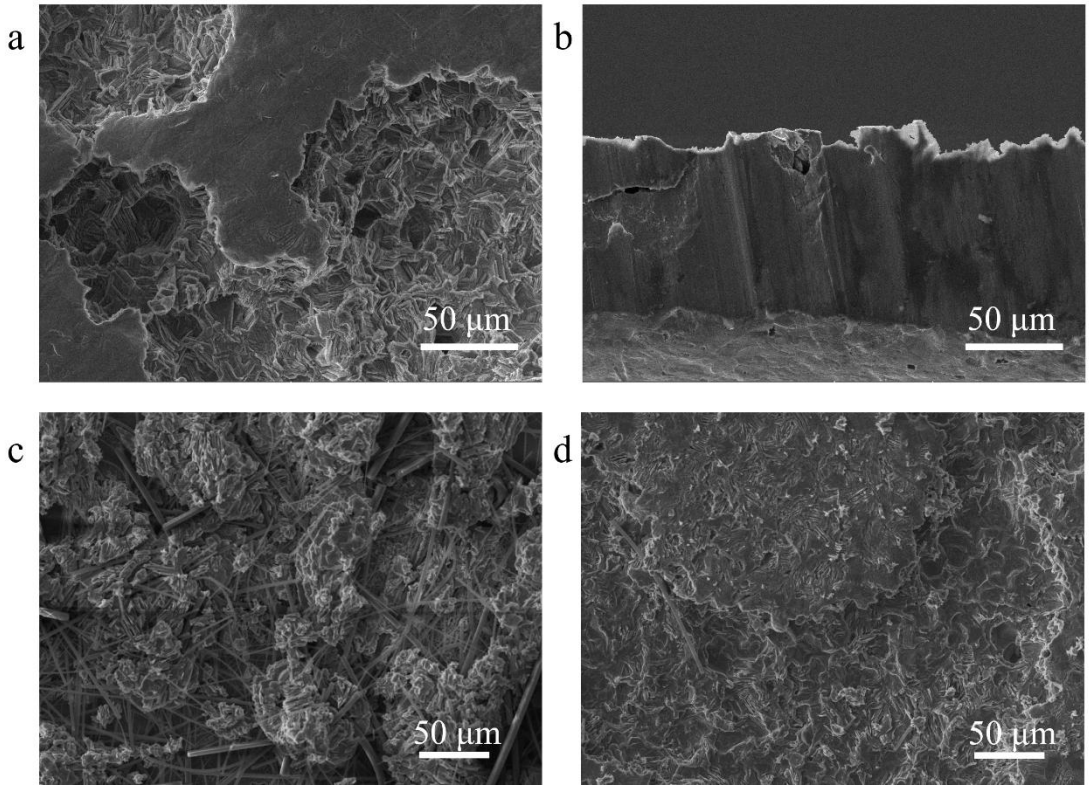

Figure 4.1 (a) Top view and (b) side view SEM images of stripped bare Zn by a capacity of 1 mAh cm^{-2} at 5 mA cm^{-2}. SEM images of the (c) pre-stripped Zn and (d) pre-plated Zn electrodes being plated by a capacity of 10 mAh cm^{-2} at 5 mA cm^{-2}. The electrodes were assembled in Zn//pre-treated Zn cells for electrochemical tests.

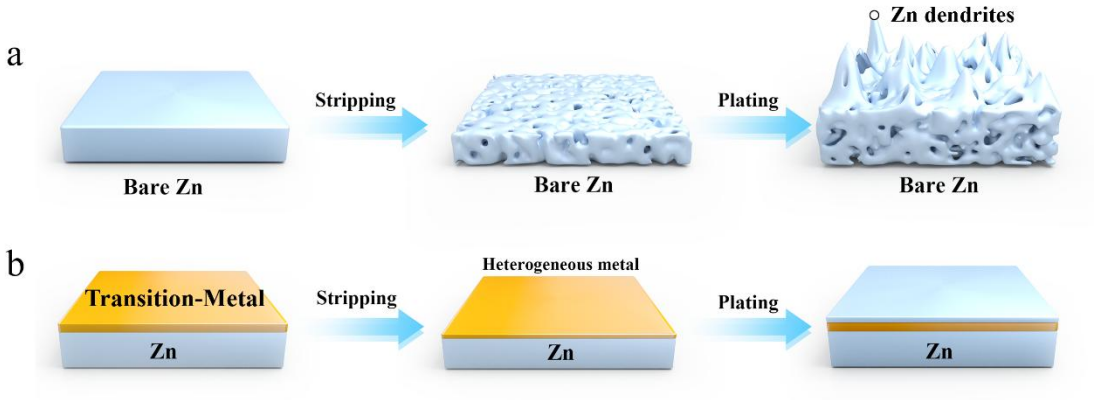

Figure 4.2 Schematic illustrating the morphological differences between discharged and charged Zn anodes in the full cell with (a) bare Zn anode and (b) TM@Zn anode.

To demonstrate the necessity and effectiveness of our bifunctional TM layer, we deposited a series of TM nanolayers (100 nm) including titanium (Ti), aluminum (Al), copper (Cu), silver (Ag), and gold (Au) metals on the surface of Zn anodes for electrochemical tests, in comparison to the bare Zn anode. Figure 4.3 shows the surface morphologies of bare Zn and TM@Zn electrodes after stripping for 5 mAh cm^{-2}. Different from the pit-rich surface of bare Zn, all TM@Zn electrodes display smooth surface, indicating the protective effect of TM layers in homogenizing the Zn metal dissolution process. A close examination of the surface topographies revealed stripping traces on Au@Zn and Ti@Zn surfaces, whereas the Ag@Zn and Cu@Zn surfaces remain flat and dense. This difference indicates the importance for TM interlayer selection for stabilizing Zn anodes, especially during pre-stripping process.

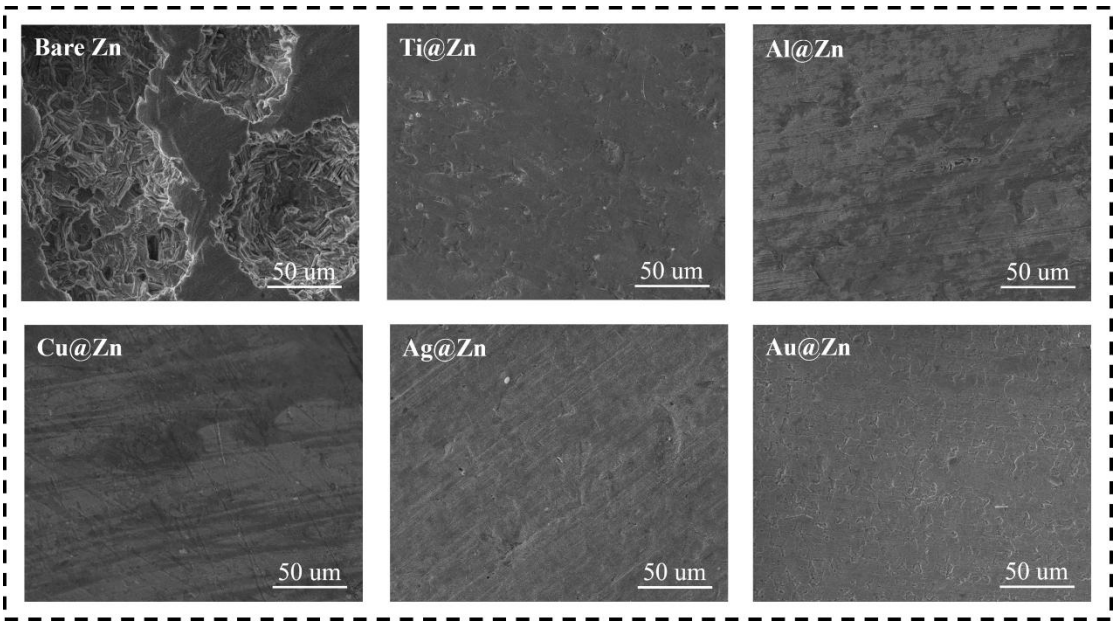

Figure 4.3 SEM images of bare Zn and TM@Zn electrodes after stripping at 5 mA cm^{-2} for a capacity of 5 mAh cm^{-2}.

4.2.2 Like Sabatier principle for selecting TM coating layers on stable Zn metal anodes

To identify the most suitable TM nanolayer for stable Zn anodes, we drew inspiration from the Sabatier principle (Figure 4.4a), which suggests the importance of ideal interactions between catalyst and reactant for effective catalytic reactions[171]. Analogically, the zincophilicity between TM and Zn atoms is essential in regulating the initial nucleation and subsequent growth of Zn metal. It is widely recognized that a strong Zn-TM bonding capacity can lower the nucleation barrier, promote initial nucleation, and benefit the uniform Zn deposition. Inspired by the Sabatier principle, we explored whether a capstone also applies for TM interfaces that can maximize the electrochemical performance of Zn anodes in aqueous electrolytes.

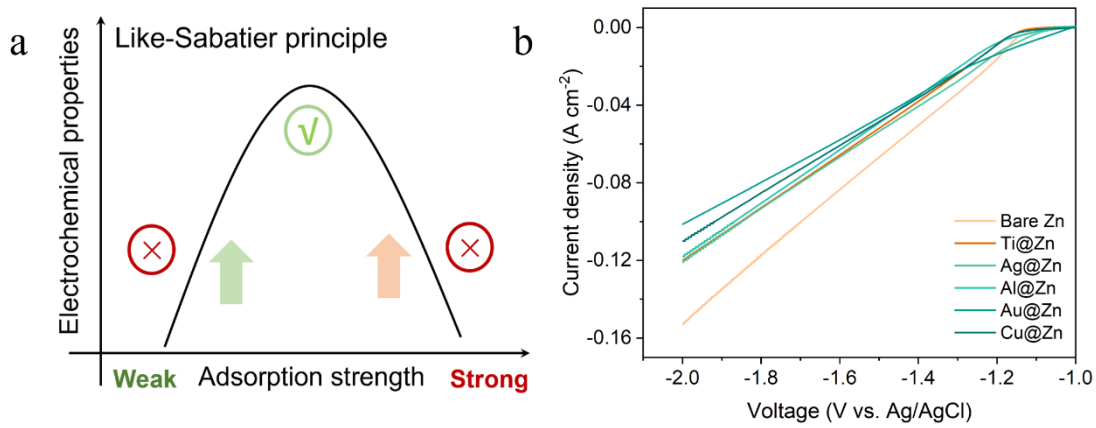

Figure 4.4 (a) Volcano plot of the like-Sabatier Principle. (b) Linear polarization curves for the corrosion of bare Zn and TM@Zn (TM= Ti, Ag, Al, Au, and Cu).

We firstly conducted liner sweep voltammetry (LSV) characterizations of TM@Zn and bare Zn anodes. As shown in Figure 4.4b, bare Zn exhibits the highest hydrogen reaction current density. In contrast, Cu@Zn and Au@Zn exhibit a lower reaction current density, suggesting the superiority of the Cu and Au coating layers in suppressing hydrogen evolution reaction (HER)[172]. Figure 4.5 also shows the lowest corrosion current densities for Cu@Zn and Au@Zn electrodes among bare Zn and TM@Zn electrodes. Density functional theory (DFT) calculations were employed to identify the zincophilicities of TMs. Figure 4.6a shows the binding energies (E_a) of Zn atoms with different TMs. The results indicate E_a values following the qualitative order of Ti@Zn, Au@Zn > Cu@Zn, Ag@Zn > Al@Zn. During the initial Zn plating at 1 mA cm^{-2}, Figure 4.6b shows increasing overpotentials of 30.3 mV for Ti@Zn, 33.5 mV for Au@Zn, 36.3 mV for Cu@Zn, 38.8 mV for Ag@Zn, and 42.3 mV for Al@Zn. Generally, lower nucleation overpotential indicates greater zincophilicity. Although Ti and Au indicate the highest zincophilicity and lowest overpotential, their stripping surfaces are rough, implying the ineffectiveness of selecting TM layer based solely on strong zincophilicity. The coulombic efficiency values of Zn plating/stripping on the TM@Zn electrodes were also measured in TM@Zn//Ti asymmetric cells[173]. Figure 4.6c shows that the Cu@Zn electrodes can be stably cycled over 1400 cycles with an average CE of 99.44%. In contrast, the bare Zn,

Al@Zn, Ti@Zn, Ag@Zn and Au@Zn electrodes exhibited much inferior cycle life of 60, 46, 52, 571 and 225 cycles, respectively. Our analysis of the average CE values of TM@Zn electrodes reveals a volcano-like distribution correlated with zincophilicity of TM layers (Figure 4.6d). This distribution is reminiscent of the Sabatier principle, which posits that optimal performance can be achieved when the catalyst-reactant interactions are 'just right'. This analogy suggests that a moderate interaction between TM and Zn is critical in regulating the electrochemical performance of Zn anodes.

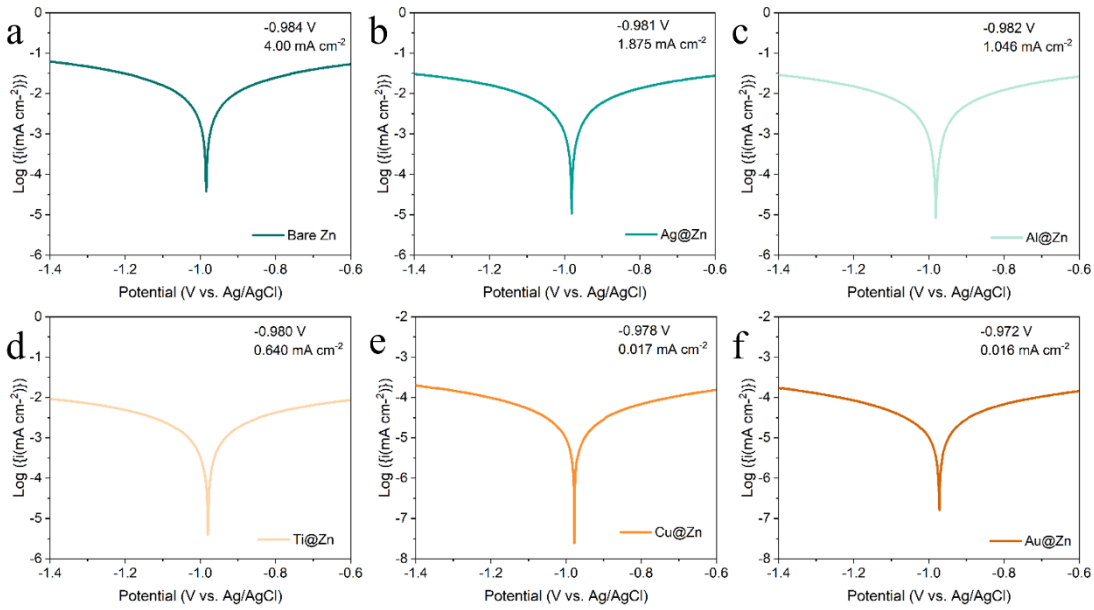

Figure 4.5 Tafel polarization curves of (a) bare Zn and (b-f) TM@Zn anode (Corrosion potential shows a positive shift from -0.984 V to -0.972 V and the corrosion current density decreased from 4.00 mA cm^{-2} to 0.016 mA cm^{-2}).

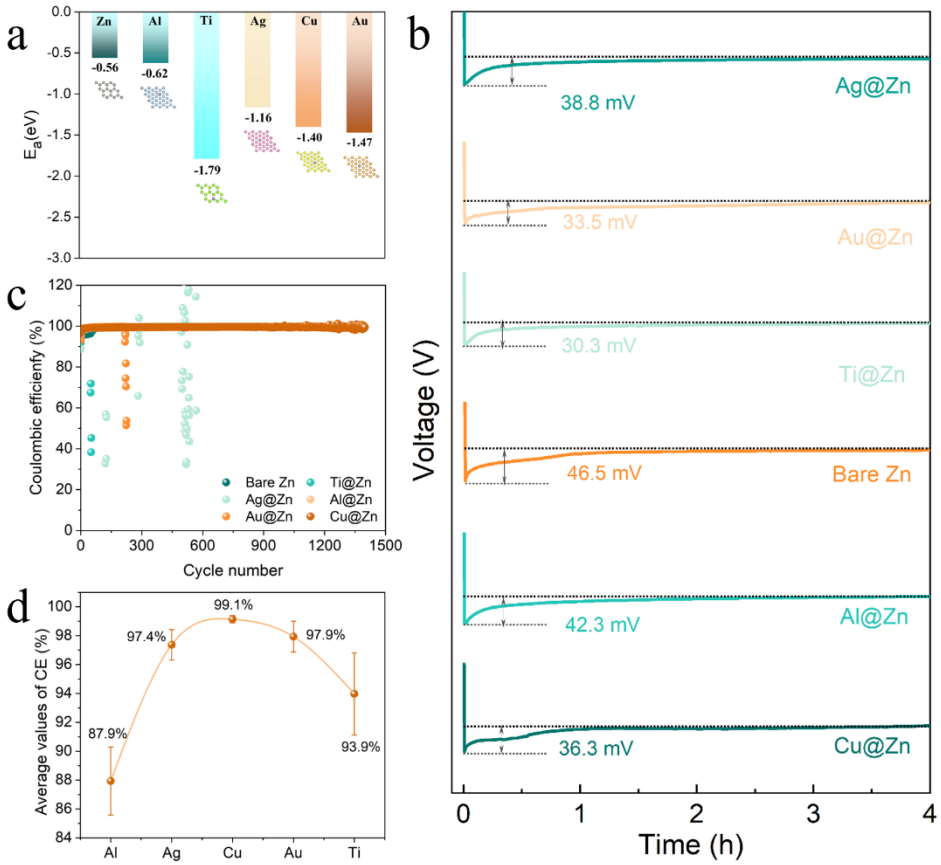

Figure 4.6 (a) E_a and adsorption configurations of Zn atoms on TM layers. (b) Polarization curves of Zn deposition at 1 mA cm^{-2} for 4 hours. (c) CEs of bare Zn, TM@Zn electrodes in asymmetric cells at 1 mA cm^{-2} and 1 mAh cm^{-2}. (d) average initial CE values for TM@Zn electrodes, the TM-Zn binding energy increases from left (Al-Zn) to the right (Ti-Zn).

Accordingly, we examined the morphologies of cycled TM@Zn electrodes with different zincophilicities (or TM-Zn binding strength), specifically strong (Au@Zn), moderate (Cu@Zn), and weak (Al@Zn) (Figure 4.6a). Figure 4.7 presents the FIB-SEM images of these electrodes after 10 cycles at 1 mA cm^{-2} and 1 mAh cm^{-2}. It shows that Al, with its weak binding strength to Zn, detached significantly and failed to protect Zn metal from in-depth etching during cycling. Despite Au's stronger interaction to Zn, the cross-sectional SEM image for Au@Zn exhibits significant structural damage and porous deposits, which can trigger the 'tip effect' and dendritic deposition during cycling, consistent with the fluctuating CEs in Figure 4.6c. In contrast, Cu@Zn with its moderate binding strength presents a dense interfacial morphology that enhances cyclic stability. We also imaged the separators facing TM interfaces

after plating/stripping cycles (Figure 4.8), which indicates significant amounts of Zn metal segments on the separators for Al@Zn, Au@Zn, and Ti@Zn electrodes. In contrast, no dead Zn is observed on the separators for Cu@Zn and Ag@Zn electrodes. Overall, these findings demonstrate the like-Sabatier principle in guiding the selection of TM interlayer for (electro)chemically stable Zn anodes in AZMBs.

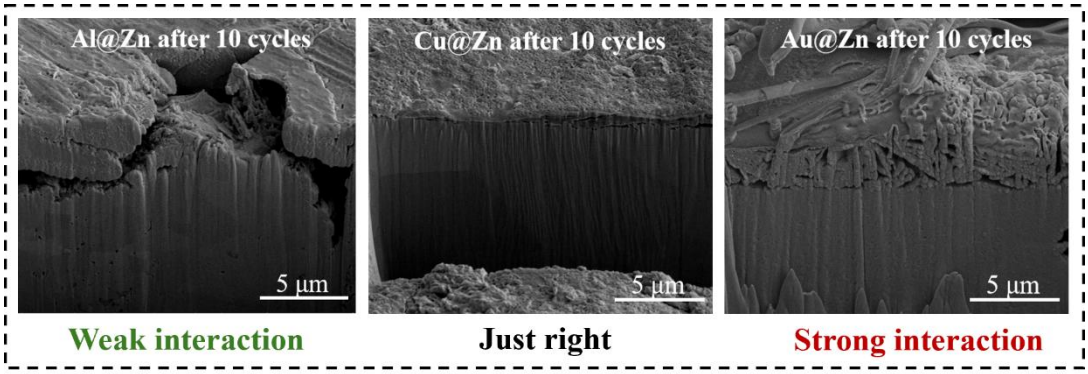

Figure 4.7 FIB-SEM images of Al@Zn, Cu@Zn, and Au@Zn electrodes after 10 cycles at 1 mA cm^{-2} and 1 mAh cm^{-2}.

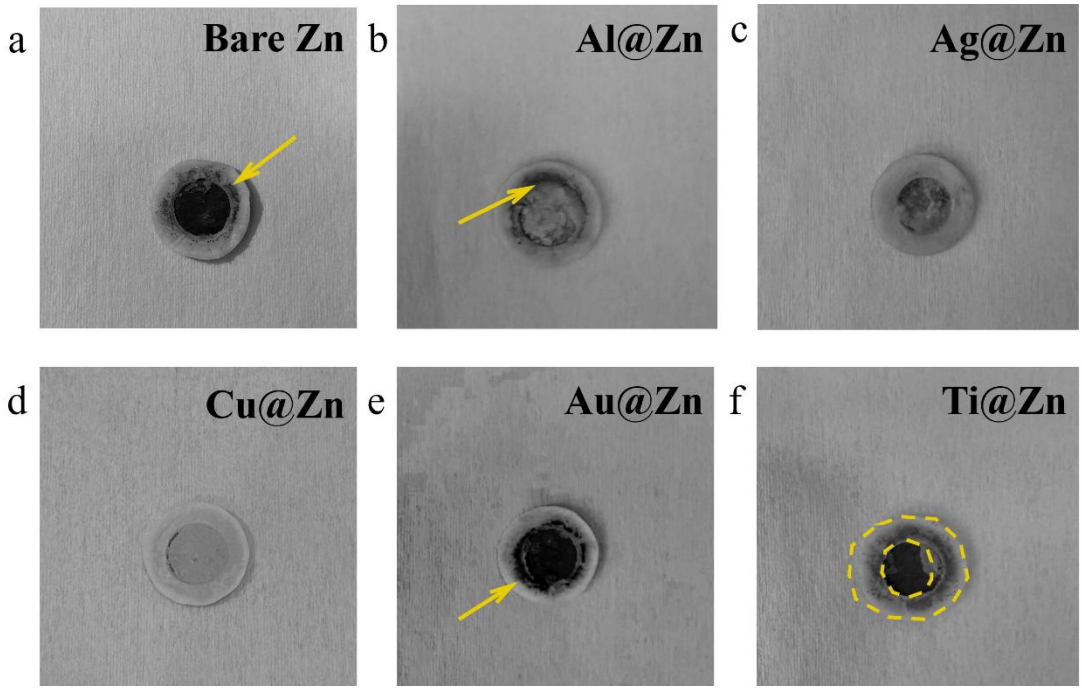

Figure 4.8 Optical images of the separators facing different TM@Zn electrodes after 50 cycles at 1 mA cm^{-2}, 1 mAh cm^{-2}. (a) bare Zn, (b) Al@Zn, (c) Ag@Zn, (d) Cu@Zn, (e) Au@Zn, (f) Ti@Zn, the arrows or dash circles in (a), (b) and (f) shows the detached Zn particles.

To further verify the effectiveness of this election criterion, we evaluated the electrochemical stability of TM@Zn electrodes. The symmetric cells (TM@Zn//TM@Zn) were cycled at a high current density of 5 mA cm^{-2} with a moderate capacity of 1 mAh cm^{-2}. As shown in Figure 4.9a, the Cu@Zn//Cu@Zn symmetric cells achieved an ultralong cycling life of over 2200 h and low overpotential (~20 mV), which is over 100 times longer than that of bare Zn. High rate cycling may alleviate the Zn anode corrosion in aqueous electrolyte[174], so we also cycled the Cu@Zn//Cu@Zn cells at a low current density of 1 mA cm^{-2} for 8000 h (Figure 4.9b), resulting in an accumulated capacity of 8 Ah cm^{-2} and demonstrating excellent stability and low overpotentials. This cycling performance is much superior to its peer Zn electrodes in terms of the accumulative capacity and cycle life (Table 4.1). In contrast, the Al@Zn, Au@Zn, Ag@Zn and Ti@Zn symmetric cells displayed cycle lives of below 350 hours at low current density of 1 mA cm^{-2} and less than 1000 hours at the high current density of 5 mA cm^{-2} with a capacity of 1 mAh cm^{-2}. The significantly different electrochemical performance was also evident at increasing rate from 0.5 mA cm^{-2} to 8 mA cm^{-2}. Figure 4.9c shows the lowest voltage hysteresis for Cu@Zn electrode in comparison with other TM@Zn and bare Zn electrodes, indicating the superior kinetics of Cu@Zn anodes[175].

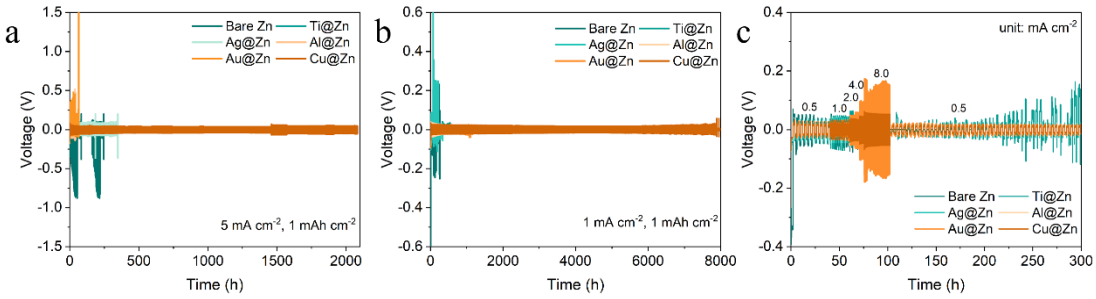

Figure 4.9 Long-term cycling of symmetrical cells at (a) 5 mA cm^{-2} with 1 mAh cm^{-2} and (b) 1 mA cm^{-2} with 1 mAh cm^{-2}. (c) Rate performances of the six kinds of symmetric cells at current densities from 0.5 to 8 mA cm^{-2} and a constant capacity of 1 mAh cm^{-2}.

Table 4.1 Comparison of the cyclic performance of Cu@Zn electrodes with peer electrode materials in the literature

Electrode	Test Conditions	Cycling life	Accumulated capacity	Ref.
$Zn_{0.73}Al_{0.27}$	1 mA cm^{-2}, 1 mAh cm^{-2}	3000 h	3 Ah cm^{-2}	[174]
ZnSe	2 mA cm^{-2}, 1 mAh cm^{-2}	1000 h	1 Ah cm^{-2}	[176]
Zn@PAQ	1 mA cm^{-2}, 1 mAh cm^{-2}	1650 h	1.65 Ah cm^{-2}	[177]
P(VDF-TrFE)@Zn	0.2 mA cm^{-2}, 0.2 mAh cm^{-2}	2000 h	0.4 Ah cm^{-2}	[178]
Zn@PDA	2 mA cm^{-2}, 1 mAh cm^{-2}	500 h	0.5 Ah cm^{-2}	[179]
P-Zn	0.5 mA cm^{-2}, 0.5 mAh cm^{-2}	2750 h	1.38 Ah cm^{-2}	[180]
ZnS@Zn	2 mA cm^{-2}, 2 mAh cm^{-2}	1000 h	2 Ah cm^{-2}	[181]
ZnF_2@Zn	1 mA cm^{-2}, 1 mAh cm^{-2}	800 h	0.8 Ah cm^{-2}	[182]
PPZ@Zn	1 mA cm^{-2}, 0.5 mAh cm^{-2}	3000 h	1.5 Ah cm^{-2}	[183]
HMTA@Zn	5 mA cm^{-2}, 5 mAh cm^{-2}	600 h	3 Ah cm^{-2}	[184]
HSOF@Zn	5 mA cm^{-2}, 1 mAh cm^{-2}	2700 h	2.7 Ah cm^{-2}	[185]
L-CN@Zn	1 mA cm^{-2},1 mAh cm^{-2}	6000h	6 Ah cm^{-2}	[186]
Cu@Zn	1 mA cm^{-2}, 1 mAh cm^{-2}	8000 h	8 Ah cm^{-2}	This work
	5 mA cm^{-2}, 1 mAh cm^{-2}	2200 h	2.2 Ah cm^{-2}	

To understand dramatic differences in electrochemical properties, we conducted SEM observations the stripped (Figure 4.10) and plated (Figure 4.11) TM@Zn electrodes. The bare Zn electrode showed irregular stripping voids (Figure 4.10a), consistent with our previous discussion. The Al@Zn electrode exhibited significant delamination of the Al layer from Zn substrate (Figure 4.10b), leaving large voids in the exposed areas, therefore the weak Al-Zn interaction is unfavorable for TM coating protection. The Au@Zn (Figure 4.10e) and Ti@Zn (Figure 4.10f) electrodes with very strong TM-Zn interactions suffered extensive structural damage on the stripped suffices. In contrast, the stripped Ag@Zn (Figure 4.10c) and Cu@Zn (Figure 4.10d) electrodes maintained relatively smooth and dense surfaces. For deposited samples, the Al@Zn presents numerous cracks and irregular deposition (Figure 4.11b). Due to the uneven surface after stripping, the surfaces of deposited bare Zn, Au@Zn and Ti@Zn electrodes present prominent Zn dendrites (Figure 4.11a, e and f). Conversely, the optimal Cu@Zn electrode maintained a smooth surface after deposition, benefiting from the uniform interface. These results highlight the importance of selecting a proper TM layer protecting Zn

during cycling. Consequently, Cu@Zn will be selected as the mode anode for the subsequent fundamental studies.

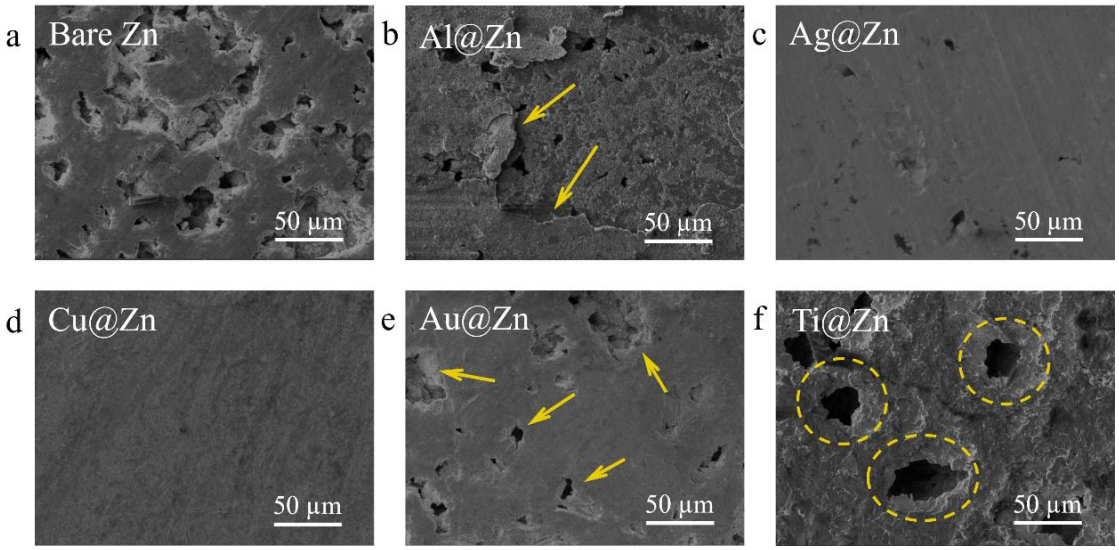

Figure 4.10 SEM images of stripped (a) bare Zn, (b) Al@Zn, (c) Ag@Zn, (d) Cu@Zn, (e) Au@Zn and (f) Ti@Zn electrodes at the 50th cycle at 1 mA cm^{-2}, 1 mAh cm^{-2}.

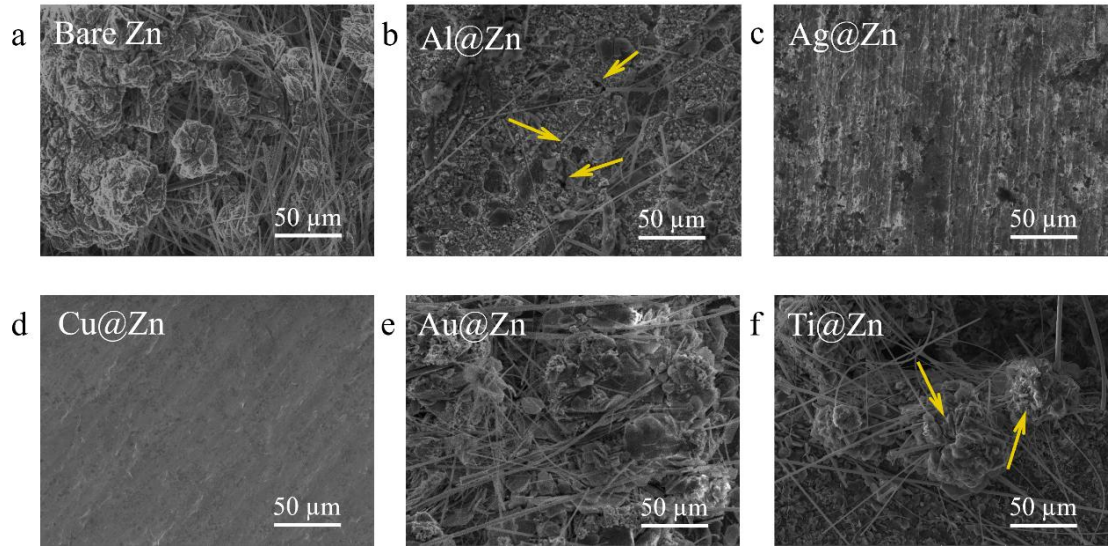

Figure 4.11 SEM images of deposited (a) bare Zn, (b) Al@Zn, (c) Ag@Zn, (d) Cu@Zn, (e) Au@Zn and (f) Ti@Zn electrodes at the 50th cycle at 1 mA cm^{-2}, 1 mAh cm^{-2}.

To illustrate the effectiveness of Cu nanolayer, we examined the morphological evolutions of bare Zn (Figure 4.12) and Cu@Zn (Figure 4.13) metal anodes after different stripping and plating capacities using scanning electron microscopy (SEM). The pristine Cu@Zn exhibits a smooth surface as that of bare Zn. After striping at 5 mA cm^{-2} for 1/5 hour (or 1 mAh cm^{-2}),

discernible pits of 10 μm in size were observed on the surface of bare Zn (Figure 4.12a$_1$), in sharp contrast to the intact surface of Cu@Zn (Figure 4.13a$_1$). When we increased the stripping capacities to 3 and 5 mAh cm^{-2} (Figure 4.12a$_2$ and 4.12a$_3$), more pits with irregular morphologies and etching depths appeared on the surface of bare Zn electrode, further verifying the uneven Zn dissolution during discharging. In contrast, Cu coating layer can effectively uniform the stripping process of Zn metal anode (Figure 4.13a$_1$-4.13a$_3$). Then, the 5 mAh cm^{-2}-stripped bare Zn and Cu@Zn electrodes were plated in new cells at 5 mA cm^{-2}. For bare Zn electrodes, the bumps grow into big dendrites accompanied by the persistence of striping pits (Figure 4.12a$_4$-a$_6$). Cu@Zn electrodes display flat surfaces and dense Zn deposits with increasing deposition capacities from 1 mAh cm^{-2} to 5 mAh cm^{-2} (Figure 4.13a$_4$-a$_6$).

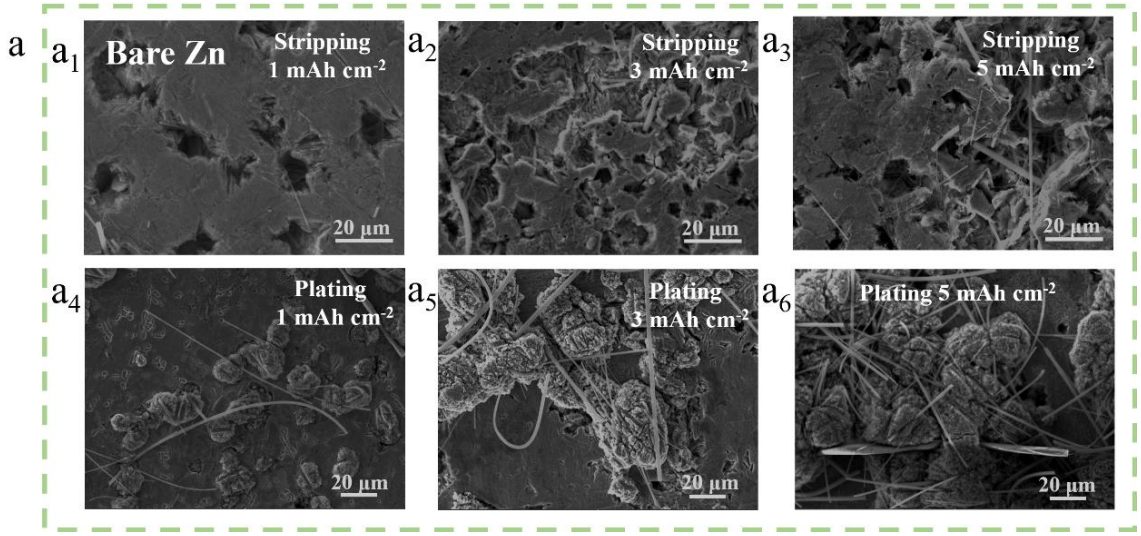

Figure 4.12 Morphological evolution of Zn stripping/plating processes. (a) SEM images of bare Zn electrodes after stripping by (a$_1$) 1 mAh cm^{-2}, (a$_2$) 3 mAh cm^{-2} and (a$_3$) 5 mAh cm^{-2} at 5 mA cm^{-2}. And then plated with (a$_4$-a$_6$) 1 mAh cm^{-2}, 3 mAh cm^{-2} and 5 mAh cm^{-2} at 5 mA cm^{-2}.

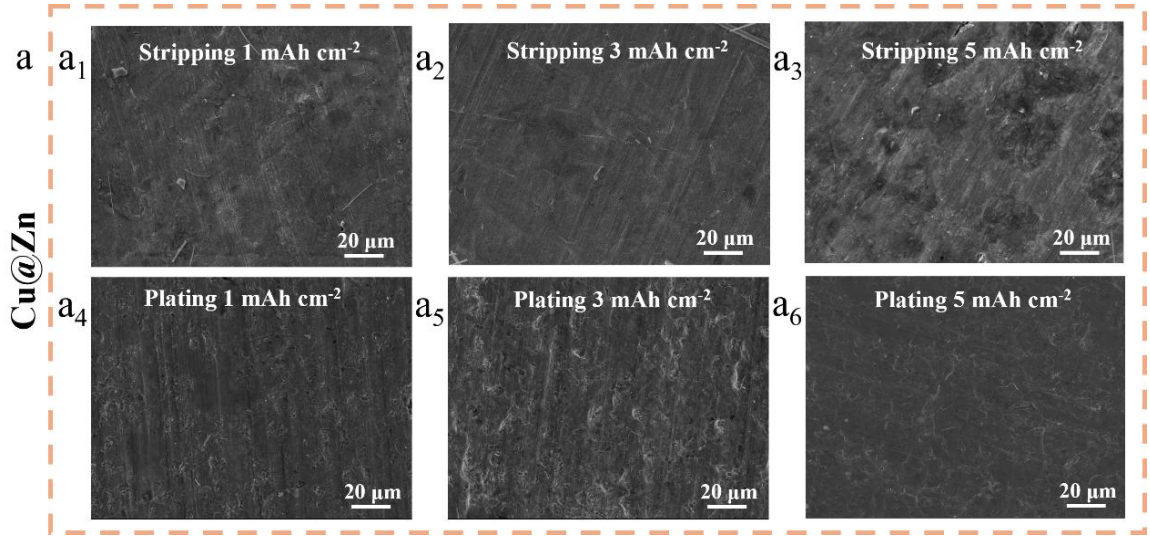

Figure 4.13 SEM images of Cu@Zn electrodes after stripping by (a_1) 1 mAh cm^{-2}, (a_2) 3 mAh cm^{-2} and (a_3) 5 mAh cm^{-2} at 5 mA cm^{-2} and then plating by (a_4-a_6) 1 mAh cm^{-2}, 3 mAh cm^{-2} and 5 mAh cm^{-2} at 5 mA cm^{-2}.

In-situ optical microscopy was also employed to observe the morphological evolution at the electrode/electrolyte interface during Zn metal stripping and plating for bare Zn and Cu@Zn electrodes. For bare Zn anodes, an uneven surface with fractures appears after stripping for 30 min at 2 mA cm^{-2}, which induced the aggressive dendrite growth in the following plating process (Figure 4.14), in agreement with our SEM observations (Figure 4.12 and Figure 4.13). In contrast, Cu@Zn electrodes maintained a uniform electrolyte/electrode interface without turbulence or inhomogeneous Zn deposits (Figure 4.14b) under the same measurement conditions.

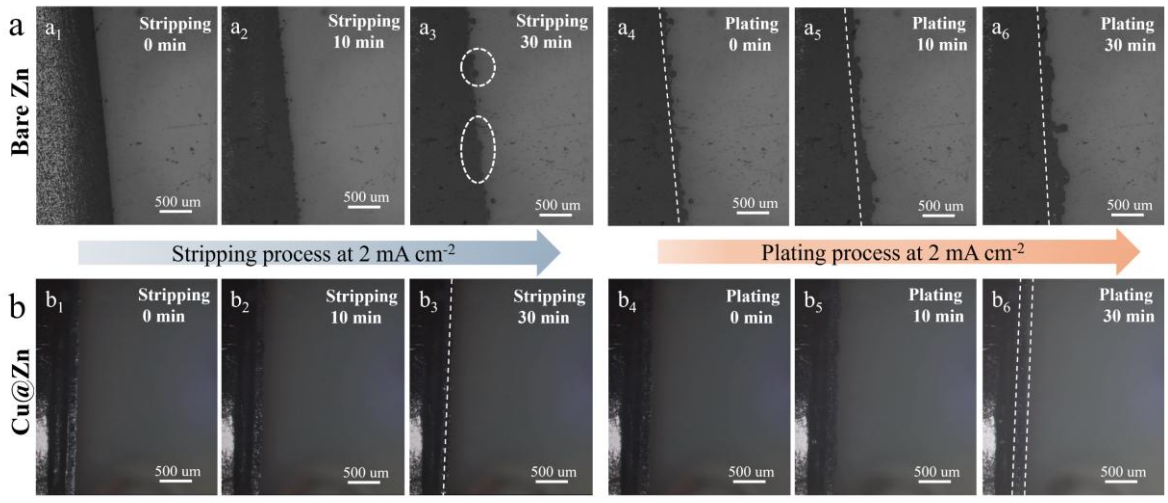

Figure 4.14 *In-situ* optical microscope images of Zn stripping/plating behaviors of a) bare Zn and b) Cu@Zn electrodes at a current density of 2 mA cm^{-2} for 30 min.

4.2.3 Working mechanisms of Cu interface to stabilize Zn anode

To elucidate the working mechanisms of Cu interface on stabilizing Zn anodes, we conducted comprehensive structural characterizations of Cu@Zn electrodes using X-ray photoelectronic spectroscopy (XPS), X-ray diffraction (XRD), FIB-SEM and scanning transmission electron microscopy (STEM). Pristine Cu@Zn indicates a uniform and phase-pure Cu layer as shown in TEM image (Figure 4.15) and in-depth XPS results (Figure 4.16a and b). After cycling in symmetric cells at 1 mA cm^{-2} for 50 cycles, the grazing incidence XRD patterns in Figure 4.17a showed characteristic peaks of Zn metal (JCPDS 04-0831) and $CuZn_5$ phase (JCPDS 35-1152), implying a Zn-Cu alloying process during cycling. High-resolution XPS was also employed to evaluate the chemical state of the cycled Cu@Zn electrode. Ar^+ sputtering in-depth XPS profiles in Figure 4.16c and d reveals strong Zn 2p peaks on the top surface with a weak Cu 2p signal, likely due to Zn deposition on the secondary current collector during cycling. At a depth of 200 nm, the Cu 2p and Zn 2p XPS spectra show similar intensities, indicating the formation of $CuZn_x$ alloys. At depths of 300 nm and 400 nm, the Zn 2p1/2 and Zn 2p3/2 peaks shift from 1045.5/1022.2 eV to 1044.9/1021.8 eV arising from the electronic structure changes of Zn atom in the alloying layer[187]. Uniform elemental distribution of this alloy layer is also confirmed by EDS mapping (Figure 4.17b).

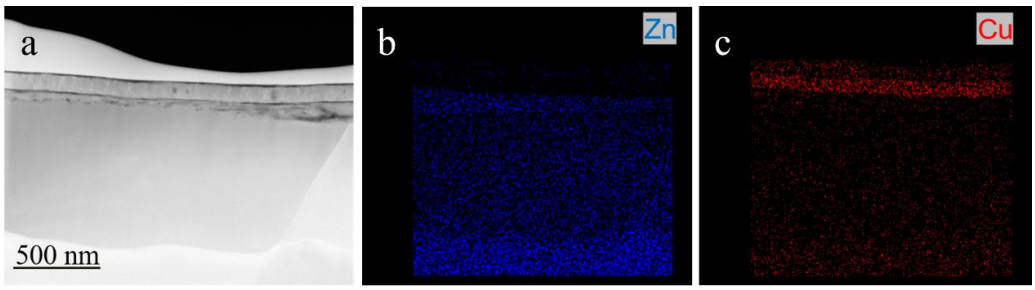

Figure 4.15 TEM image and EDS mapping of the pristine Cu@Zn electrode. FIB-cutting is applied to obtain the cross-section information of Cu@Zn sample.

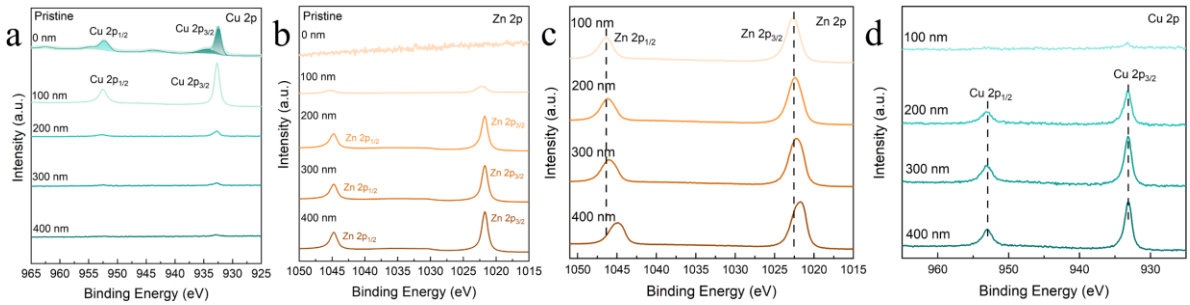

Figure 4.16 XPS curves of pristine Cu@Zn from the surface to 400 nm. (a) Cu 2p and (b) Zn 2p curves. XPS curves of Cu@Zn after 50 cycles. (c) Cu 2p and (d) Zn 2p.

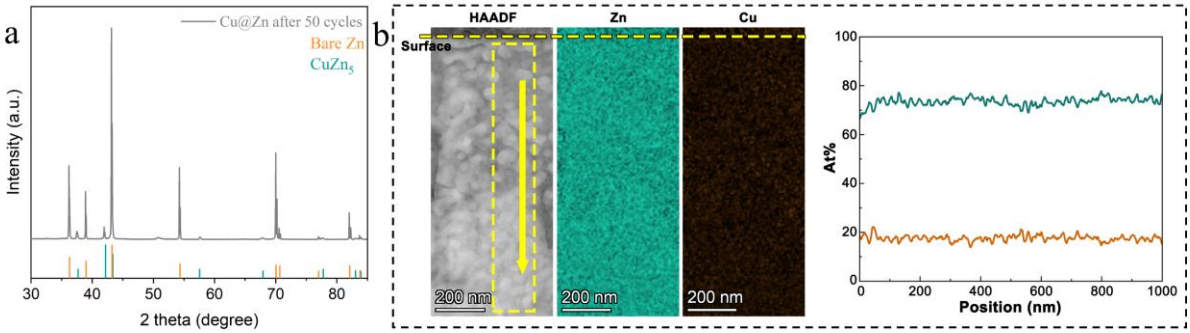

Figure 4.17 (a) XRD patterns of Cu@Zn electrode after 50 cycles with 1 mAh cm^{-2} at 1 mA cm^{-2}. The XRD peaks can be assigned to Zn and $CuZn_5$ phases. (b) EDS-mapping of Cu@Zn after 50 cycles at 1 mA cm^{-2}, 1 mAh cm^{-2}.

Phase evolution of the *in-situ* generated $CuZn_x$ alloys was elucidated by XRD and high-resolution STEM characterizations. XRD patterns show a unique peak at around 41.15° (d = 0.219 nm) referring to $CuZn_x$ phases for the cycled Cu@Zn electrodes (Figure 4.18). STEM images of Cu@Zn after 50 cycles (denoted as Cu@Zn-50) displayed nanograins (marked by orange dash lines) of around 100 nm within the Zn matrix (Figure 4.19b), which are smaller than these after 20 cycles (denoted as Cu@Zn-20, Figure 4.19a). Grain refinement of $CuZn_x$ alloys upon cycling was evidenced by the enhanced polycrystalline selected area diffraction (SAD) patterns for Cu@Zn-50 compared to Cu@Zn-20. Figure 4.19c shows the high-angle dark-field STEM (HAADF-STEM) and the corresponding fast Fourier transform (FFT) images of the transition phase in Cu@Zn-20 with the lattice distances consist with the XRD results. The HAADF images displayed an alternative ordered contrast change, where the typical area

marked by orange dash square was enlarged in Figure 4.19d$_1$ and the triangle area in Figure 4.19d$_2$.

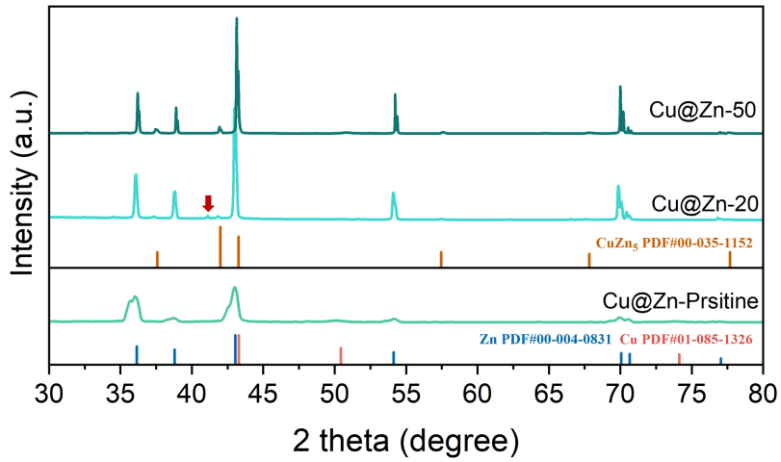

Figure 4.18 XRD patterns of Cu@Zn, Cu@Zn-20 and Cu@Zn-50 electrodes.

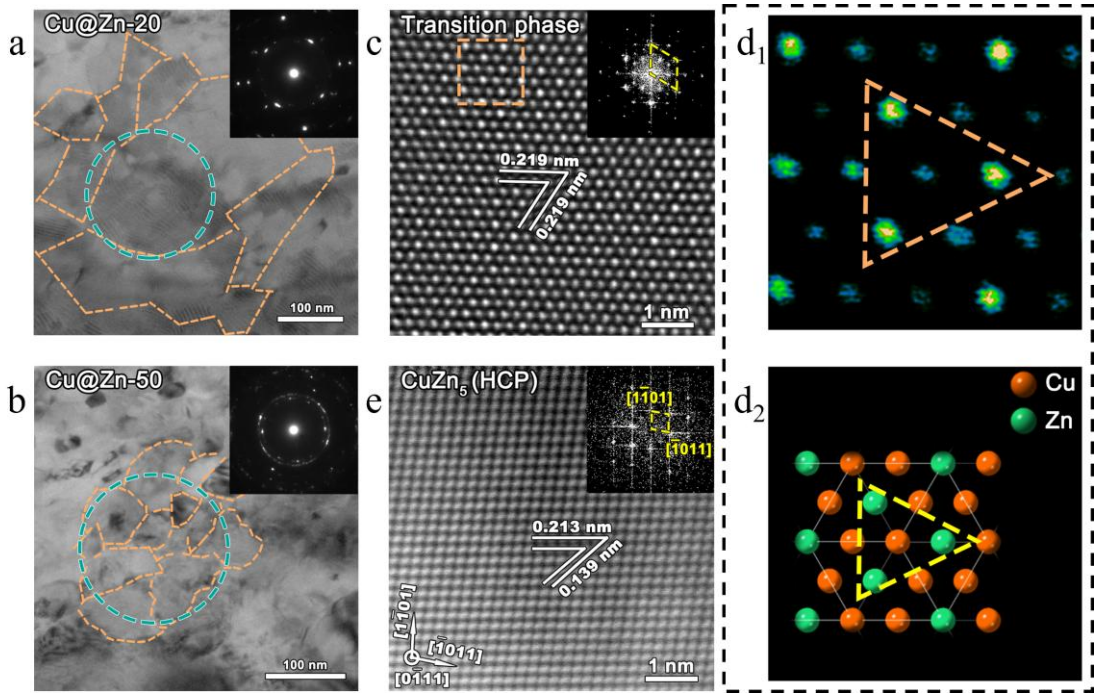

Figure 4.19 The BF-TEM images of (b) Cu@Zn-20 and (c) Cu@Zn-50. The corresponding SADF images are presented in the top-right corner. STEM-HAADF image of (d) transition phase $CuZn_x$ from Cu@Zn-20 sample and (f) $CuZn_5$ with the orientation from Cu@Zn-50. The corresponding FFT images and typical lattice distances are inserted. A detailed squared region marked by orange dash line in (d) are zoomed in and contrast moderated in (e$_1$) and (e$_2$) for the dash line triangles marked the pattern.

For the Cu@Zn-50 electrode, the lattice distances of 0.139 nm and 0.213 nm as marked for a typical hexagonal close-packed (HCP) $[01\bar{1}1]$ orientation (Figure 4.19e) for $CuZn_5$ phase. The

lattice parameters for the $CuZn_5$ crystal are significantly different from these of Zn substrate and Cu coating layer (Figure 4.20a and b). These results demonstrate the Cu-Zn alloying process as illustrated in Figure 4.20c-4.20e. Specifically, Cu atoms in face-centered cubic (FCC) structure are initially oxidized and receive Zn metal atoms to form a transition structure. With the continuous loss of Cu and insertion of Zn, the alloying phase will gradually convert to HCP $CuZn_5$ phase (Figure 4.20c)[188]. The microhardness of the in-situ generated $CuZn_x$ interface was also measured, which exhibited a gradual increase from 48 HV for the pristine Cu@Zn to 139 HV for the 50th cycled electrode (Figure 4.21). The enhanced hardness of $CuZn_x$ alloy interface is also beneficial for the structural integrity of Cu@Zn electrodes.

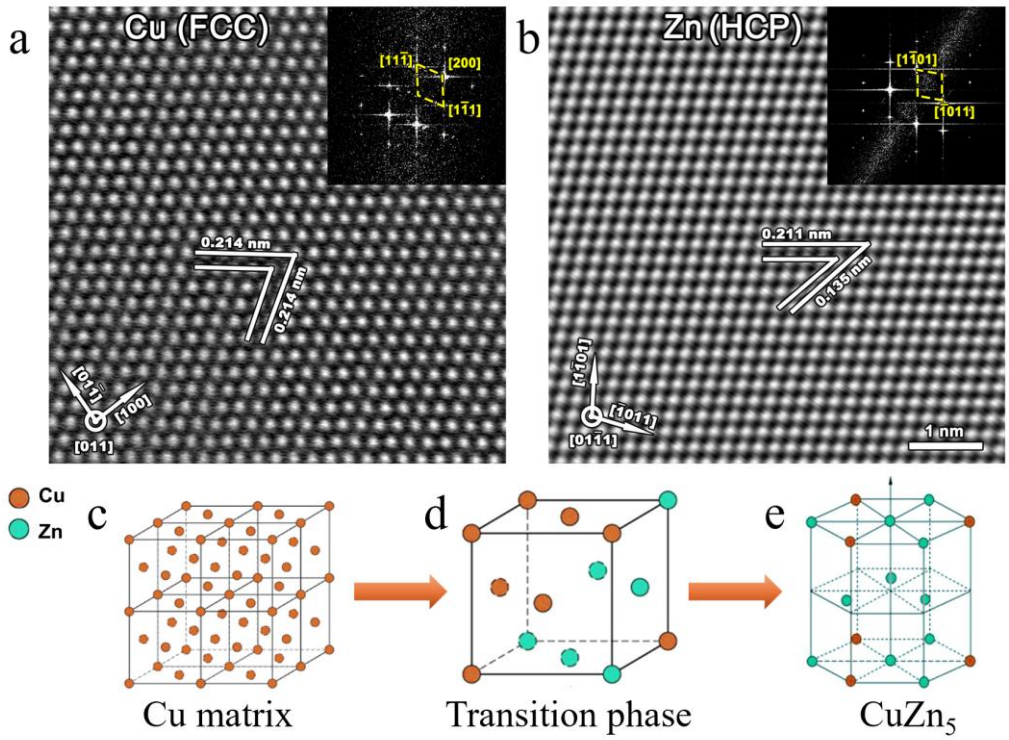

Figure 4.20 STEM-HAADF atomic images of (a) Cu lattice with the orientation of [011] and (b) Zn lattice with the orientation of [01$\bar{1}$1]. The corresponding FFT images with the typical pattern have been inserted. Typical lattice distances are also marked. The schematic diagram of (c) Cu matrix evolution via (d) $CuZn_x$ transition phase to (e) $CuZn_5$.

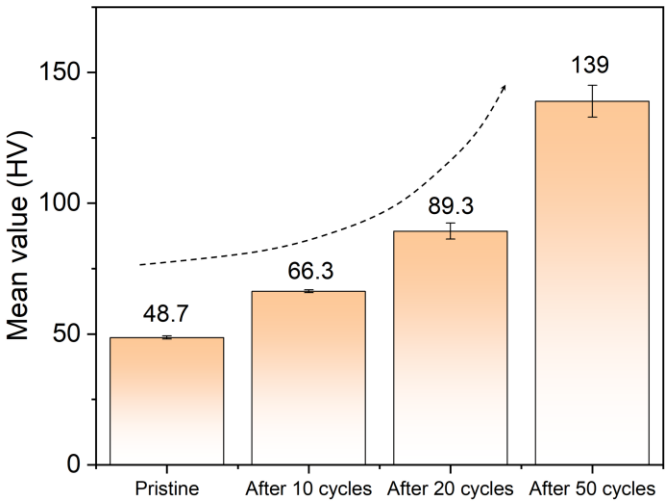

Figure 4.21 Microhardness of the Cu@Zn after different cycle numbers. (Vickers hardness tests were carried out under a 10 g load for 10 seconds using a Struers Duramin-40.)

The charge transfer kinetics of the dynamic interface was evaluated by electrochemical impedance spectroscopy (EIS) measurements.[189] Nyquist plots of the cycled Cu@Zn electrodes (Figure 4.22a) showed a single high-frequency semi-circle with lower-frequency tail, which can be fitted by an equivalent circuit comprising a charge transfer resistance (R_{ct}) element and a capacitance-Warburg impedance element for Zn^{2+} diffusion through the interphase layer. The diameters of the semi-circles decreased significantly after the 1st cycle and stabilized in the following five cycles, possibly due to the initial activation and gradual phase transition of the interface layers. The kinetics of Zn stripping and plating through the coating layer were parametrized by a formal exchange current, j_0. The value of j_0 can be extracted from the EIS results via $j_0 = RT/(zFSR_{ct})$, where R, T, z, F and S represents the universal gas constant, the absolute temperature, the valance state of Zn^{2+}, the Faraday constant and the surface area of the electrode, respectively[190]. The j_0 values for Cu@Zn increased from 0.042 to 0.123 mA cm^{-2} across the 20 cycles, about 8 times higher than these of bare Zn electrodes (Figure 4.22b). The lower charge transfer resistance and higher exchange current for cycled Cu@Zn electrodes indicate the favorable Zn^{2+} diffusion through the $ZnCu_x$ alloying layer. In contrast, j_0 of bare Zn electrodes initially increased due to the exposure of porous Zn deposits but decreased rapidly from the surface passivation and dendrite formation (Figure

4.22d). The superior interfacial charge transfer kinetics of cycled Cu@Zn electrode was also evidenced by the lower activation energy (E_a = 21.73 kJ mol^{-1}) than bare Zn (E_a = 33.26 kJ mol^{-1}) (Figure 4.23a to 4.23c)[177].

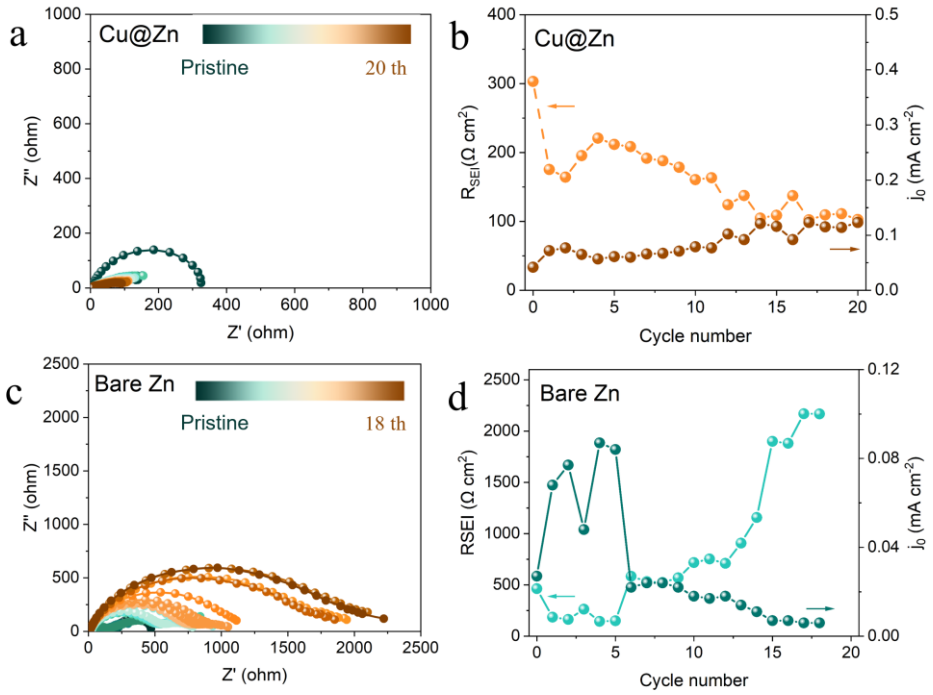

Figure 4.22 Nyquist plots of in-situ EIS measured (a) Cu@Zn and (c) bare Zn symmetric cells over 20 cycles. The R_{SEI} and exchange current density j_0 for (b) Cu@Zn and (d) bare Zn electrodes derived from (a, c).

Next, we examined the role of secondary current collector for the coating layer on Cu@Zn anodes. Chronoamperometry (CA) analysis at a constant overpotential of -150 mV reflected the nucleation process and surface changes[68]. For the bare Zn, the current density continues to increase above 400 s (Figure 4.23d), indicating the rampant 2D diffusion of Zn^{2+} ions and uncontrollable dendritic Zn growth. In specific, the Zn^{2+} ions tend to diffuse laterally for minimizing the surface energy and the exposed area, thus aggregating Zn deposits into dendrites. In contrast, the Cu@Zn undergoes a longstanding 3D diffusion process with a current density of 15 mA cm^{-2} after 30 s of planar diffusion and nucleation. Zn^{2+} ions on the $ZnCu_x$ surface are reduced to metallic Zn locally with constrained 2D surface diffusion. The

highly conductive $ZnCu_x$ layer serves as the favorable secondary current collector for uniform Zn nucleation with low surface energy.

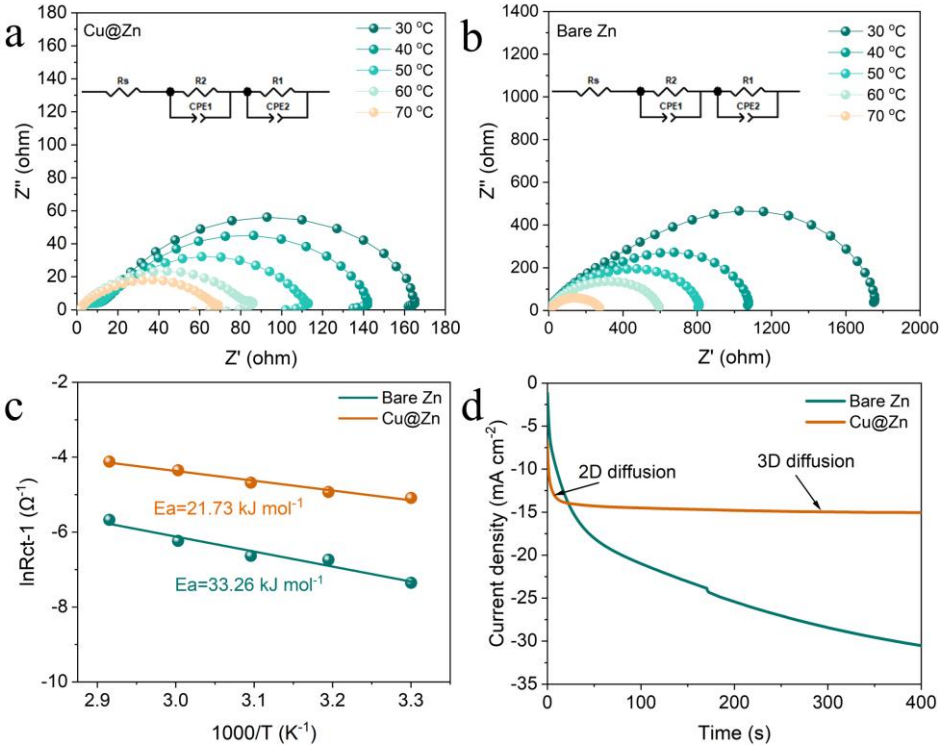

Figure 4.23 Nyquist EIS plots of (a) bare Zn and (b) Cu@Zn electrodes at different temperatures. Insets are the equivalent circuits. (c) Arrhenius curves and comparison of activation energies of bare Zn and Cu@Zn. (d) Chronoamperometry curves of bare Zn and Cu@Zn symmetric cells at a constant potential of −150 mV.

The Zn metal nucleation and growth behaviors on cycled Cu@Zn and Zn electrodes were further compared by SEM observations. Bare Zn anodes exhibited irregular and random Zn aggregates from 0.8 to 5 mAh cm^{-2} (Figure 4.24a), which can be explained by the continuous accumulation of Zn metal on the inhomogeneous nucleation sites[191]. In comparison, the Cu@Zn exhibited a dense and flat morphology during the whole plating process (Figure 4.24b). The structural integrity of Cu@Zn anodes was maintained upon cycling. FIB-SEM images of bare Zn after 20 cycles displayed severe structural damage with large voids and numerous pores (Figure 4.25a), which could impede the charge transfer and deteriorate the reversibility. In contrast, the cross-section of Cu@Zn remained dense without discernible voids or pores after

20 cycles (Figure 4.25b). The significantly different structural stability of bare Zn and Cu@Zn electrodes was further confirmed by extending the symmetric cells to 20th and 50th cycles (Figure 4.25c and 4.25d). Even after the 100th stripping cycle, Cu@Zn electrode still exhibits a smooth surface, demonstrating the duration and bifunctionality of our alloy interface (Figure 4.25e and Figure 4.26).

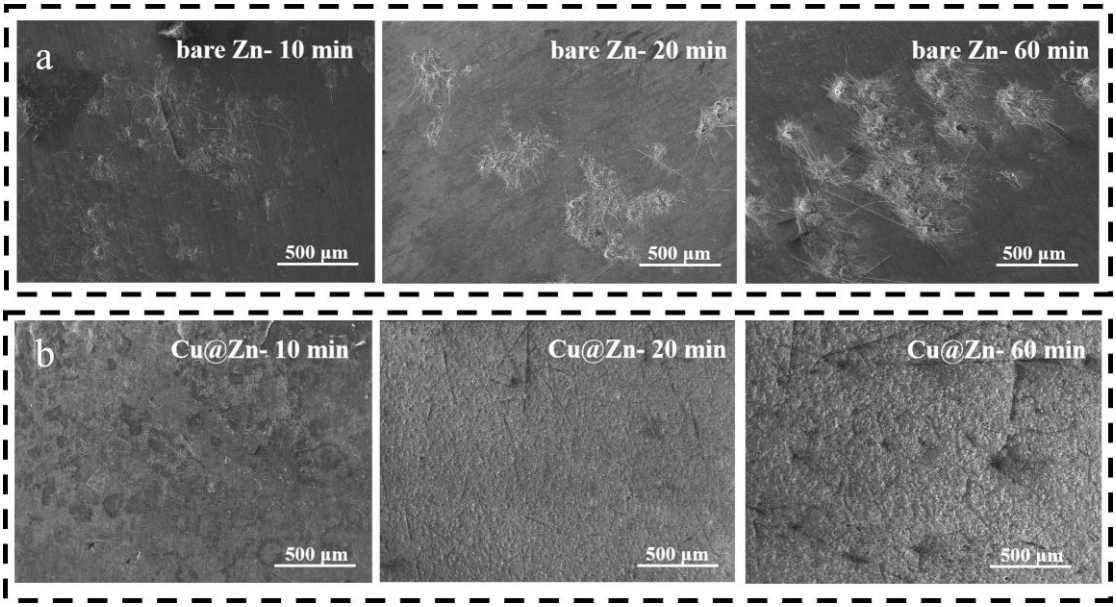

Figure 4.24 SEM images of Zn deposits on (a) bare Zn anode and (b) Cu@Zn anode by deposition for 10 min, 20 min, and 60 min at current density is 5 mA cm^{-2}, respectively.

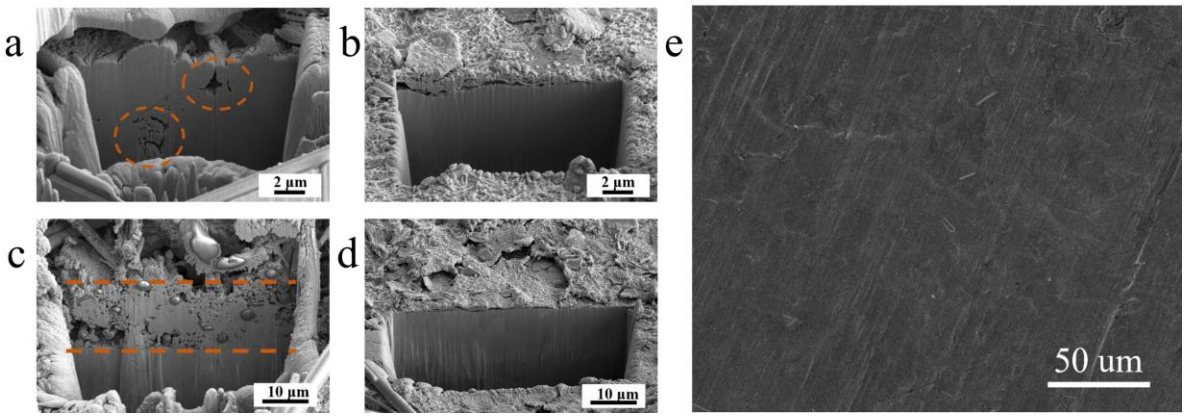

Figure 4.25 FIB-SEM images for the (a) bare Zn anode and (b) Cu@Zn anode after 20 cycles, (c) bare Zn and (d) Cu@Zn anode after 50 cycles at 1 mA cm^{-2}/1 mAh cm^{-2}. (e) SEM images of stripping side Cu@Zn after the 100th stripping cycles at 1 mA cm^{-2},1 mAh cm^{-2}.

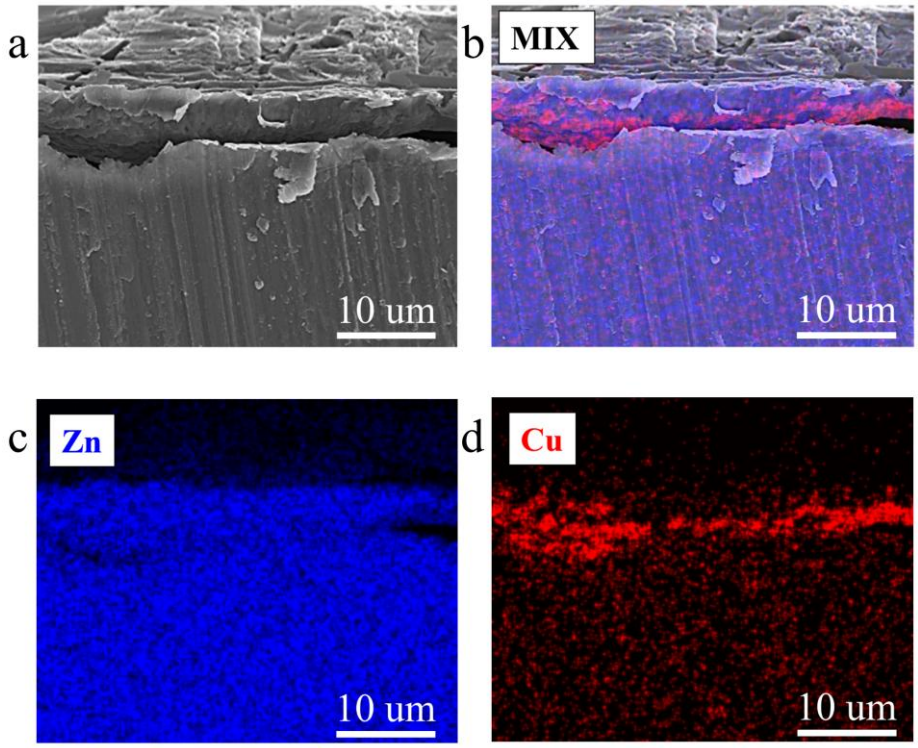

Figure 4.26 Plating side anode (a) Cross-sectional SEM images and (b-d) EDS elemental mappings for Cu@Zn after cycling.

Considering the significant effects of electric field and Zn^{2+} ion concentration on Zn metal nucleation and growth, dual-field simulations were performed through COMSOL to understand the role of the in-situ alloyed $CuZn_x$ layer in homogenizing the Zn^{2+} ion flux and current density. As shown in Figure 4.27a and Figure 4.27c, the Zn^{2+} ion distribution and current density on the surface of bare Zn show obvious gradients during Zn plating. A rapid confluence of Zn^{2+} ions towards the nucleation sites is observed from 0 to 200 s, as evidenced by a steep concentration flux[192]. The concentrated Zn^{2+} ions on the tips could cause the substantial electromotive force to propel dendritic deposition. The "tip effect" eventually promotes small protrusions into large dendrites[193]. In contrast, on the Cu@Zn surface, the uniformly distributed current density and Zn^{2+} ion flux ensures homogeneous Zn^{2+} deposition, resulting in uniform Zn nucleation (Figure 4.27b and Figure 4.27d). Consequently, the Cu@Zn electrodes maintain a flat and smooth surface even after long cycling periods.

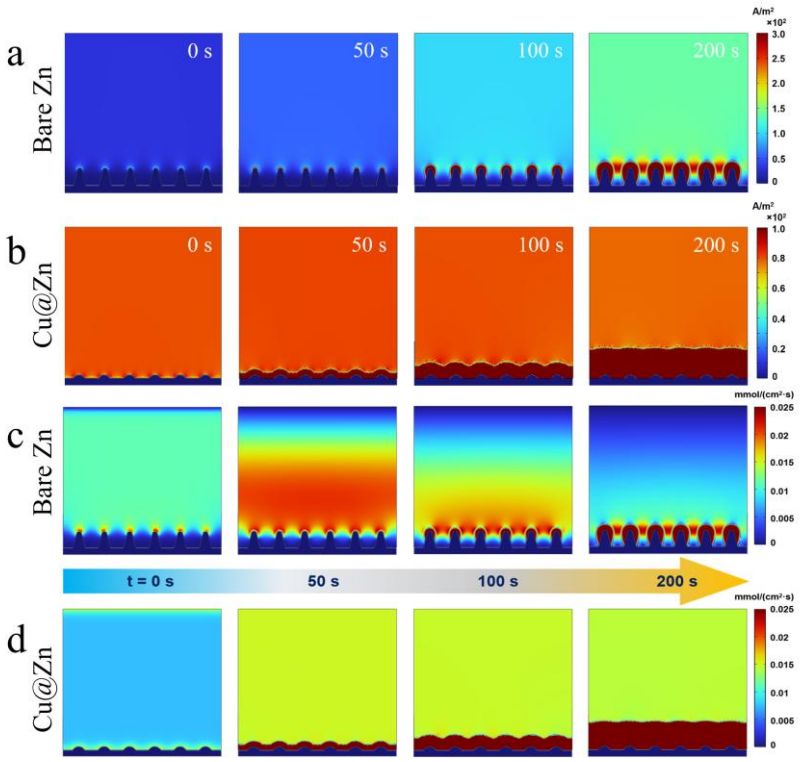

Figure 4.27 Simulation of surface current density distribution during the zinc plating process on (a) bare Zn and (b) Cu@Zn anode. Simulation of Zn^{2+} ion concentration distribution during the zinc plating process on (c) bare Zn and (d) Cu@Zn anode.

The working mechanisms of the Sabatier principle inspired Cu nanolayer have been revealed from the above results. At the early stage of stripping/plating cycles, the Cu nanolayer plays the role of uniform metal dissolution and will be electrochemically alloyed with Zn to form transition phases. As increasing the cycle number, more Zn atoms participate into the $CuZn_x$ alloying process, eventually stabilizing at the HCP-oriented $CuZn_5$ structure. The $CuZn_x$ nanolayer is electronically and ionically conductive, and mechanically robust. It homogenizes the Zn^{2+}ion flux as a secondary current collector during the plating process and provides uniform charge transfer kinetics for even Zn metal dissolution and deposition. Overall, the achievement of ultrastable Cu@Zn anodes can be attributed to the in-situ alloying $CuZn_x$ layers inspired by Sabatier principle.

4.2.4 Electrochemical performance in practical applications

In practice, the DOD (or utilization degree) of Zn anodes significantly determines the cycle life and energy density of AZMBs[194]. Most of the Zn anodes in literature are thick (≈100 μm, 45.96 mAh cm^{-2}) with extremely low DODs (less than 1%), resulting in low specific and volumetric energy densities that are not applicable for practical applications. When Zn metal is deeply discharged (or DOD> 50%), the hostless Zn metal would suffer an uneven stripping process and inevitable structural collapse, leading a limited cycle life. To estimate the practical potential of our Cu@Zn anodes, we measured the plating/stripping performance of symmetric cells under DODs ranging from 10% to 80%. At moderate current densities/capacities of 0.5 mA cm^{-2}/0.5 mAh cm^{-2} (DOD = 10%) and 0.92 mA cm^{-2}/0.92 mAh cm^{-2} (DOD = 20 % of a 10 um-thick Zn foil), the Cu@Zn anodes exhibited stable cycling over 1000 h (Figure 4.28a and 4.28c). In contrast, bare Zn anodes failed in less than 300 h and 500 h, respectively, with strong voltage fluctuations (Figure 4.28b and 4.28d). When we further increase the DOD to 80% (corresponding to 3.67 mA cm^{-2}/4.596 mAh cm^{-2}), the bare Zn anode failed after only 40 h with the occurrence of fluctuating voltage peaks and short-circuiting (Figure 4.28e). The Cu@Zn electrodes can be cycled to around 250 h with low overpotentials at 48 mV (Figure 4.28f). When we listed the cycle life of our Cu@Zn anodes with other high DOD Zn anodes in literature (Figure 4.29)[195-202], the Cu@Zn electrode stands out with the highest DOD value over 250 cycles.

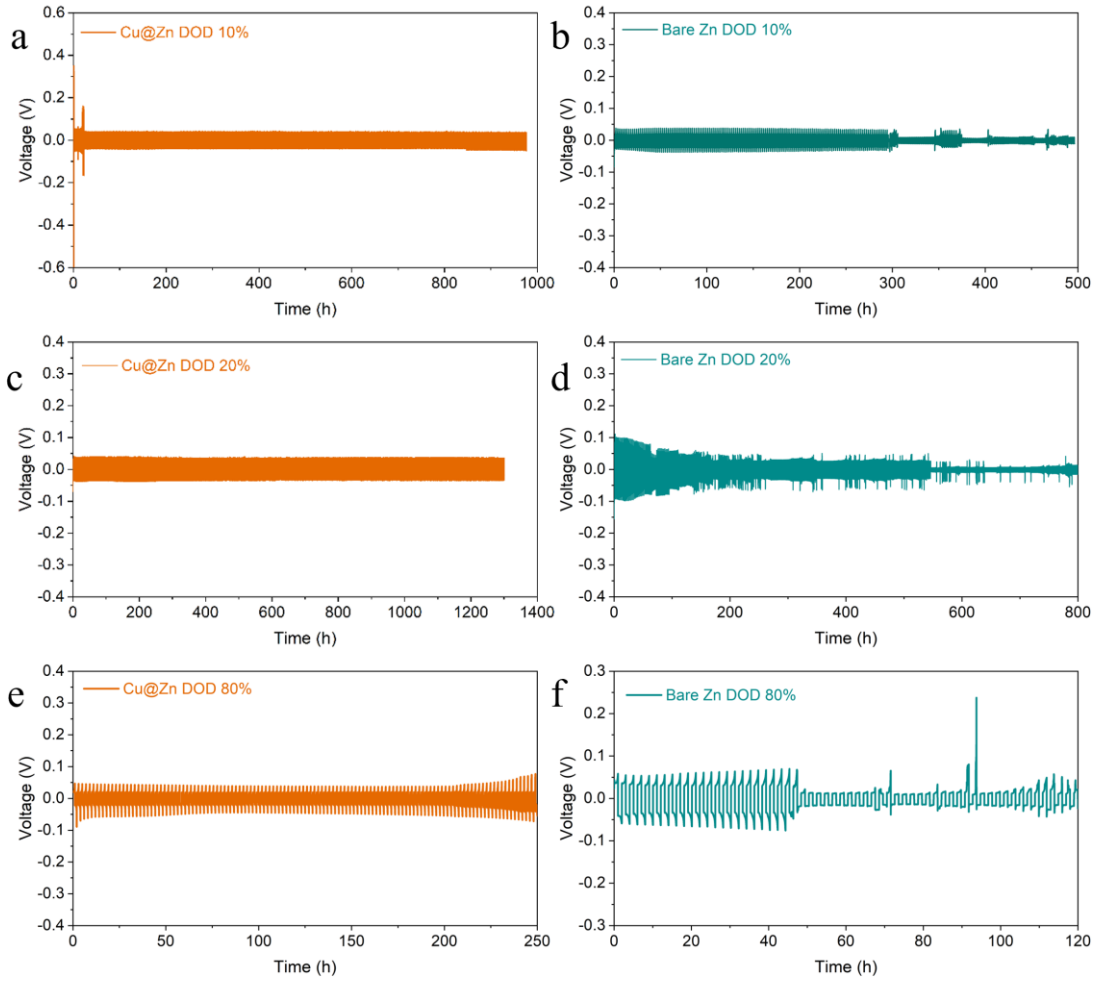

Figure 4.28 Cycling performance of (a, c, e) Cu@Zn//Cu@Zn and (b, d, f) bare Zn//Zn symmetric cells at DODs of 10 %, 20 % and 80%.

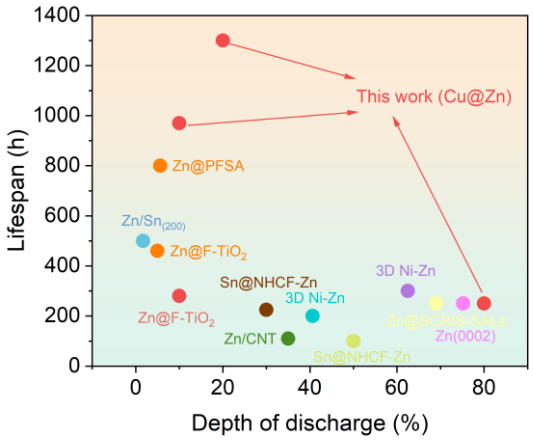

Figure 4.29 Comparison of depth of discharge and cycling life of Cu@Zn electrode with representative peer Zn anodes.

To assess the viability of the Cu@Zn anode, we constructed Cu@Zn||VO_2 full cells in 2M $ZnSO_4$ electrolyte, employing bare Zn||VO_2 cells as a control. The VO_2 nanorods were

synthesized by a hydrothermal method, and their morphologies were characterized using SEM and XRD (Figure 4.30). CV scanning of Cu@Zn||VO_2 full cells shows three pairs of reduction/oxidation peaks at 1.04/0.75, 0.72/0.51, and 0.63/0.43 V *vs.* Zn/Zn^{2+} (Figure 4.31a), which represent the reversible insertion/extraction of Zn^{2+} in VO_2 cathode. Zn||VO_2 cells display similar CV peaks but relatively lower current densities than these of Cu@Zn||VO_2 at the first cycle, suggesting the higher electrochemical reactivity of Cu@Zn anode[67]. Considering that during LSV testing, the current increases significantly when the voltage exceeds 1.2 V, the upper limit for testing is therefore set at 1.2 V to avoid destructive side reactions. CV tests also confirmed that the entire redox processes can be fully observed within the range of 0.1-1.2 V. Consequently, the voltage window for full-cell testing is determined to be 0.1-1.2 V. Figure 4.31b shows a lower R_{ct} for Cu@Zn||VO_2 cells (372 Ω) than the 1280 Ω for Zn||VO_2, which may be attributed to the enhanced charge transfer rates and Zn^{2+} diffusion kinetics for Cu@Zn.

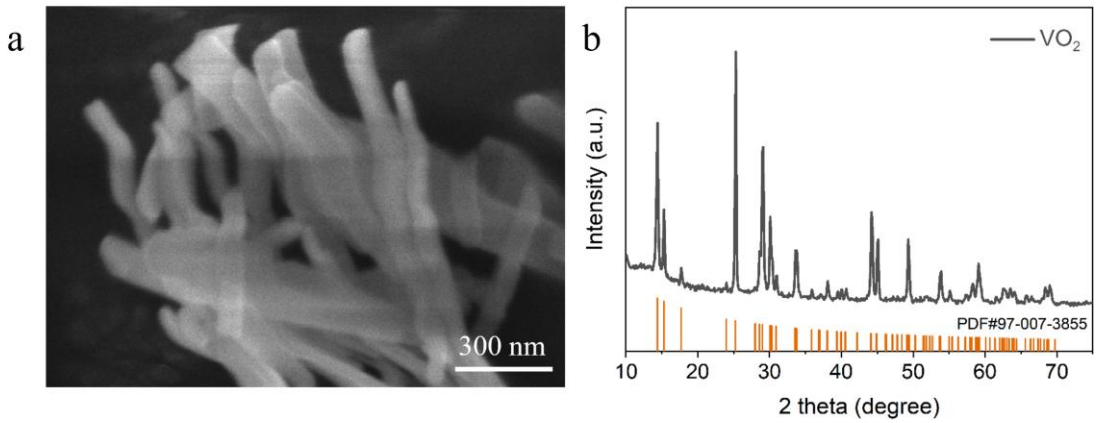

Figure 4.30 (a) SEM image of VO_2 nanorods and (b) XRD patterns of the VO_2 cathode material.

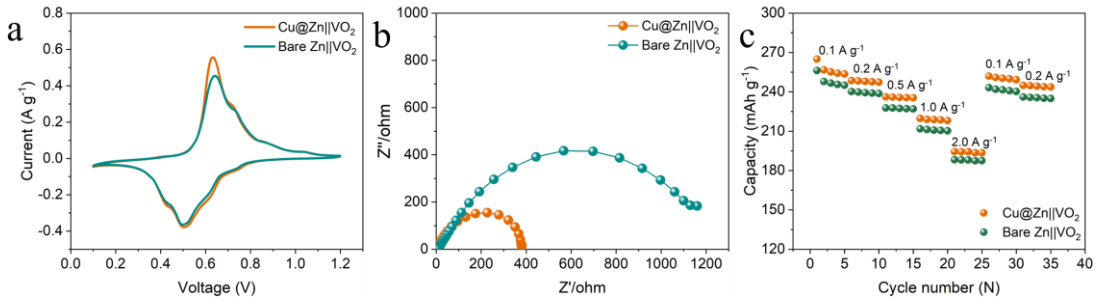

Figure 4.31 (a) Initial CV curves of bare Zn||VO_2 and Cu@Zn||VO_2 full cells. (b) Nyquist EIS plots of fresh full cells. (c) Rate performance of full cells.

The full cells were cycled at increasing current densities from 0.1 to 2.0 A g^{-1}. Figure 4.31c shows a higher discharge capacity of 255 mAh g^{-1} for Cu@Zn||VO_2 than the 247 mAh g^{-1} for bare Zn||VO_2 at 0.1 A g^{-1}, with the difference remaining at higher current rates. It may be caused by the rapid Zn dissolution and deposition and the reduced interfacial resistance for Cu@Zn anodes[179]. At a current density of 1.0 A g^{-1}, the Cu@Zn||VO_2 cell exhibits an initial capacity of ≈232.80 mAh g^{-1} and maintained ≈90.9% of its highest capacity after 800 cycles (Figure 4.32a). In contrast, the bare Zn||VO_2 showed a significant capacity decay of 16 % under the same testing conditions (Figure 4.32b)[196]. At a high current density of 2 A g^{-1}, the Cu@Zn||VO_2 exhibited a capacity retention of 88.0% (from 194.44 mAh g^{-1} to 171.11 mAh g^{-1}) without short circuit after 1000 cycles (Figure 4.32c). The curves of Zn||VO_2 full cells fluctuated at around 900th cycle in comparison, the final capacity decay is 23%. We also assembled full cells with ultrathin Zn anode (10 um) for cycling under a competitive DOD of approximate 40 % (Figure 4.32d). The Cu@Zn||VO_2 was able to cycle 500 times at 1A g^{-1} and retained 82.6% of its pristine capacity, which is much higher than the 60.8% for bare Zn||VO_2. These excellent results confirm that Cu@Zn anodes can significantly improve the stability of Zn metal full batteries.

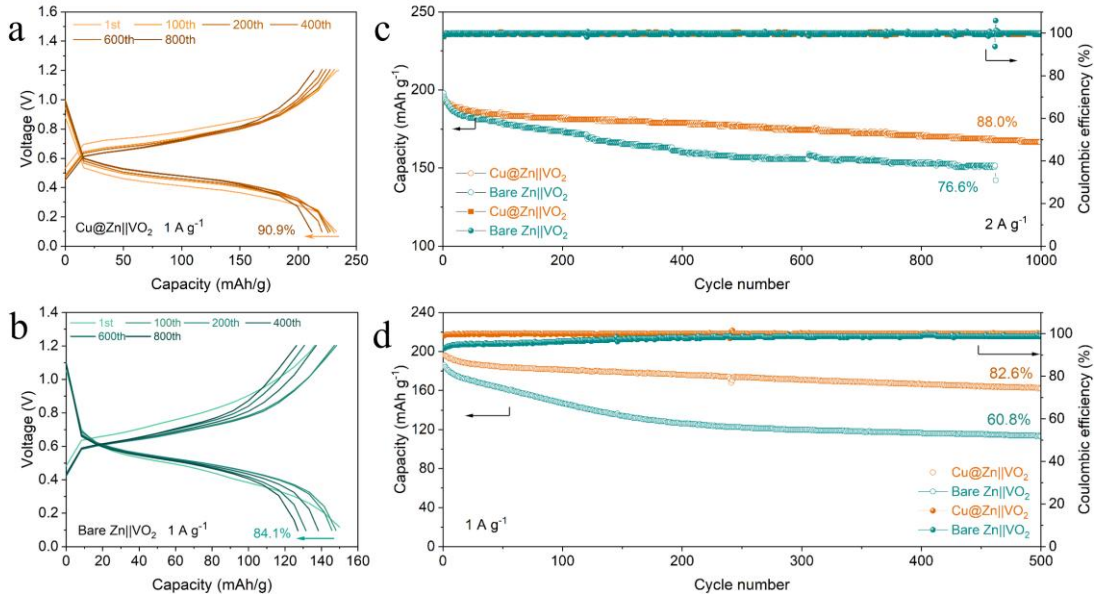

Figure 4.32 Galvanostatic charge/discharge profiles of (a) Cu@Zn||VO_2 and (b) bare Zn||VO_2 full cells at 1 A g^{-1}. (c) cycling capacities of Cu@Zn||VO_2 and bare Zn||VO_2 full cells at 2 A g^{-1}. (d) Cyclic performance of Cu@Zn||VO_2 and bare Zn||VO_2 full cells at 1 A g^{-1} over 500 cycles by using ultrathin Zn anodes of about 10 um in thickness.

4.3 Conclusion

In summary, this work establishes a screening mechanism (*i.e.,* analogous Sabatier principle) for a bifunctional interface (*i.e.,* buffer for uniform stripping and secondary current collector for plating) in high DOD (*i.e.,* 80%) Zn metal anodes. Drawing an analogy to the Sabatier principle for chemical catalysis, we find that a moderate TM-Zn interaction strength can favor the uniform stripping of Zn anodes. The flat and zincophilic interphase further regulates a dendrite-free and uniform Zn metal plating process. Atomic observations demonstrate a gradual phase evolution of Cu to $CuZn_x$ and $CuZn_5$ alloys. These phases exhibit high electronic conductivity, zincophilicity, and remarkable mechanical robustness, which collectively inhibit Zn dendrite growth during plating and suppress the pits during stripping. As a result, Cu@Zn anodes exhibited an extremely long cycle life of over 8000 hours (at 1 mA cm^{-2}/1 mAh cm^{-2}) in symmetric cells and high CEs of above 99.4% in asymmetric cells. At a high DOD of 80%, the Cu@Zn electrodes can be cycled over 250 hours, rivaling the state-of-the-art high-DOD Zn

anodes in literature. Furthermore, the Cu@Zn//VO_2 full cells deliver outstanding stability after 1000 cycles with a remarkable capacity retention of 92%. The like Sabatier principle is expected to guide the selection of TM interlayer for (electro)chemically stable metal anodes in rechargeable batteries.

Chapter 5 Atomic Sieve-Mediated Interface Enables 90% Utilization of Zinc Anodes

5.1 Introduction

The rational selection of interfacial layers can significantly enhance their protective efficacy. In the preceding chapter, inspired by the Sabatier principle, we established a heterometallic interface screening criterion that effectively mitigates electrode structural degradation induced by the stripping process through optimized interfacial charge transfer kinetics and mechanical stability. However, The practical deployment of metallic zinc anodes remains constrained by two persistent challenges: (i) the low zinc utilization efficiency (<5%) caused by the necessity of excess zinc loading to compensate for irreversible active material loss[154], and (ii) dendritic growth and parasitic side reactions exacerbated under high current density or deep discharge conditions[203]. These limitations stem from the non-uniform electric field distribution at the anode/electrolyte interface, which exacerbates localized Zn^{2+} flux heterogeneity and accelerates passivation layer formation.

Conventional optimization strategies (e.g., electrolyte additives, conductive framework construction) typically focus on alleviating individual failure mechanisms (e.g., dendrite growth or hydrogen evolution reaction), whereas interface engineering achieves simultaneous modulation of multiple critical parameters through atomic/molecular-level interface reconstruction. Common artificial interface materials can be broadly categorized into organic, inorganic, and metallic materials[204]. The majority of organic materials exhibit low electrical conductivity, which may elevate interfacial resistance and exacerbate polarization during Zn deposition/stripping processes[205]. This phenomenon can result in non-uniform Zn electrodeposition, generating localized high current density regions that paradoxically accelerate dendritic growth while simultaneously diminishing Zn utilization efficiency.

Inorganic materials (e.g., ZnO[206], ZrO_2[149]) generally demonstrate inherent brittleness, rendering them prone to crack propagation under the volume variation induced by Zn deposition/stripping cycles. Furthermore, densified inorganic coatings may impede the rapid transport of Zn^{2+} ions, particularly under high current density conditions. Moreover, these two types of materials typically exhibit electron-insulating properties while permitting solely ionic transport. Under high Zn utilization rates, the substantial Zn^{2+} flux traversing these artificial layers may compromise their structural integrity, thereby diminishing their long-term protective efficacy. Metallic materials exhibit high electronic conductivity, which significantly reduces interfacial resistance and promotes rapid charge transfer kinetics. However, the selection of metallic coatings is critically important, as inappropriate choices may induce structural degradation of zinc anodes during stripping processes[207]. Moreover, inadequate mechanical stability could compromise the long-term protective efficacy of these coatings[208]. These trade-offs highlight an urgent need for interfacial engineering paradigms that can reconcile high zinc utilization with long-term cycling stability under practical operating parameters.

In this work, we have developed a bilayer metal interface that integrates the buffering capability with the dual advantages of uniform zinc ion deposition. Under electrochemical conditions, a hollow-structured Cu_6Zn_{13} alloy was formed on the electrode surface. This phenomenon differs significantly from scenarios where single-layer metals are employed as buffer layers, which can be attributed to the ultrathin atomic sieve effect exhibited by the Ag interlayer. Owing to the dual protective mechanism, a stable zinc anode is attained even at high utilization rates. The Cu/Ag@Zn anodes demonstrate exceptional cycling stability, maintaining operation for over 5500 h at 5 mA cm^{-2} and over 500 h even at a 90% depth of discharge. They also demonstrate practical feasibility by maintaining 84.3 % capacity retention after 1000 cycles in Cu/Ag@Zn||VO_2 full cells. This work proposes a novel strategy to enhance the utilization

efficiency of zinc anodes and advance the commercialization of aqueous zinc batteries for large-scale energy storage applications.

5.2 Results and Discussion

5.2.1 The Critical Role of Initial Zinc Stripping Behavior

The discrepancy in cycle life between symmetric cells and full cells remains a persistent challenge in zinc metal battery systems[209]. This issue arises from the necessity to employ a significant excess of zinc to maintain supply during irreversible consumption, which substantially reduces energy density and further limits their broad applicability. Crucially, this performance gap originates from the neglected initial stripping behavior of zinc anodes in practical full cells[210]. As illustrated in Figure 5.1, pits emerge on the zinc anode surface during the initial stripping stage, with their dimensions progressively expanding as stripping capacity increases. During subsequent deposition, the sharp edges of these pits induce localized electric field concentration, driving preferential zinc-ion deposition at these sites and accelerating dendrite growth. To enhance depth of discharge (DOD), thinner zinc electrodes were implemented (Figure 5.2). Intriguingly, this modification exacerbates the consequences of heterogeneous stripping behavior: uneven zinc dissolution generates extensive internal voids within the electrode. These voids disrupt electron transport pathways, eliminate nucleation sites, and significantly increase charge transfer resistance[208].

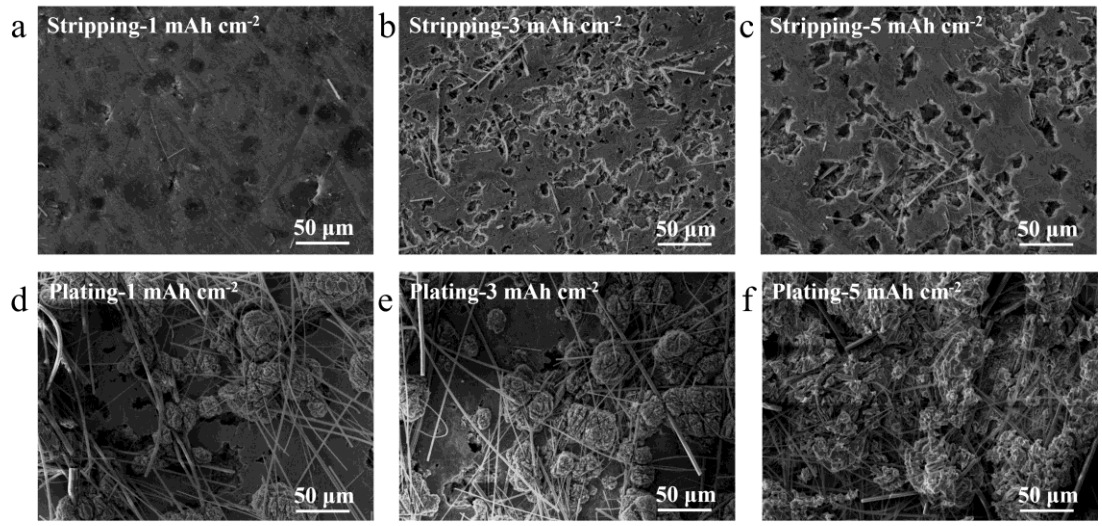

Figure 5.1 SEM images of bare Zn electrodes after stripping by (a) 1 mAh cm^{-2}, (b) 3 mAh cm^{-2} and (c) 5 mAh cm^{-2} at 5 mA cm^{-2} and then plating by (d-f) 1 mAh cm^{-2}, 3 mAh cm^{-2} and 5 mAh cm^{-2} at 5 mA cm^{-2}.

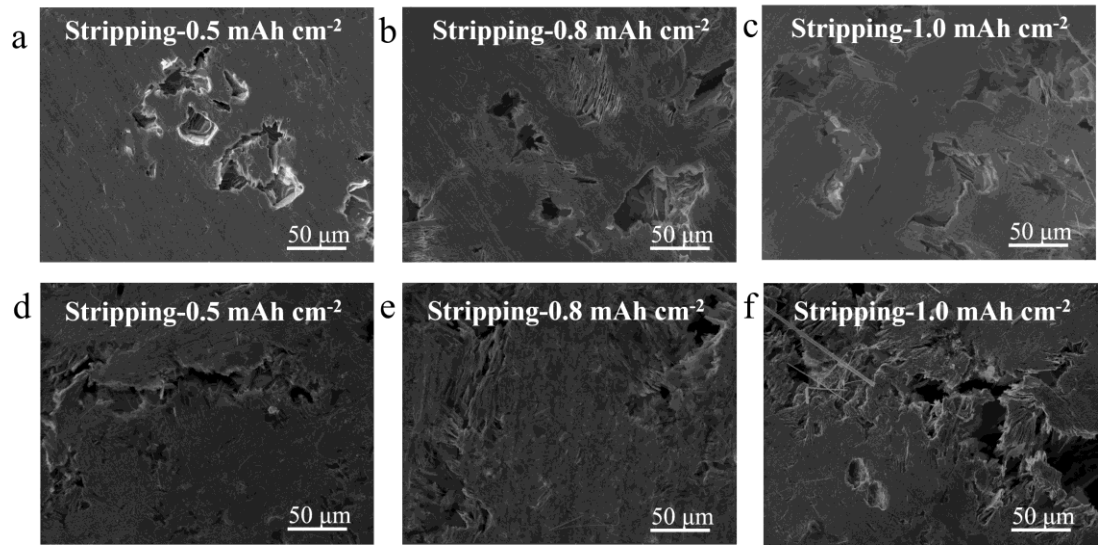

Figure 5.2 Morphological evolution of stripping processes. SEM images of 0.03mm bare Zn electrodes after stripping by (a) 0.5 mAh cm^{-2}, (b) 0.8 mAh cm^{-2} and (c) 1.0 mAh cm^{-2} at 1 mA cm^{-2}. SEM images of 0.01mm bare Zn electrodes after stripping by (a) 0.5 mAh cm^{-2}, (b) 0.8 mAh cm^{-2} and (c) 1.0 mAh cm^{-2} at 1 mA cm^{-2}.

To mitigate heterogeneous dissolution and deposition of zinc metal anodes, we engineered a bilayer Cu/Ag nanolayer (thickness ≈200 nm) on zinc surfaces via magnetron sputtering. This mechanically robust bimetallic architecture demonstrates dual functionality: during discharge,

it stabilizes zinc dissolution through constrained electrochemical reactions, while in subsequent charging cycles, it modulates homogeneous zinc deposition via interfacial charge redistribution. Consequently, the transition metal interlayer serves not only as a protective coating against surface degradation but also as a secondary current collector, enabling dendrite-free zinc metal anode operation through synergistic mechanical-electrochemical regulation. To validate the necessity and efficacy of our bilayer metallic architecture, we conducted comparative electrochemical evaluations between the optimized electrodes and bare zinc anodes. Figure 5.3a-c delineates the surface topographies of both pristine Zn and Cu/Ag@Zn electrodes after 5 mAh cm^{-2} stripping. The Cu/Ag@Zn configuration demonstrated markedly enhanced uniformity in zinc dissolution compared to its bare counterpart. Remarkably, the flattened electrode morphology resulting from homogeneous stripping enables ordered zinc-ion deposition during subsequent plating cycles, ultimately achieving densely packed and dendrite-free zinc morphologies with submicron-scale surface roughness (Figure 5.3d-f).

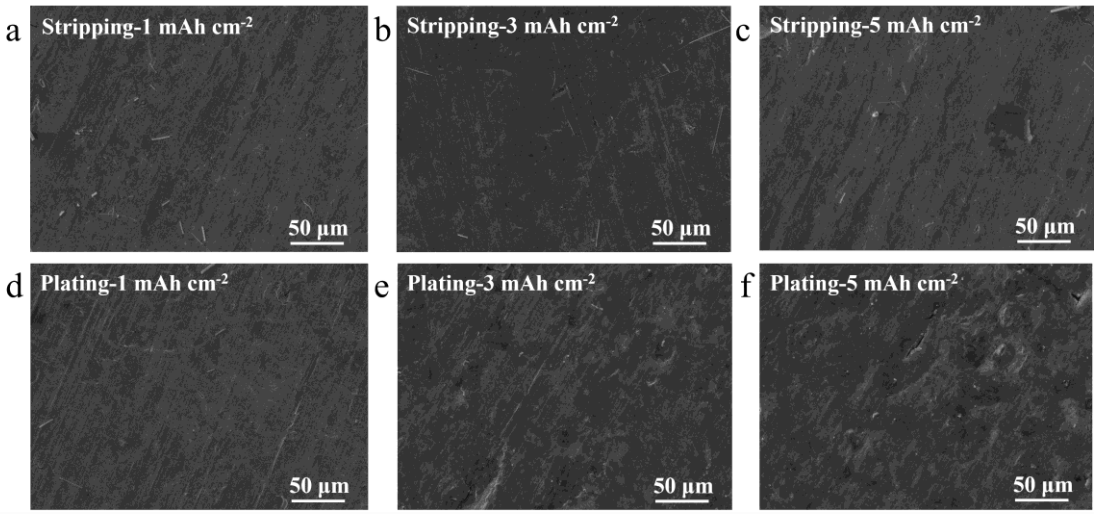

Figure 5.3 SEM images of Cu/Ag@Zn electrodes after stripping by (a) 1 mAh cm^{-2}, (b) 3 mAh cm^{-2} and (c) 5 mAh cm^{-2} at 5 mA cm^{-2}, and then plating by (d-f) 1 mAh cm^{-2}, 3 mAh cm^{-2} and 5 mAh cm^{-2} at 5 mA cm^{-2}.

To probe the structural resilience under elevated zinc utilization, we systematically investigated stripping behaviors using zinc foils with reduced thicknesses (0.03 mm and 0.01 mm,

corresponding to 7% and 20% Zn utilization respectively), as shown in Figure 5.4. Strikingly, unlike bare Zn electrodes that exhibited catastrophic structural collapse, the Cu/Ag@Zn configuration maintained structural integrity, as evidenced by cross-sectional analysis via focused ion beam-scanning electron microscopy (FIB-SEM). Progressive stripping depth in bare Zn induced substantial internal fractures (Figure 5.5), with interconnected microcracks predisposing the electrode to rapid mechanical-electrochemical failure. In contrast, the cross-section of the Cu/Ag@Zn electrode consistently displayed a well-preserved structure. Enhancing the structural stability of the electrode during cycling is crucial for achieving high zinc utilization rates[170, 211]. This mechanistic study confirms that engineered interface stability is a critical determinant for achieving practical high-zinc-utilization batteries.

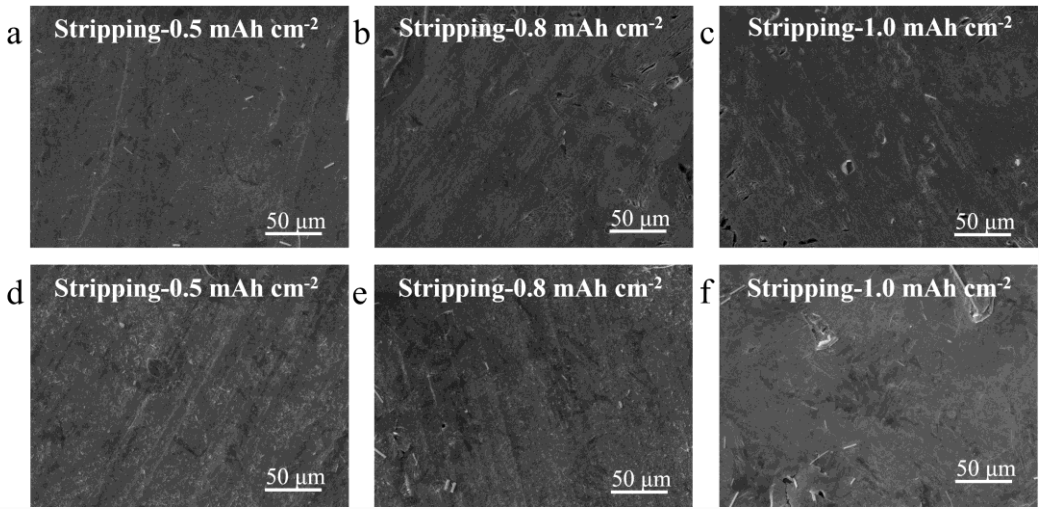

Figure 5.4 Morphological evolution of stripping processes. SEM images of 0.03mm Cu/Ag@Zn electrodes after stripping by (a) 0.5 mAh cm^{-2}, (b) 0.8 mAh cm^{-2} and (c) 1.0 mAh cm^{-2} at 1 mA cm^{-2}. SEM images of 0.01mm Cu/Ag@Zn electrodes after stripping by (a) 0.5 mAh cm^{-2}, (b) 0.8 mAh cm^{-2} and (c) 1.0 mAh cm^{-2} at 1 mA cm^{-2}.

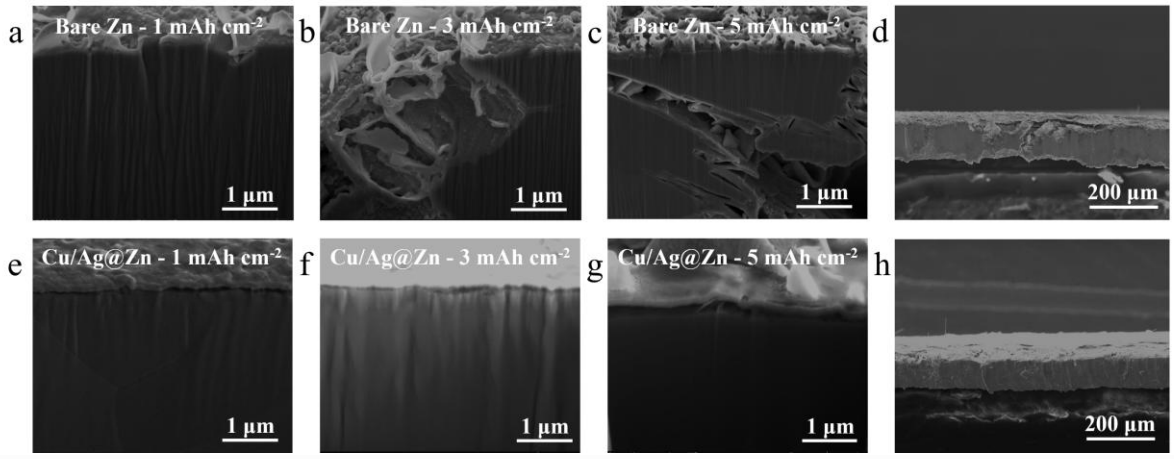

Figure 5.5 FIB-SEM images for the (a-c) bare Zn and (e-g) Cu/Ag@Zn electrodes after stripping 1 mAh cm^{-2}, 3 mAh cm^{-2} and 5 mAh cm^{-2} at 5 mA cm^{-2}. Side view SEM images of stripped (d) bare Zn and (h) Cu/Ag@Zn by a capacity of 5 mAh cm^{-2} at 5 mA cm^{-2}.

5.2.2 Characterization of the Cu/Ag@Zn Electrode and Electrochemical Behavior

We fabricated silver and copper layers sequentially on the zinc metal surface via magnetron sputtering, with each metallic layer exhibiting a thickness of approximately 100 nm (Figure 5.6). TEM analysis revealed a well-defined dual-layer structure on the zinc electrode surface, while elemental mapping further demonstrated the uniform spatial distribution of the sputtered metallic coatings. The phase composition of the Cu/Ag@Zn electrode was characterized by grazing-incidence X-ray diffraction (GI-XRD), where the characteristic diffraction peaks of metallic silver, copper, and zinc were all identified in the pristine sample (Figure 5.7a). The contact angle of water drops on pure Zn is 97.5°. After the coating of Cu/Ag layer, the contact angle decreased slightly (Figure 5.7b-c). Furthermore, depth-profiling X-ray photoelectron spectroscopy (XPS) analysis confirmed the discrete stratification of copper and silver layers through sequential sputter-etching cycles (Figure 5.7d-f).

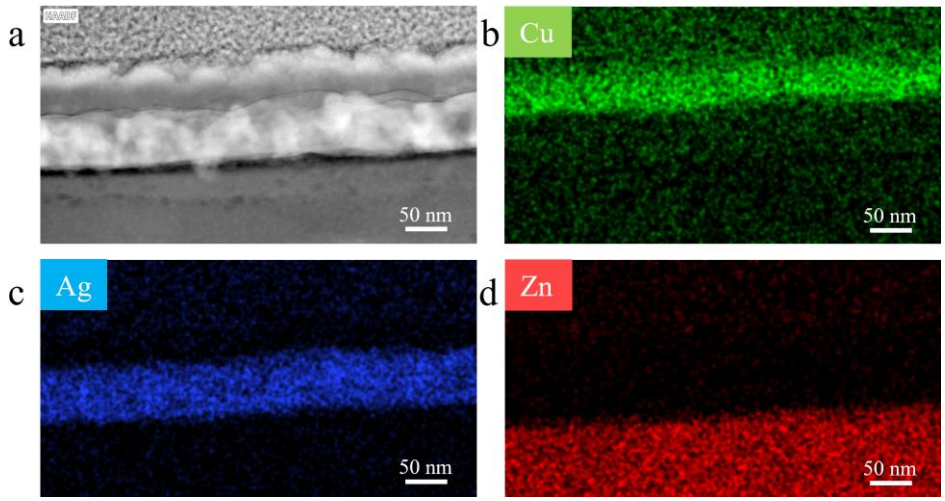

Figure 5.6 TEM image and EDS mapping of the pristine Cu/Ag@Zn electrode. FIB-cutting is applied to obtain the cross-section information of Cu/Ag@Zn sample.

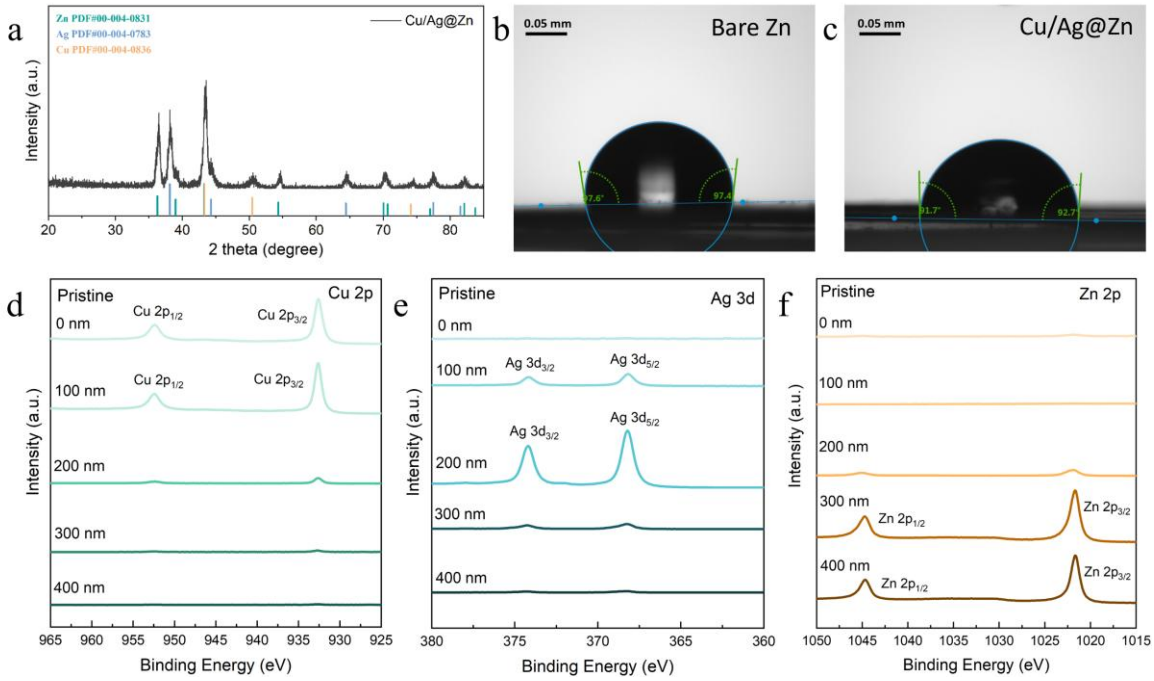

Figure 5.7 (a) GI-XRD curves of pristine Cu/Ag@Zn. Contant angles of (b) bare Zn and (c) Cu/Ag@Zn. XPS curves of pristine Cu@Zn from the surface to 400 nm: (d) Cu 2p, (e) Ag 3d and (f) Zn 2p curves.

Benefiting from the protective Cu/Ag composite coating, the zinc corrosion induced by parasitic side reactions between the anode and electrolyte is significantly mitigated. As shown in Figure 5.8a, the protected Zn exhibits a corrosion potential positively shifted from -0.987 V (bare Zn) to -0.984 V, accompanied by a substantial reduction in corrosion current density from

3.30 mA cm^{-2} to 1.48 mA cm^{-2}. These electrochemical parameters indicate decreased thermodynamic propensity for corrosion and slower corrosion kinetics[212]. Linear sweep voltammetry (LSV) measurements at 5 mV s^{-1} reveal distinct interfacial behaviors: the bare Zn anode demonstrates rapidly accelerating cathodic current density (Figure 5.8b), whereas the modified anode maintains significantly restrained current evolution. These observations confirm the dual functionality of the Cu/Ag coating in suppressing hydrogen evolution reaction (HER) and enhancing corrosion resistance in aqueous electrolytes.

Notably, polarization hysteresis analysis during rate performance testing reveals a critical distinction. The Cu/Ag@Zn symmetric cell maintains stable voltage hysteresis values of 23, 32, 35, 42, and 51 mV across current densities from 0.5 to 8.0 mA cm^{-2}, markedly lower than those of bare Zn counterparts (Figure 5.8c). Particularly concerning is the premature short-circuit failure observed in bare Zn cells upon returning to 0.5 mA cm^{-2}. Further evaluation of cycling reversibility through coulombic efficiency (CE) analysis, calculated as the ratio of stripping-to-plating capacity, demonstrates exceptional stability: the Cu/Ag@Zn configuration sustains 99.5% average CE over 1500 cycles, contrasting sharply with the bare Zn's severe CE fluctuations and complete failure within 100 cycles (Figure 5.8d). This optimized deposition/stripping behavior provides fundamental advantages for achieving superior zinc utilization efficiency.

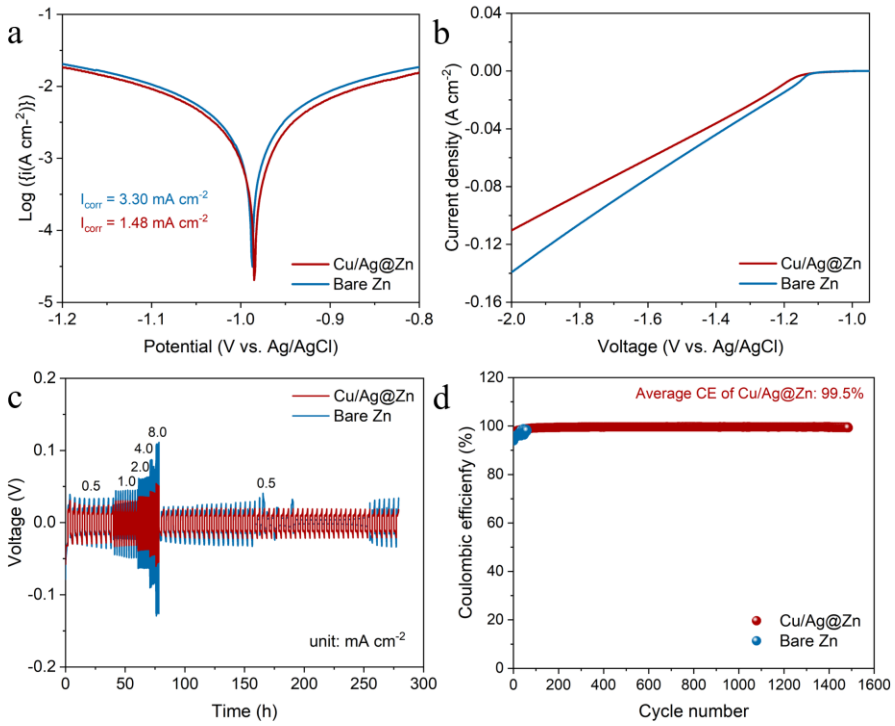

Figure 5.8 (a) Tafel polarization curves of bare Zn and Cu/Ag@Zn. (b) Linear polarization curves for the corrosion of bare Zn and Cu/Ag@Zn. (c) Rate performances of the six kinds of symmetric cells at current densities from 0.5 to 8 mA cm^{-2} and a constant capacity of 1 mAh cm^{-2}. (d) CEs of bare Zn and Cu/Ag@Zn electrodes in asymmetric cells at 1 mA cm^{-2} and 1 mAh cm^{-2}.

To demonstrate the superiority of Cu/Ag@Zn anode, the symmetric cells were initially measured to evaluate the long-term cycling stability at a current density of 1.0 mA cm^{-2} with an areal capacity of 1.0 mAh cm^{-2}. As expected, the Cu/Ag@Zn symmetrical cell maintains superior cycle stability for 3700 h with a low overpotential of 25 mV. While for the bare Zn, the polarization voltage suddenly increases accompanied by the cell failure after only 107 h, resulting from the accumulation of "dead" Zn and by-products, as shown in Figure 5.9a. When the current density was increased to 5 mA cm^{-2}, the Cu/Ag@Zn electrode still exhibited exceptional cycling longevity. In contrast to the bare Zn anode, which experienced a short circuit after 300 hours of cycling, the Cu/Ag@Zn symmetric cell demonstrated stable operation exceeding 5500 hours (Figure 5.9b).

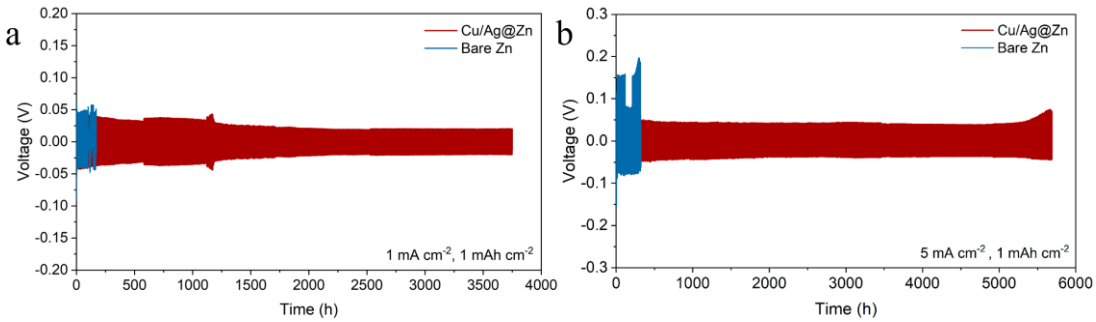

Figure 5.9 Long-term cycling of symmetrical cells at (a) 1 mA cm^{-2} with 1 mAh cm^{-2} and (b) 5 mA cm^{-2} with 1 mAh cm^{-2}.

This study systematically investigates the mechanistic role of composite current collector (Cu/Ag) coatings in zinc metal anodes. By constructing symmetric cell configurations, the zinc nucleation and deposition kinetics were characterized through chronoamperometry (CA) under a constant overpotential of -150 mV[210]. The oscillatory characteristics of current-time curves effectively reveal the nucleation behavior and morphological evolution on electrode surfaces. Experimental data demonstrate that bare zinc electrodes exhibit continuous current density escalation beyond 300 seconds (Figure. 5.10a), attributable to uncontrolled dendritic growth triggered by two-dimensional diffusion failure of zinc ions. Specifically, zinc ions preferentially undergo lateral diffusion to minimize surface energy exposure, thereby inducing directional aggregation of deposits into dendritic architectures. In stark contrast, the Cu/Ag@Zn composite electrode transitions from transient two-dimensional diffusion to a stabilized three-dimensional compact diffusion mode. This mechanistic shift confirms the homogeneous zinc-ion deposition characteristics on the Cu/Ag composite surface. To further validate the superiority of the composite current collector, asymmetric cell configurations (Zn//Cu and Cu/Ag@Zn//Cu) were employed to examine the evolution of nucleation overpotential. Defined as the potential difference between peak potential and plateau potential, this parameter serves as a critical indicator for evaluating long-term cycling stability. At a current density of 5.0 mA cm^{-2}, the Cu/Ag@Zn electrode exhibits a nucleation overpotential of 34.5 mV, significantly lower than the 46.4 mV observed for bare zinc electrodes, as shown

in Figure 5.10b. This discrepancy directly reflects the reduced energy barrier for zinc deposition facilitated by the composite current collector. The experimental evidence conclusively demonstrates that the Cu/Ag composite layer enhances zinc deposition kinetics while effectively suppressing energy barrier accumulation during nucleation through optimized charge distribution and reduced interfacial impedance.

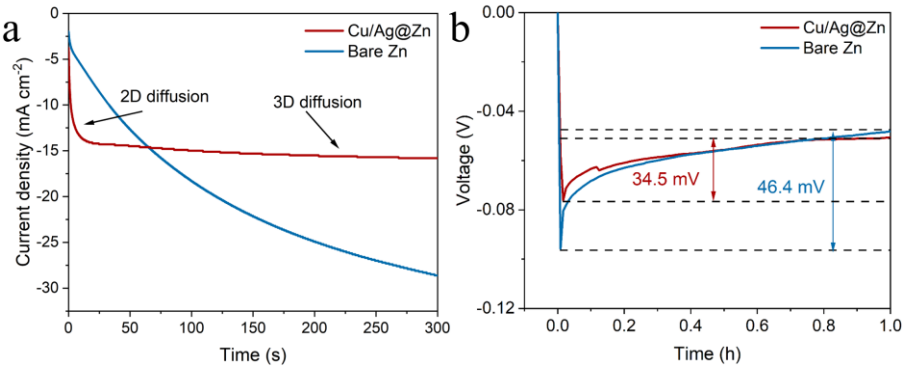

Figure 5.10 Chronoamperometry curves of bare Zn and Cu/Ag@Zn at a constant potential of -150 mV. (b) Polarization curves of Zn deposition at 5 mA cm^{-2} for 1 hour.

The Zn metal nucleation and growth behaviors on cycled Cu@Zn and Zn electrodes were further studied by SEM observations. Bare Zn anodes exhibited irregular and random Zn aggregates from 1.0 to 5 mAh cm^{-2} (Figure 5.11a), attributable to the continuous accumulation of Zn metal at heterogeneous nucleation sites. In contrast, the Cu@Zn electrodes maintained a dense and flat morphology throughout the entire plating process (Figure 5.11b). Furthermore, in situ optical microscopy was employed to directly visualize the morphological evolution of zinc plating/stripping processes. As illustrated in the Figure 5.12b, under a stripping current density of 2 mA cm^{-2}, distinct uneven stripping patterns emerge on the bare zinc electrode surface at 10 minutes, with progressively exacerbated interfacial heterogeneity as stripping duration extends. Additionally, substantial bubble formation is observed on the bare zinc electrode due to hydrogen evolution reaction (HER) activity. In contrast, the Cu/Ag@Zn electrode maintains a homogeneous and intact interface throughout the stripping process (Figure 5.12a). This interfacial disparity during the stripping phase critically influences

subsequent deposition behavior. The bare zinc surface exhibits irregular zinc deposition within 10 minutes of plating, with protruding deposits gradually evolving into characteristic dendritic structures as plating time increases (Figure 5.13b). Conversely, the Cu/Ag@Zn electrode consistently demonstrates smooth and compact surface morphology without discernible dendrite formation, highlighting its superior interfacial stability and dendrite-suppressing capability (Figure 5.13a).

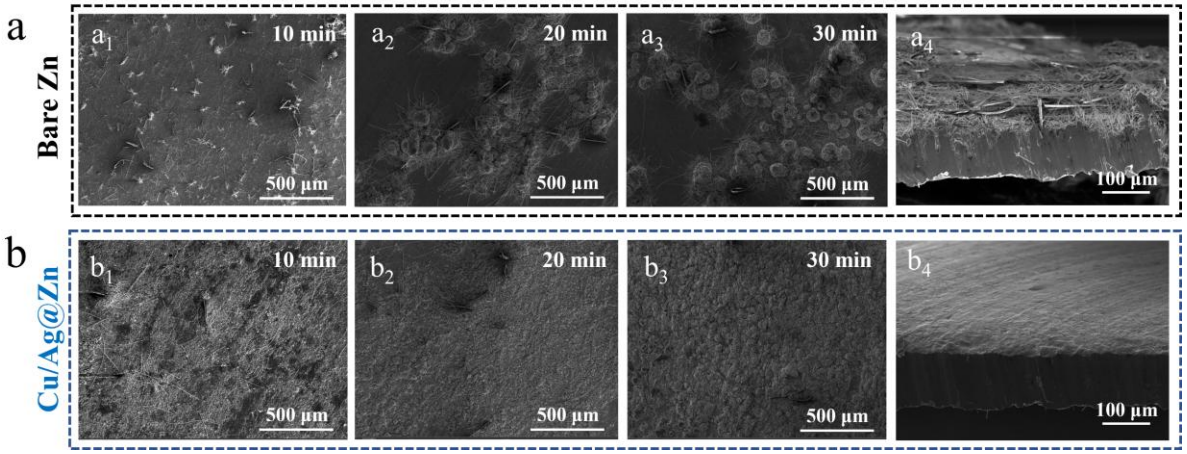

Figure 5.11 SEM images of Zn deposits on (a) bare Zn anode and (b) Cu/Ag@Zn anode by deposition for 10 min, 20 min, and 60 min at current density is 5 mA cm^{-2}, respectively.

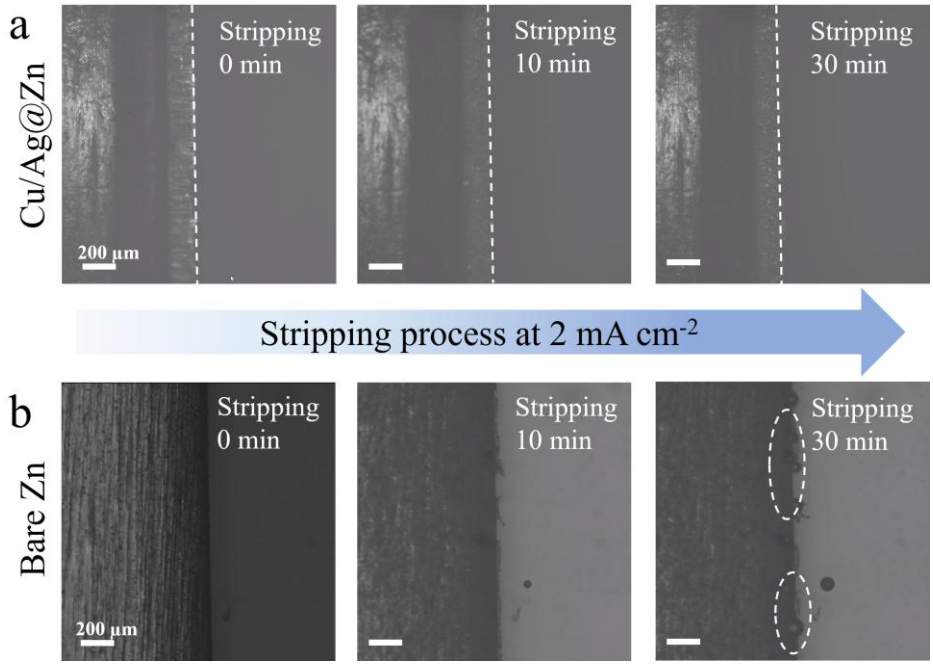

Figure 5.12 *In-situ* optical microscope images of Zn stripping behaviors of a) bare Zn and b)

Cu@Zn electrodes at a current density of 2 mA cm^{-2} for 30 min.

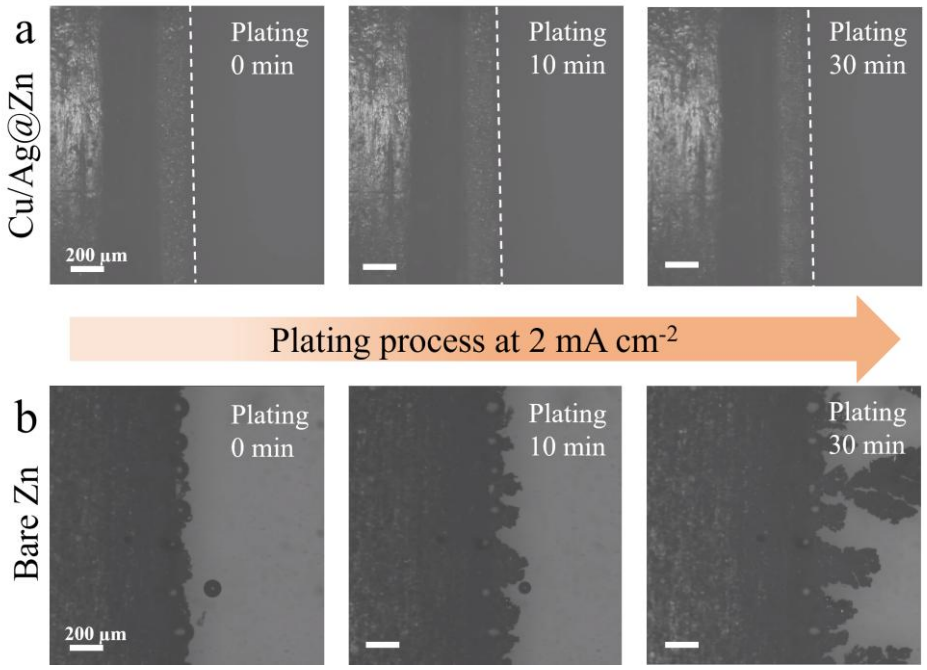

Figure 5.13 *In-situ* optical microscope images of Zn plating behaviors of a) bare Zn and b) Cu@Zn electrodes at a current density of 2 mA cm^{-2} for 30 min.

Given the critical battery failure mechanisms induced by zinc dendritic side reactions, which become increasingly pronounced during cycling in aqueous zinc-ion batteries, atomic force microscopy (AFM) was utilized to elucidate zinc deposition mode and further investigate the protective efficacy of the Cu/Ag layer on zinc anodes (Figure 5.14a-b). Owing to heterogeneous zinc deposition, severe surface roughening with large dendritic protrusions—a potential precursor to internal short circuits—was observed on bare zinc anodes after 50 cycles in 2 M $ZnSO_4$ electrolyte. Notably, under identical testing conditions (1 mA cm^{-2}, 1 mAh cm^{-2}), the Cu/Ag@Zn anode retained exceptional surface smoothness. These findings were corroborated by focused ion beam-scanning electron microscopy (FIB-SEM) analysis. As shown in Figure 5.14c-d, Cross-sectional imaging revealed porous architectures within the bare zinc electrode alongside irregular surface deposits, whereas the Cu/Ag@Zn electrode exhibited a defect-free surface and densely packed internal morphology.

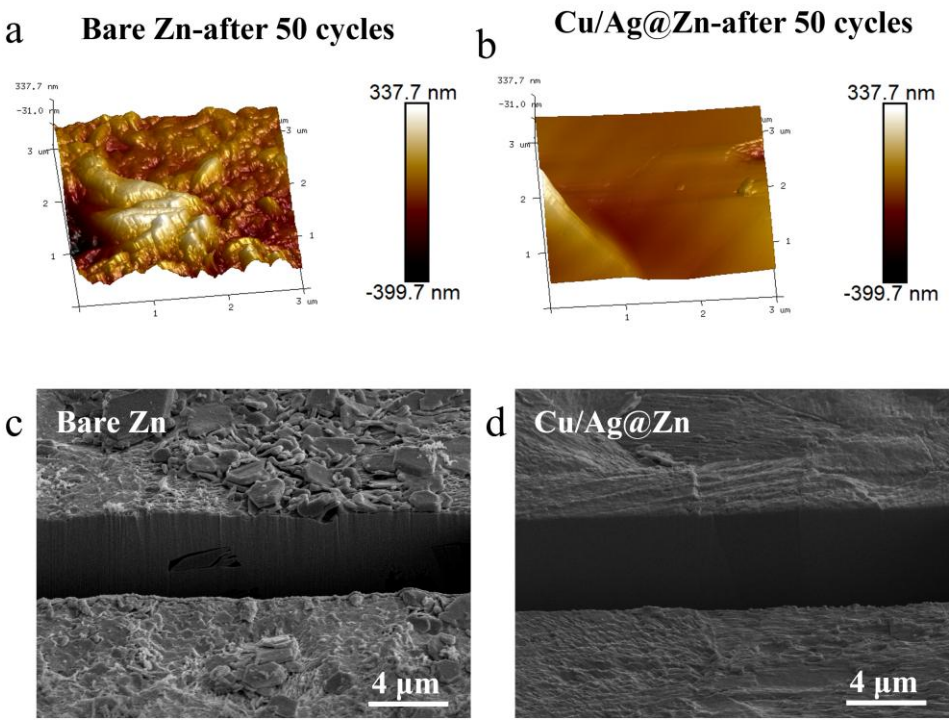

Figure 5.14 AFM images of (a) bare Zn and (b) Cu/Ag@Zn after 50 cycles at 1 mA cm^{-2}, 1 mAh cm^{-2}. Fib-SEM images for the (c) bare Zn and (d) Cu/Ag@Zn after 50 cycles.

Collectively, the multi-faceted experimental results—electrochemical cycling, nanoscale surface characterization, and microstructural analysis—demonstrate that the Cu/Ag composite layer effectively regulates zinc deposition/stripping processes by homogenizing ion flux distribution, mitigating localized stress accumulation, and suppressing dendrite nucleation.

5.2.3 Working Mechanisms of Cu/Ag Interface to Stabilize Zn Anode

To elucidate the mechanistic role of the Cu/Ag interface in stabilizing zinc anodes, we conducted a comprehensive structural characterization of the Cu/Ag@Zn electrode through multi-dimensional analytical techniques, including X-ray photoelectron spectroscopy (XPS), X-ray diffraction (XRD), and scanning transmission electron microscopy (STEM). We conducted detailed microscopic characterization of samples subjected to varying degrees of electrical cycling. Samples were selected after 20 cycles for the earlier reaction stage and 50 cycles for the later reaction stage (denoted as Cu/Ag@Zn-20 and Cu/Ag@Zn-50). High-

resolution X-ray photoelectron spectroscopy (XPS) was systematically utilized to investigate the chemical speciation of the cycled Cu/Ag@Zn electrode. Comprehensive depth-profiling analysis via Ar^+ sputtering, as illustrated in Figure 5.15, demonstrates prominent Zn 2p photoelectron signatures dominating the near-surface region, accompanied by attenuated Cu 2p and Ag 3d spectral intensities. This observed elemental distribution heterogeneity can be attributed to the preferential electrochemical deposition of metallic Zn onto the secondary current collector during cycling, which effectively masks the underlying Cu substrate and Ag-containing components. Through depth-resolved etching analysis, we observed a distinct deviation from the initial specimen. The Zn 2p photoelectron signals exhibited coexistence with Cu 2p and Ag 3d spectral features at identical sputtering depths. Furthermore, pronounced stratification phenomena were identified in the elemental distribution profiles of Cu 2p and Ag 3d, necessitating further mechanistic investigation into the interfacial evolution with electrochemical cycling conditions.

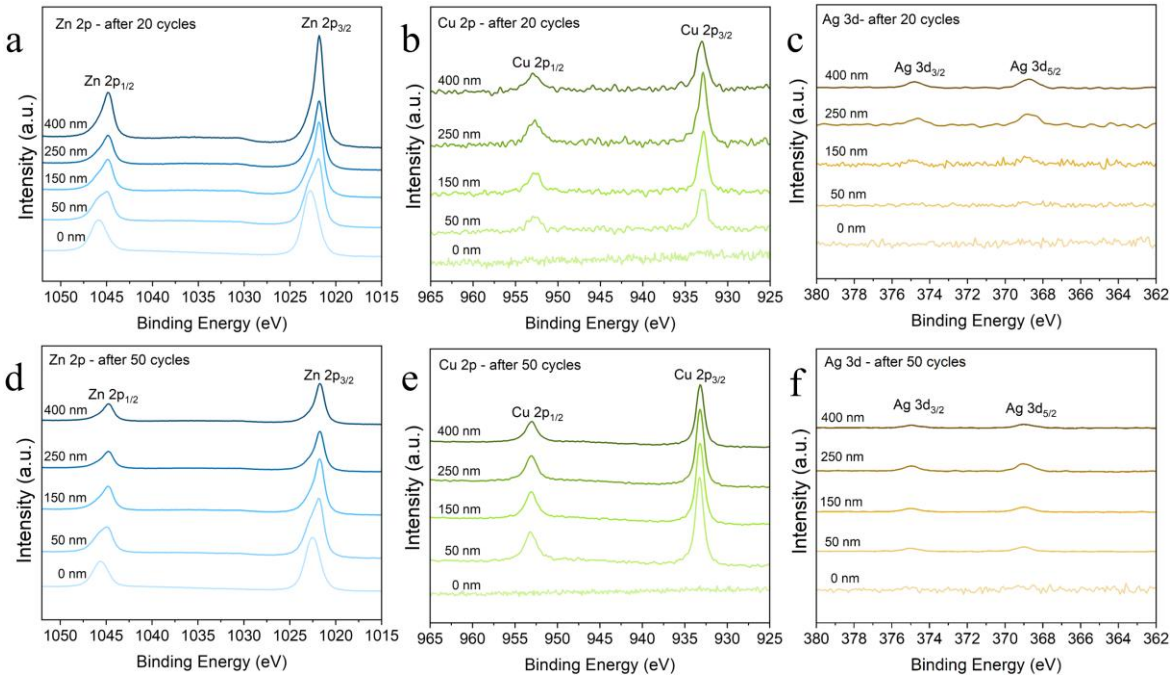

Figure 5.15 XPS curves for (a) Zn 2p, (b) Cu 2p and (c) Ag 3d of Cu/Ag@Zn after 20 cycles. (d) Zn 2p, (e) Cu 2p and (f) Ag 3d of Cu/Ag@Zn after 50 cycles.

The high-angle annular dark-field scanning transmission electron microscopy (HAADF-STEM)

images and corresponding energy-dispersive X-ray spectroscopy (EDS) images of the Cu/Ag@Zn-20 samples are presented in Figure 5.16. As shown, the samples still exhibit a distinct layered structure, with the Cu layer (green) and Ag layer (blue) maintaining a morphology similar to that before the reaction, retaining their metallic structures (Figure 5.17a-b). The microstructural analysis reveals that the silver layer adjacent to the zinc substrate has undergone partial alloying, forming $AgZn_3$ (Figure 5.17c), while the overlying copper layer has also alloyed with zinc. Notably, the EDS results (59.7% Zn, 39.9% Cu, and 0.4% Ag) combined with atomic-resolution HAADF-STEM imaging (Figure 5.17d) confirm the presence of a previously unreported Cu-Zn alloy phase with an approximate stoichiometric ratio of Cu:Zn = 2:3. This observation suggests that interfacial reactions between Cu, Ag, and Zn lead to the formation of distinct intermetallic phases, which may play a critical role in stabilizing the zinc anode. The detection of such an alloy phase underscores the complex interfacial chemistry at play and warrants further investigation into its structural and electrochemical implications.

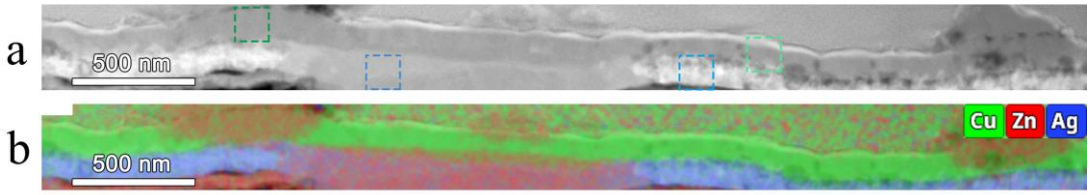

Figure 5.16 (a) HAADF-STEM image and the corresponding (b) XEDS image of the sample after 20 cycles.

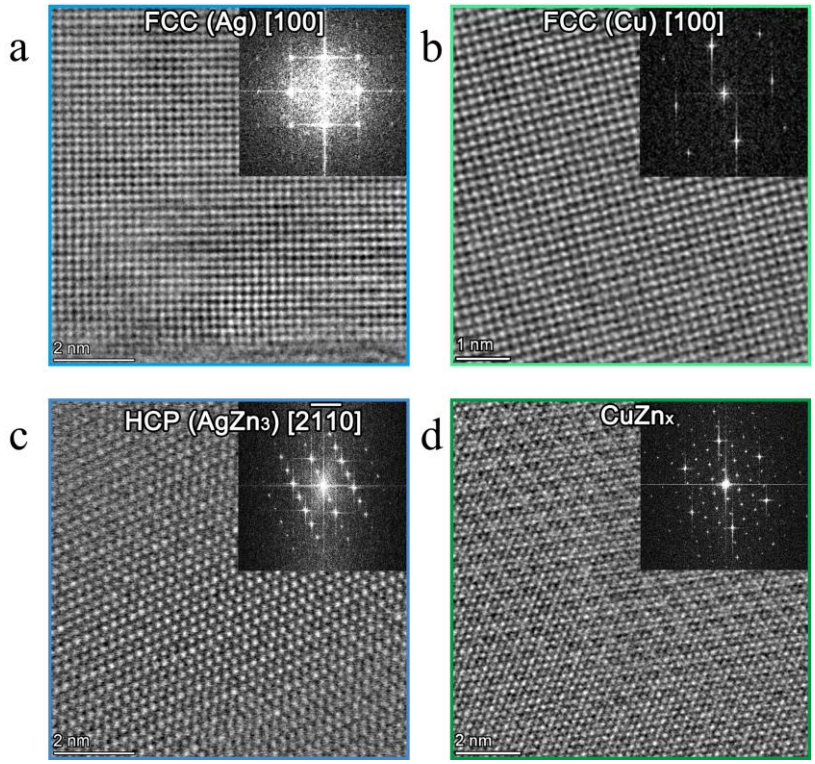

Figure 5.17 Atomic-level HAADF images of unalloyed (a) Ag and (b) Cu within the sample. The corresponding FFT images are shown in the upper right corner. The locations in Figure 5.16 are marked in light blue and light green, respectively. alloyed (c) $AgZn_3$ and (d) $CuZn_x$ within the sample. The corresponding FFT images are shown in the upper right corner. The locations in Figure 5.16 are marked in dark blue and dark green, respectively.

We propose that this unidentified alloy phase may play a crucial role in the remarkable improvement of electrochemical performance, particularly under high Zn utilization conditions. To elucidate its structural characteristics, we performed comprehensive characterization of this phase. Figure 5.18 exhibits the Electron Energy Loss Spectroscopy (EELS) spectra of the alloy phase, revealing no detectable absorption signals in the Ag and O regions, while distinct characteristic peaks for Cu and Zn are observed. This confirms that the phase consists exclusively of Cu and Zn elements. Subsequently, atomic-resolution imaging was conducted along different crystallographic axes (Figure 5.19a-c), enabling structural analysis at the atomic scale. Based on these observations, we reconstructed the three-dimensional atomic configuration of this phase (Figure 5.19d), which corresponds to a Cu_6Zn_{13} stoichiometry—

consistent with the EDS compositional analysis. The corresponding zone-axis diffraction patterns, presented in the lower-left insets of Figure 5.19a-c, demonstrate excellent agreement between the proposed structural model and experimental data, validating the accuracy of our structural determination.

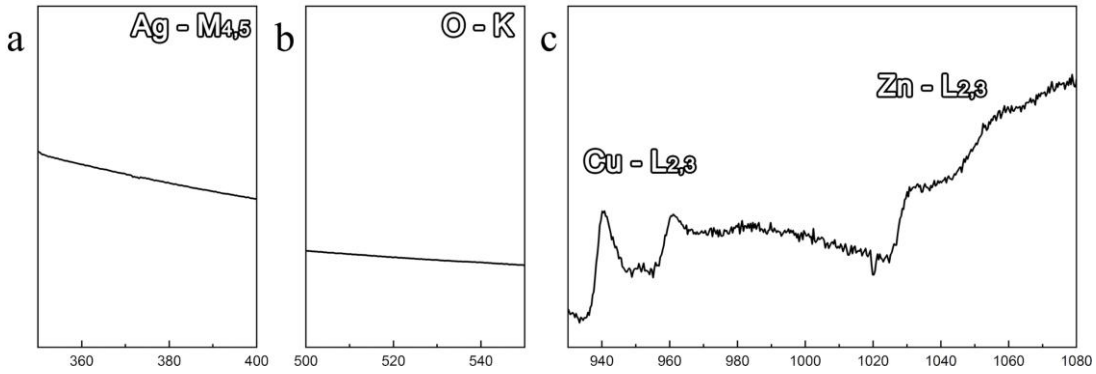

Figure 5.18 EELS energy spectra of the redeposited alloy phase at the characteristic peaks of (a) Ag, (b) O, and (c) Cu and Zn.

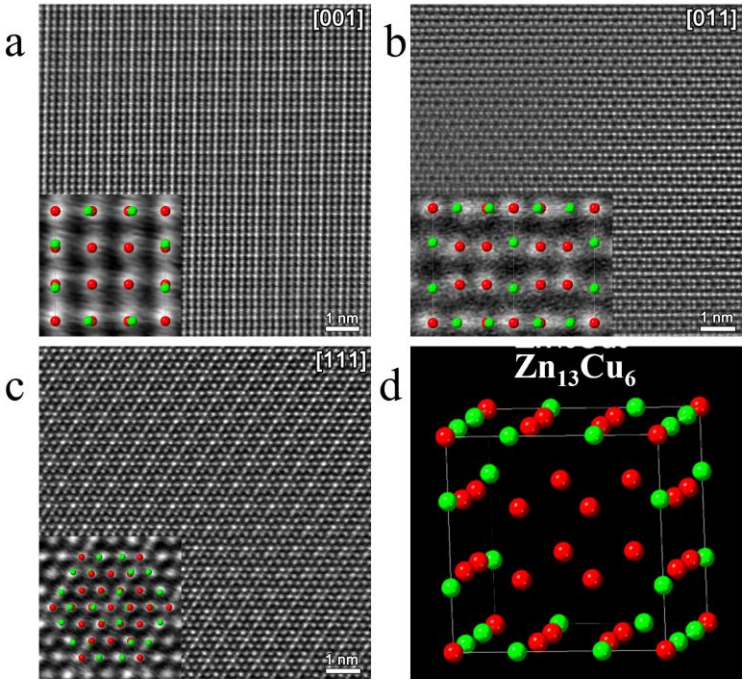

Figure 5.19 (a-c) Atomic-level HAADF images of the redeposited alloy phase along different axes, with theoretical atomic positions shown in the inset at the lower left corner. (d) Proposed three-dimensional structure of the redeposited alloy phase, with red spheres representing Zn atoms and green spheres representing Cu atoms. The estimated chemical formula for this structure is Cu_6Zn_{13}.

Comparative analysis reveals that the sample subjected to 50 cycles exhibits a more advanced

stage of alloying reaction compared to the pristine Cu/Ag@Zn-20 sample, as illustrated in Figure 5.20a-b. EDS compositional analysis demonstrates complete alloying of the copper layer, while maintaining the Cu_6Zn_{13} intermetallic phase structure. Furthermore, the silver layer has undergone near-complete alloying transformation while retaining its distinct layered alloy structure. Notably, residual metallic Ag persists even after extended cycling (Figure 5.20c), indicating that the alloying kinetics of the Cu layer proceed at a significantly faster rate compared to the Ag layer. This observation further reveals an interdependent alloying mechanism, where the ongoing transformation of the Ag layer continues to modulate the alloying dynamics of the adjacent Cu layer throughout the electrochemical cycling process. The differential alloying rates between these two metallic layers suggest a complex interfacial evolution process, where the relatively slower Ag alloying may serve to regulate and stabilize the more rapid Cu-Zn alloy formation, potentially contributing to the structural integrity of the composite electrode during prolonged operation. X-ray diffraction (XRD) characterization further elucidated the phase evolution of in situ formed Zn_xCu_y alloys during electrochemical cycling. The XRD patterns exhibited a distinctive peak at approximately 24.47°, unambiguously confirming the emergence of the $Zn_{13}Cu_6$ phase during cycling (Figure 5.21). This observation provides crystallographic evidence for the progressive alloying process, where the initially deposited Zn gradually reacts with the Cu substrate to form ordered intermetallic compounds.

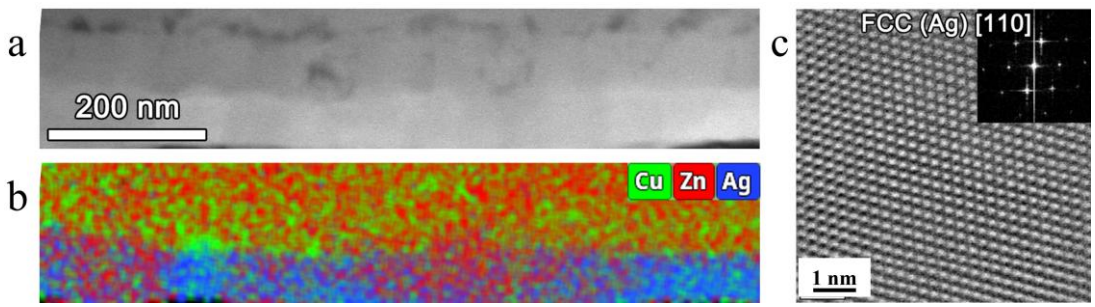

Figure 5.20 (a) HAADF-STEM image and the corresponding (b) XEDS image of the sample after 50 cycles. (c) Atomic-scale HAADF images of unalloyed Ag in the 50-cycle sample.

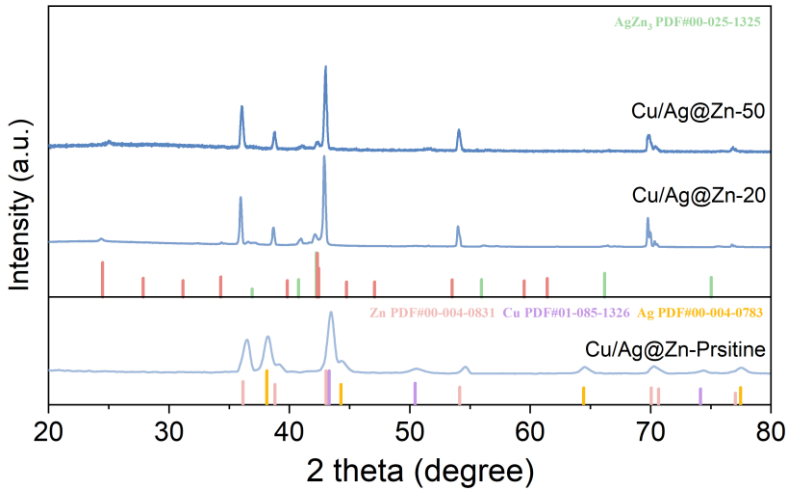

Figure 5.21 XRD patterns of Cu/Ag@Zn, Cu/Ag@Zn-20 and Cu/Ag@Zn-50 electrodes.

A critical examination of existing literature reveals that Cu-Zn alloying in conventional zinc batteries predominantly yields the $CuZn_5$ phase (Cu:Zn=1:5) with hexagonal close-packed (HCP) structure. However, our system featuring an interfacial Ag layer between Cu and Zn exclusively produces the cubic Cu_6Zn_{13} phase (Cu:Zn=1:2.17), representing a remarkable 50% reduction in Zn content. This striking deviation strongly suggests that the Ag interlayer plays a dual mechanistic role in phase formation kinetics. From a structural perspective, the Ag layer functions as: (1) an atomic sieve that modulates interfacial reactions by restricting direct Cu-Zn contact and reducing Zn^{2+} flux; and (2) a face-centered cubic (FCC) template (either as pristine Ag or the reaction-retarded Cu layer) that thermodynamically favors cubic phase nucleation in the redeposited layer. Furthermore, the $AgZn_3$ alloy formed during cycling exhibits lattice parameters that are intermediate between the Zn substrate and the (111) plane of the cubic Cu_6Zn_{13} phase (Figure 5.22). This lattice matching creates an effective bridging effect across interfaces, significantly enhancing structural coherence while suppressing delamination. Concurrent microhardness measurements of the in situ formed interface revealed a progressive increase from 47.6 HV for the pristine Cu/Ag@Zn electrode to 85 HV after 50 cycles (Figure 5.23). This substantial enhancement in interfacial hardness significantly contributes to maintaining the structural integrity of the Cu/Ag@Zn electrode during prolonged

cycling.

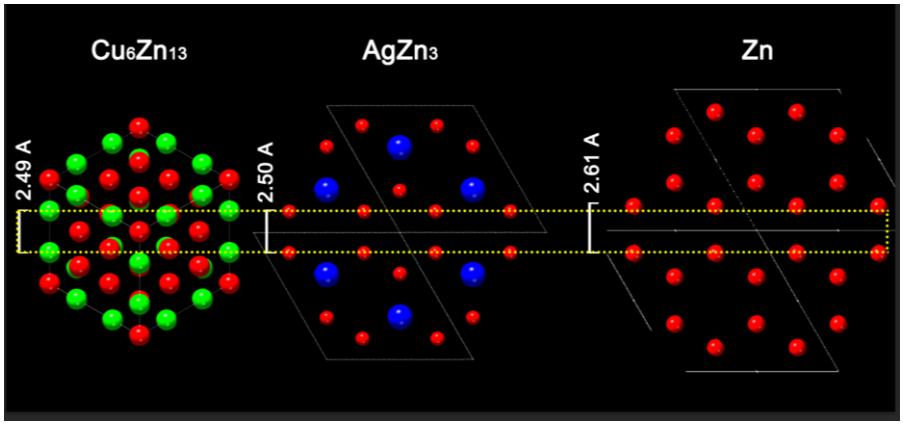

Figure 5.22 Schematic diagrams of the (111) plane of the redeposited alloy phase, the (0001) plane of $AgZn_3$, and the (0001) plane of Zn, from left to right. The atomic spacing increases progressively from left to right.

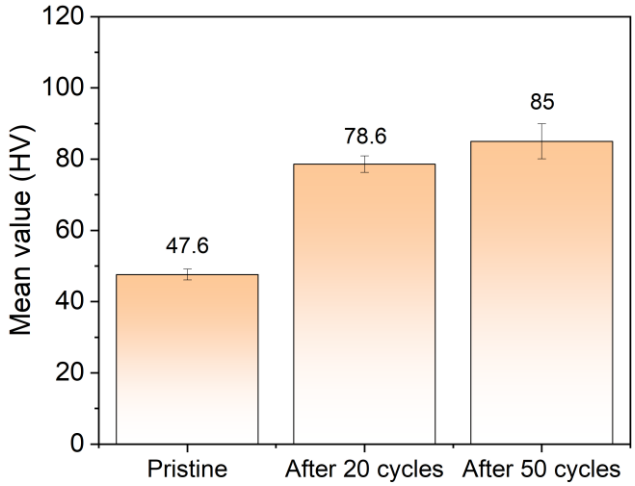

Figure 5.23 Microhardness of the Cu/Ag@Zn after different cycle numbers. (Vickers hardness tests were carried out under a 10 g load for 10 seconds using a Struers Duramin-40.)

The transport kinetics of ions and electrons at the anode-electrolyte interface critically governs the polarization behavior and reversibility of Zn plating/stripping processes[213]. To systematically investigate the influence of the metal interphase on interfacial transport dynamics, we employed in situ electrochemical impedance spectroscopy (EIS) during Zn deposition. Nyquist plots of cycled Cu/Ag@Zn electrodes (Figure 5.24) exhibited characteristic features consisting of a high-frequency semicircle followed by a low-frequency tail[214]. This impedance response was quantitatively analyzed using an equivalent circuit model

incorporating charge transfer resistance (R_{ct}) and Warburg diffusion elements. The R_{ct} values, directly proportional to the semicircle diameter, serve as a quantitative measure of charge transfer difficulty at the interface. Notably, the R_{ct} values demonstrated a significant reduction after the initial cycle and subsequently stabilized over eight cycles, suggesting an activation process accompanied by progressive interfacial phase transformations. The interfacial kinetics were further quantified through the exchange current density (j_0), calculated from EIS data using the relation $j_0 = RT/(zFSRct)$, where R, T, z, F, and S represent the universal gas constant, absolute temperature, Zn^{2+} valence state, Faraday constant, and electrode surface area, respectively[190]. The Cu/Ag@Zn electrode exhibited a remarkable enhancement in j_0 from 0.068 to 0.094 mA cm^{-2} over 35 cycles, approximately three times higher than bare Zn electrodes (Figure 5.24b and d). This substantial improvement in exchange current density, coupled with reduced charge transfer resistance, indicates significantly facilitated Zn^{2+} transport through the alloyed interphase layer. In stark contrast, unmodified cells displayed progressively increasing transport impedance with cycling, attributable to dendritic Zn growth and passivating byproduct formation that severely compromise interfacial charge transfer. Notably, the abrupt R_{ct} reduction observed in bare Zn cells after 21 cycles typically indicates soft short-circuit formation in symmetric cell configurations[215], which also accounts for the anomalous j_0 increase. Further supporting evidence for the superior interfacial kinetics comes from activation energy analysis (Figure 5.25), where the Cu/Ag@Zn system demonstrated a substantially lower E_a (24.86 kJ mol^{-1}) compared to bare Zn (30.18 kJ mol^{-1}). These comprehensive electrochemical characterizations collectively demonstrate that the engineered interphase effectively optimizes charge transfer kinetics while suppressing detrimental interfacial degradation mechanisms.

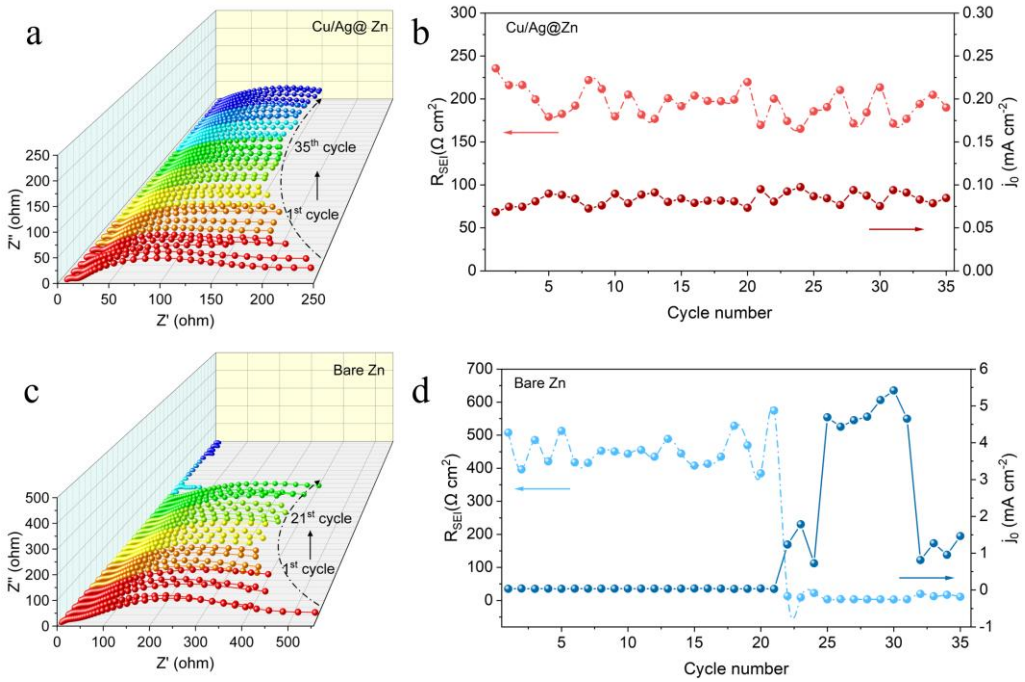

Figure 5.24 In situ electrochemical impedance spectroscopy (EIS) was adopted to investigate the transport kinetics for (a) Cu/Ag@Zn and (c) bare Zn symmetric cells. The R_{SEI} and j_0 for (b) Cu/Ag@Zn and (d) bare Zn electrodes derived from (a, c).

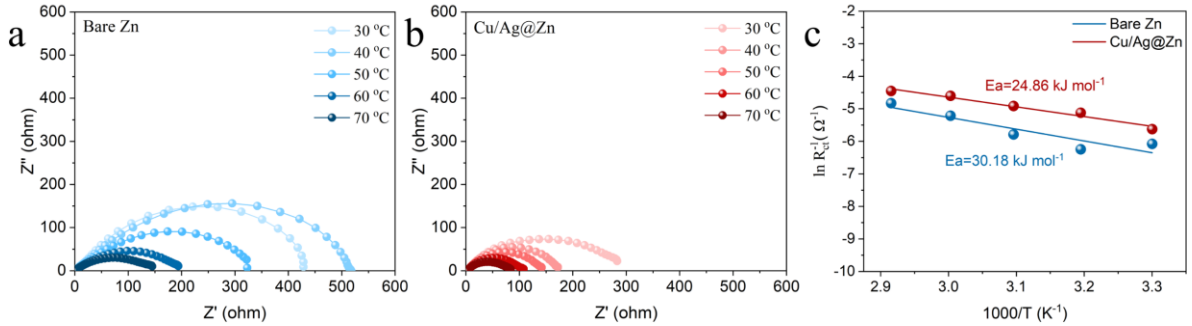

Figure 5.25 Temperature-dependent Nyquist plots of (a) bare Zn and (b) Cu/Ag@Zn symmetric cells and (c) corresponding activation energy.

5.2.4 Electrochemical Performance in Practical Evaluation

In practical zinc-based battery systems, the depth of discharge (DOD, or zinc utilization rate) serves as a critical determinant of both cycle longevity and energy density metrics in aqueous zinc-metal batteries (AZMBs). Conventional Zn anodes in reported systems typically employ thick metal foils (100 μm, 45.96 mAh cm^{-2}) operated at ultralow DODs (<5%)[154], which severely compromises their specific/volumetric energy density for commercial

implementation. This limitation originates from the hostless nature of Zn metal that undergoes heterogeneous stripping dynamics and irreversible structural degradation when subjected to deep cycling (DOD>50%). To rigorously assess the technological viability of our Cu/Ag@Zn architecture, we systematically evaluated its plating/stripping behavior under progressively intensified DOD conditions (20-95%). At moderate current density/capacity combinations of 0.92 mA cm^{-2}/0.92 mAh cm^{-2} (DOD=20% for 10 μm-thick Zn), the Cu/Ag@Zn configuration demonstrated exceptional cycling stability exceeding 1800 h (Figure 5.26b). In stark contrast, bare Zn counterparts exhibited premature failure within 400 h respectively, accompanied by marked voltage fluctuations (Figure 5.26a). Under extreme DOD conditions (90%, 4.39 mA cm^{-2}/4.39 mAh cm^{-2}), the bare Zn anode catastrophically failed within 60 h due to dendritic-induced short circuits and erratic voltage spikes (Figure 5.26c), whereas the Cu/Ag@Zn electrode maintained stable operation for 800 h with minimal polarization (70 mV, Figure 5.26d). Importantly, comparative analysis with state-of-the-art high DOD Zn anodes reveals our Cu/Ag@Zn system achieves unprecedented DOD-capacity synergy, delivering over 400 cycles at the highest reported utilization rate (Figure 5.27)[142, 201, 216-223].

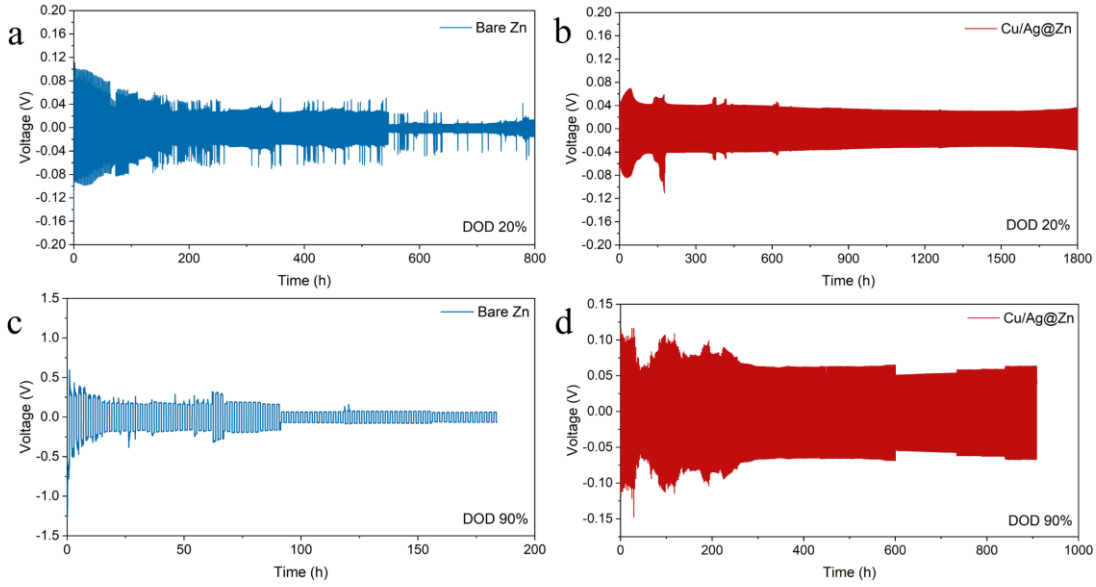

Figure 5.26 Cycling performance of (a, c) bare Zn//Cu@Zn and (b, d) Cu/Ag@Zn//Zn symmetric cells at DODs of 20 % and 90 %.

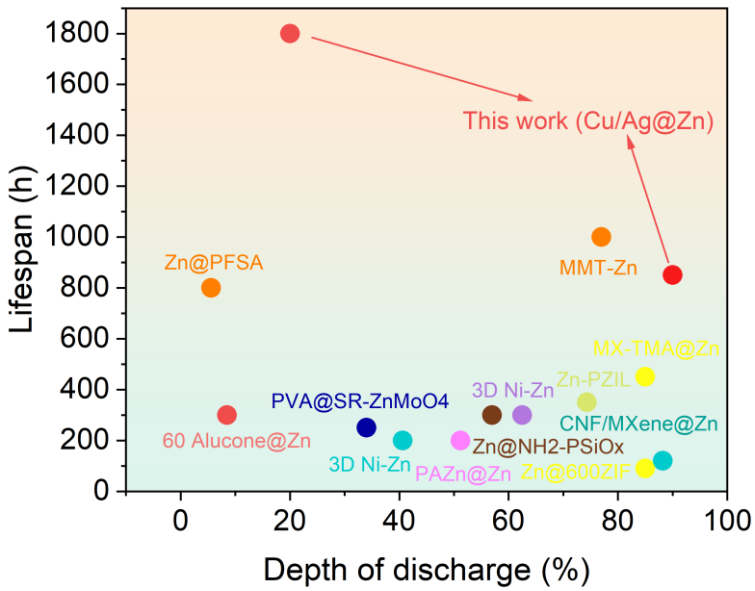

Figure 5.27 Comparison of depth of discharge and cycling life of Cu/Ag@Zn electrode with representative peer Zn anodes.

To assess the practical viability of Cu/Ag@Zn anodes in operational battery systems, we constructed full cells with VO_2 nanorod cathodes (hydrothermally synthesized, morphology verified by SEM/XRD in Figure 5.28) in 2 M $ZnSO_4$ electrolyte. Comparative electrochemical analysis between Cu/Ag@Zn||VO_2 and bare Zn||VO_2 configurations revealed fundamental performance differences. Cyclic voltammetry of Cu/Ag@Zn||VO_2 cells exhibited three distinct redox couples at 1.01/0.84, 0.74/0.48, and 0.65/0.41 V vs. Zn/Zn^{2+} (Figure 5.29a), corresponding to reversible Zn^{2+} intercalation/deintercalation in the VO_2 lattice. While Zn||VO_2 cells displayed analogous peak positions, their initial current densities were consistently lower than Cu/Ag@Zn counterparts (Figure 5.29a), indicative of enhanced interfacial charge transfer kinetics in the modified anode. This observation aligns with electrochemical impedance spectroscopy results demonstrating a markedly reduced charge transfer resistance (Rct = 245 Ω) for Cu/Ag@Zn||VO_2 versus 460 Ω for bare Zn systems (Figure 5.29b), attributable to optimized Zn^{2+} diffusion pathways and interfacial conductivity.

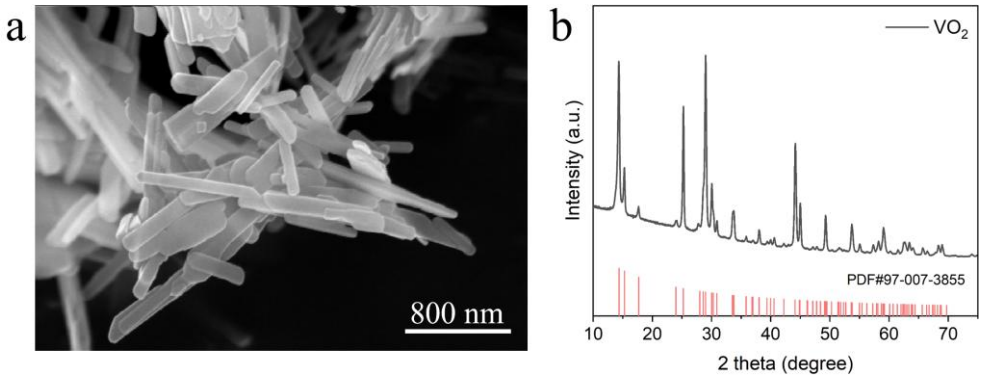

Figure 5.28 (a) SEM image of VO_2 nanorods and (b) XRD patterns of the VO_2 cathode material.

Rate capability evaluation across 0.1-2.0 A g^{-1} current densities showed systematic performance advantages (Figure 5.29d). At 1.0 A g^{-1}, Cu/Ag@Zn||VO_2 delivered 167 mAh g^{-1} versus 147 mAh g^{-1} for bare Zn||VO_2 (Figure 5.29c), a disparity amplified at higher rates due to accelerated Zn dissolution/deposition kinetics and reduced interfacial impedance in Cu/Ag@Zn anodes. Long-term cycling at 1.0 A g^{-1} demonstrated exceptional stability for Cu/Ag@Zn||VO_2 (≈79.4% capacity retention after 1500 cycles, initial capacity ≈232.80 mAh g^{-1}), outperforming the 16% capacity decay observed in bare Zn||VO_2 controls (Figure 5.30a). Under extreme 2 A g^{-1} conditions, Cu/Ag@Zn||VO_2 maintained 84.3% capacity retention (167.70 → 141.37 mAh g^{-1}) over 1000 cycles without short-circuiting (Figure 5.30b), contrasting with bare Zn||VO_2 44.7% decay and voltage instability from cycle 1000 onward.

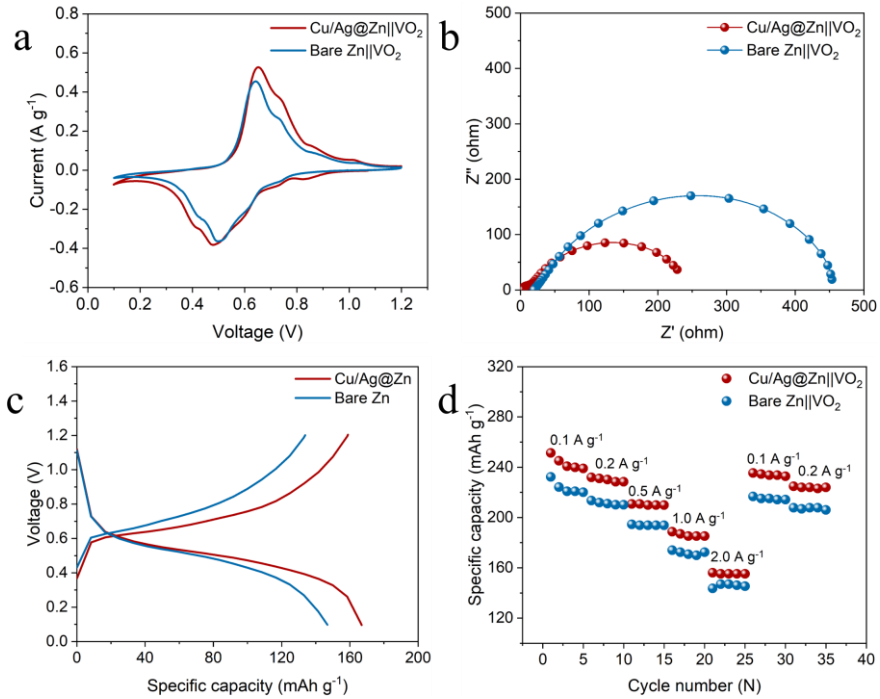

Figure 5.29 (a) CV curves of bare Zn||VO_2 and Cu/Ag@Zn||VO_2. (b) Electrochemical impedance spectroscopy (EIS) of full cells. (c) galvanostatic charge/discharge profiles of bare Zn||VO_2 and Cu/Ag@Zn||VO_2 at 1.0 A g^{-1}. (d) Rate performance of full cells.

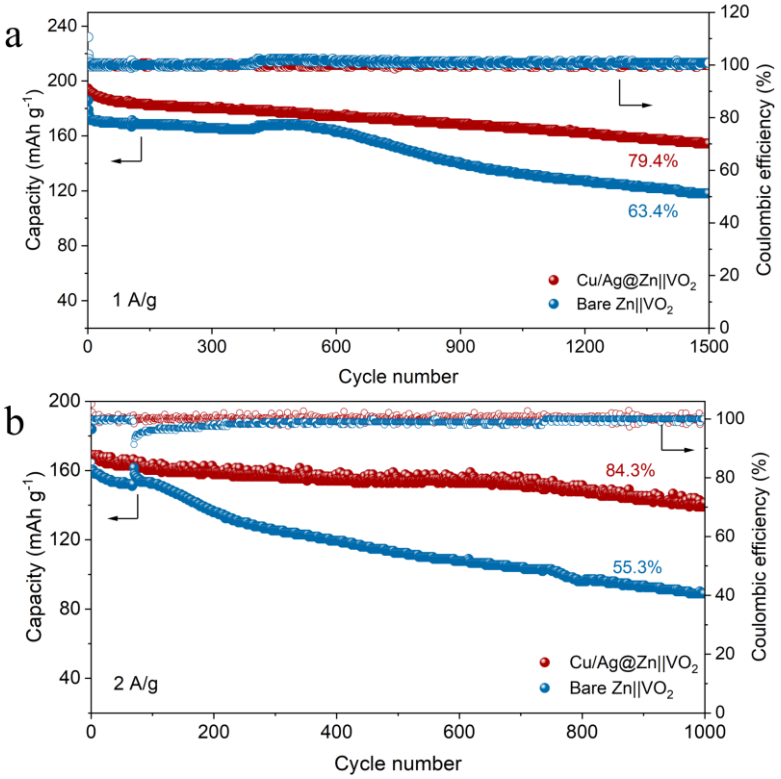

Figure 5.30 Long-term cycling performance of bare Zn||VO_2 and Cu/Ag@Zn||VO_2 at (a) 1.0 A g^{-1} and (b) 2.0 A g^{-1}.

5.3 Conclusion

In this work, we present an innovative bilayer metallic interface architecture that synergistically combines stress buffering functionality with dual advantages in regulating uniform zinc ion deposition. During electrochemical cycling, the electrode surface undergoes structural evolution to form a Cu_6Zn_{13} alloy with hollow architecture - a phenomenon distinct from conventional single-layer buffer systems. This unique behavior originates from the ultrathin atomic-sieving effect enabled by the engineered Ag interlayer. The dual protection mechanism (combining mechanical buffering and ion flux regulation) enables exceptional zinc anode stability even under extreme operational conditions. The optimized Cu/Ag@Zn anode demonstrates remarkable cyclability with ultra-long lifespans exceeding 5500 hours at 5 mA cm^{-2} and maintains 500 cycles at 95% depth of discharge. Practical viability is further demonstrated in full-cell configurations (paired with VO_2 cathodes), achieving 84.3% capacity retention after 1000 cycles. The synergistic effects of these mechanisms - kinetic control of alloying reactions, thermodynamic stabilization of cubic phases, and improved interfacial adhesion - collectively contribute to the exceptional structural stability observed in our battery system. This represents a significant advancement over conventional Cu-Zn alloy systems, demonstrating how interfacial engineering can fundamentally alter phase evolution pathways in metal battery electrodes.

Chapter 6 Conclusion and Perspectives

6.1 Conclusion

Owing to inherent safety profile and practical feasibility, aqueous zinc-ion batteries (AZIBs) have garnered significant attention for large-scale energy storage applications. Zinc metal, serving as a key component of AZIBs, has been widely adopted as an anode material due to its multifaceted advantages. The fundamental operational mechanism of zinc anodes primarily relies on the electrochemical redox reactions between metallic Zn and Zn^{2+} ions. Thus the reversibility of zinc plating/stripping processes becomes crucial for achieving long-term cycling stability. However, the development of AZIBs has been substantially hindered by several inherent limitations, including poor anode reversibility and low zinc utilization efficiency, predominantly arising from zinc dendrite formation and parasitic side reactions. To address these challenges, this thesis implements a series of engineered interfacial layers on the zinc anode surface, which effectively suppress detrimental side reactions while enhancing overall battery performance. The principal findings of each investigation are summarized as follows:

(1) We build a multifunctional integrated interface layer consisting of MPP on the surface of the Zn anode. Arising from its abundant functional moieties and porous architecture, the MPP layer exhibits substantial binding energy for water molecule coordination, facilitating three synergistic effects: chemical confinement of solvated species, spatial redistribution of ionic flux, and efficient desolvation of Zn^{2+}. These integrated mechanisms collectively shield the reactive Zn metal from electrochemical degradation by aqueous electrolytes, thereby significantly mitigating parasitic reaction pathways. Furthermore, the MPP interphase simultaneously modulates interfacial polarization through electric field passivation and homogenization, enabling topographically controlled Zn^{2+} deposition that

yields dendrite-free MPP-Zn electrodes. The demonstrated multifunctional interphase design framework provides a universal blueprint for zinc anode optimization, offering critical insights that accelerate the realization of durable multivalent metal battery technologies through synergistic interfacial control mechanisms.

(2) We introduces a novel interfacial screening mechanism inspired by the Sabatier principle to engineer bifunctional zinc anodes operating at 80% depth of discharge (DOD). The designed interface synergistically combines stress buffering capabilities for uniform stripping with secondary current collection functionality for regulated plating. Drawing conceptual parallels to catalytic adsorption-energy optimization, our analysis reveals that optimized transition metal-zinc (TM-Zn) binding energetics critically govern anode stripping homogeneity. Concurrently, the engineered zincophilic interface with submicron topography mediates dendrite-suppressed metal deposition through spatial charge redistribution. Drawing an analogy to the Sabatier principle for chemical catalysis, we find that a moderate TM-Zn interaction strength can favor the uniform stripping of Zn anodes. Atomic observations demonstrate a gradual phase evolution of Cu to $CuZn_x$ and $CuZn_5$ alloys. These phases exhibit high electronic conductivity, zincophilicity, and remarkable mechanical robustness, which collectively inhibit Zn dendrite growth during plating and suppress the pits during stripping. The like Sabatier principle is expected to guide the selection of TM interlayer for (electro)chemically stable metal anodes in rechargeable batteries.

(3) Building upon our second work, we aim to achieve high-utilization zinc batteries under extreme operational conditions through the development of an innovative bilayer metallic interface architecture. We present an innovative bilayer metallic interface architecture that synergistically combines stress buffering functionality with dual advantages in regulating uniform zinc ion deposition. During electrochemical cycling, the electrode surface

undergoes structural evolution to form a Cu_6Zn_{13} alloy with hollow architecture - a phenomenon distinct from conventional single-layer buffer systems. This unique behavior originates from the ultrathin atomic-sieving effect enabled by the engineered Ag interlayer. The dual-functional protection system, integrating strain-adaptive mechanical buffering with spatially regulated Zn^{2+} flux distribution, achieves unprecedented anode stability under harsh operating conditions (DOD=90%). The synergistic effects of these mechanisms - kinetic control of alloying reactions, thermodynamic stabilization of cubic phases, and improved interfacial adhesion - collectively contribute to the exceptional structural stability observed in our battery system. This represents a significant advancement over conventional Cu-Zn alloy systems, demonstrating how interfacial engineering can fundamentally alter phase evolution pathways in metal battery electrodes.

6.2 Perspectives

Current research on zinc anodes remains predominantly focused on enhancing electrochemical performance, while investigations into the failure mechanisms triggering performance degradation remain in their nascent stages. This has led to many studies essentially yielding significantly less efficient outcomes. During cycling, zinc metal anodes involve intricate mass transport/diffusion and electrochemical reactions: the former encompasses diffusion, adsorption, desolvation, and atomic rearrangement at the zinc-ion interface, while the latter concerns electron transport and exchange at interfaces involving zinc ions, water molecules, or protons. Specifically, the diffusion, adsorption, desolvation of zinc ions, and electron transfer between zinc ions and the electrode directly govern zinc deposition/stripping behavior and side reactions at the interface. These processes are neither instantaneous nor isolated—they unfold as complex, interrelated, transient phenomena that may proceed competitively:

(I): The dynamic interfacial evolution mechanism remains unclear. The chemical/structural evolution of interfacial layers during charge/discharge (e.g., alloying, phase separation) lacks

in situ characterization methods, resulting in a design process devoid of theoretical guidance. We can employ *liquid-phase in situ TEM* to dynamically observe in real-time the spontaneous formation process of the SEI at the Zn/electrolyte interface in aqueous electrolytes, revealing the correlation between its compositional distribution and structural stability. Furthermore, understanding the hydrogen evolution reaction (HER) at the interface is *paramount* for regulating the electrochemical behavior of zinc-aqueous batteries. However, the mechanism underlying HER's relationship with solvation chemistry, particularly the time-resolved dynamics of hydrogen bonding networks under electric fields—remains unclear. While numerous studies have exhaustively elucidated solvation structures in bulk electrolytes, a substantial knowledge gap persists regarding the dynamic evolution of these structures, especially concerning hydrogen bonding reconfiguration at electrode/electrolyte interfaces. To bridge this gap, we propose utilizing *electrochemical in situ FTIR* spectroscopy to uncover ion desolvation/solvent dissociation processes occurring at the interface.

(II): A critical limitation persists in current zinc battery research: the predominant reliance on coin cell platforms fails to emulate practical operating parameters. This methodological gap necessitates transitioning to industrial-relevant pouch cell configurations. Such systems enable comprehensive analysis of cumulative parasitic effects (e.g. H_2 evolution, ZnO passivation) under multi-physics coupled conditions, thereby informing the design of interface-specific suppression protocols for scalable aqueous battery development.

(III): Significant progress has been made in enhancing zinc anode performance through interface engineering strategies. However, substantial opportunities remain for improving zinc utilization efficiency. Current interface design strategies offer limited enhancement to anode material properties, necessitating a holistic approach that synergistically integrates zinc anode structural design, electrolyte optimization, and separator modification to achieve comprehensive battery performance improvements.

References

[1] D. Selvakumaran, A. Pan, S. Liang, G. Cao. *J. Mater. Chem. A,* **2019**, 7, 18209-18236.

[2] L. Tang, H. Peng, J. Kang, H. Chen, M. Zhang, Y. Liu, D. H. Kim, Y. Liu, Z. Lin. *Chemical Society Reviews,* **2024**, 53, 4877-4925.

[3] T.-Z. Ang, M. Salem, M. Kamarol, H. S. Das, M. A. Nazari, N. Prabaharan. *Energy strategy reviews,* **2022**, 43, 100939.

[4] F. Creutzig, P. Agoston, J. C. Goldschmidt, G. Luderer, G. Nemet, R. C. Pietzcker. *Nature Energy,* **2017**, 2, 1-9.

[5] E. Romero, V. I. Novoderezhkin, R. van Grondelle. *Nature,* **2017**, 543, 355-365.

[6] F. Díaz-González, A. Sumper, O. Gomis-Bellmunt, R. Villafáfila-Robles. *Renew Sust Energ Rev.,* **2012**, 16, 2154-2171.

[7] K. Kang, Y. S. Meng, J. Breger, C. P. Grey, G. Ceder. *Science,* **2006**, 311, 977-980.

[8] C. Xu, Q. Dai, L. Gaines, M. Hu, A. Tukker, B. Steubing. *Commun. Mater. ,* **2020**, 1, 99.

[9] H. Wu, D. Zhuo, D. Kong, Y. Cui. *Nat. Commun.,* **2014**, 5, 5193.

[10] J. C. Pramudita, D. Sehrawat, D. Goonetilleke, N. Sharma. *Adv. Energy Mater.,* **2017**, 7, 1602911.

[11] J. Ni, S. Fu, C. Wu, J. Maier, Y. Yu, L. Li. *Adv. Mater.,* **2016**, 28, 2259-2265.

[12] S. Chen, C. Wu, L. Shen, C. Zhu, Y. Huang, K. Xi, J. Maier, Y. Yu. *Adv. Mater.,* **2017**, 29, 1700431.

[13] Y. Wang, J. Yi, Y. Xia. *Adv. Energy Mater.,* **2012**, 2, 830-840.

[14] M. Winter, R. J. Brodd. *Chem. Rev.,* **2004**, 104, 4245-4270.

[15] D. Chao, W. Zhou, F. Xie, C. Ye, H. Li, M. Jaroniec, S.-Z. Qiao. *Sci. Adv.,* **2020**, 6,

eaba4098.

[16] P. Kurzweil. *J. Power Sources,* **2010**, 195, 4424-4434.

[17] G. J. May, A. Davidson, B. Monahov. *J. Energy Storage,* **2018**, 15, 145-157.

[18] A. von Wald Cresce, K. Xu. *Carbon Energy,* **2021**, 3, 721-751.

[19] J. B. Goodenough, Y. Kim. *Chem. Mater.,* **2010**, 22, 587-603.

[20] W. Zhang, J. Yin, W. Wang, Z. Bayhan, H. N. Alshareef. *Nano Energy,* **2021**, 83, 105792.

[21] Y. Li, X. Zhao, Y. F. Gao, Y. C. Ding, Z. C. Si, L. B. Dong, D. Zhou, F. Y. Kang. *Sci. China-Chem.,* **2024**, 67, 165-190.

[22] X. Zhao, X. Liang, Y. Li, Q. Chen, M. Chen. *Energy Storage Mater.,* **2021**, 42, 533-569.

[23] M. Piccolino. *Trends in neurosciences,* **2000**, 23, 147-151.

[24] A. R. Mainar, L. C. Colmenares, J. A. Blázquez, I. Urdampilleta. *Int. J. Energy Res.,* **2018**, 42, 903-918.

[25] N. Zhang, F. Cheng, J. Liu, L. Wang, X. Long, X. Liu, F. Li, J. Chen. *Nat. Commun.,* **2017**, 8, 405.

[26] T. Yamamoto, T. Shoji. *Inorg Chim Acta,* **1986**, 117, L27-L28.

[27] C. J. Xu, B. H. Li, H. D. Du, F. Y. Kang. *Angew. Chem. Int. Ed.,* **2012**, 51, 933-935.

[28] C. Xu, B. Li, H. Du, F. Kang. *Angew. Chem. Int. Ed.,* **2012**, 124, 957-959.

[29] B. Li, X. T. Zhang, T. L. Wang, Z. X. He, B. A. Lu, S. Q. Liang, J. Zhou. *Nano-micro Lett. ,* **2022**, 14, 1-31.

[30] H. Jia, Z. Wang, B. Tawiah, Y. Wang, C.-Y. Chan, B. Fei, F. Pan. *Nano Energy,* **2020**, 70, 104523.

[31] X. Chen, S. Li, K. Wang, H. Zhao, G. He, Y. Bai. *Energy Storage Mater.,* **2024**, 73, 103869.

[32] X. Chen, B. Liu, C. Zhong, Z. Liu, J. Liu, L. Ma, Y. Deng, X. Han, T. Wu, W. Hu. *Adv. Energy Mater.,* **2017**, 7, 1700779.

[33] W. Zhou, M. Chen, Q. Tian, J. Chen, X. Xu, C.-P. Wong. *Energy Storage Mater. ,* **2022**, 44, 57-65.

[34] X. Guo, S. Zhang, H. Hong, S. Wang, J. Zhu, C. Zhi. *iScience,* **2025**, 28, 111751.

[35] J. Lee, J. B. Ju, W. I. Cho, B. W. Cho, S. H. Oh. *Electrochim. Acta,* **2013**, 112, 138-143.

[36] J. Yang, B. Yin, Y. Sun, H. Pan, W. Sun, B. Jia, S. Zhang, T. Ma. *Nano-Micro Lett.,* **2022**, 14, 1-47.

[37] M. S. Chae, J. W. Heo, S. C. Lim, S. T. Hong. *Inorg. Chem.,* **2016**, 55, 3294-3301.

[38] Y. W. Cheng, L. L. Luo, L. Zhong, J. Z. Chen, B. Li, W. Wang, S. X. Mao, C. M. Wang, V. L. Sprenkle, G. S. Li, J. Liu. *ACS Appl. Mater. Interfaces,* **2016**, 8, 13673-13677.

[39] W. Li, K. Wang, S. Cheng, K. Jiang. *Adv. Energy Mater.,* **2019**, 9, 1900993.

[40] G. Li, L. Sun, S. Zhang, C. Zhang, H. Jin, K. Davey, G. Liang, S. Liu, J. Mao, Z. Guo. *Adv. Funct. Mater.,* **2024**, 34, 2301291.

[41] T. T. Wang, C. P. Li, X. S. Xie, B. G. Lu, Z. X. He, S. Q. Liang, J. Zhou. *ACS Nano,* **2020**, 14, 16321-16347.

[42] A. Naveed, H. Yang, Y. Shao, J. Yang, N. Yanna, J. Liu, S. Shi, L. Zhang, A. Ye, B. He. *Adv. Mater.,* **2019**, 31, 1900668.

[43] Z. Yi, G. Chen, F. Hou, L. Wang, J. Liang. *Adv. Energy Mater.,* **2021**, 11, 2003065.

[44] H. Dai, T. Sun, J. Zhou, J. Wang, Z. Chen, G. Zhang, S. Sun. *Nat. Commun.,* **2024**, 15, 8577.

[45] H. Wang, H. Li, Y. Tang, Z. Xu, K. Wang, Q. Li, B. He, Y. Liu, M. Ge, S. Chen. *Adv. Funct.*

Mater., **2022**, 32, 2207898.

[46] Y. Zhang, X. Zheng, N. Wang, W.-H. Lai, Y. Liu, S.-L. Chou, H.-K. Liu, S.-X. Dou, Y.-X. Wang. *Chem. Sci. ,* **2022**, 13, 14246-14263.

[47] Q. Yang, G. Liang, Y. Guo, Z. Liu, B. Yan, D. Wang, Z. Huang, X. Li, J. Fan, C. Zhi. *Adv. Mater.,* **2019**, 31, 1903778.

[48] D. H. Wang, Q. Li, Y. W. Zhao, H. Hong, H. F. Li, Z. D. Huang, G. J. Liang, Q. Yang, C. Y. Zhi. *Adv. Energy Mater.,* **2022**, 12, 2102707.

[49] X. B. Cheng, R. Zhang, C. Z. Zhao, Q. Zhang. *Chem. Rev.,* **2017**, 117, 10403-10473.

[50] Q. Yang, G. J. Bang, Y. Guo, Z. X. Liu, B. X. Yon, D. H. Wang, Z. D. Huang, X. L. Li, J. Fan, C. Y. Zhi. *Adv. Mater.,* **2019**, 31, 1903778.

[51] A. Bayaguud, Y. Fu, C. Zhu. *J. Energ. Chem.,* **2022**, 64, 246-262.

[52] J. Hao, X. Li, S. Zhang, F. Yang, X. Zeng, S. Zhang, G. Bo, C. Wang, Z. Guo. *Adv. Funct. Mater.,* **2020**, 30, 2001263.

[53] M. Zhu, J. Hu, Q. Lu, H. Dong, D. D. Karnaushenko, C. Becker, D. Karnaushenko, Y. Li, H. Tang, Z. Qu. *Adv. Mater.,* **2021**, 33, 2007497.

[54] X. Guo, Z. Zhang, J. Li, N. Luo, G.-L. Chai, T. S. Miller, F. Lai, P. Shearing, D. J. Brett, D. Han. *ACS Energy Lett.,* **2021**, 6, 395-403.

[55] Z. Cai, Y. T. Ou, B. Zhang, J. D. Wang, L. Fu, M. T. Wan, G. C. Li, W. Y. Wang, L. Wang, J. J. Jiang, Z. W. Seh, E. Y. Hu, X. Q. Yang, Y. Cui, Y. M. Sun. *J Am Chem Soc.,* **2021**, 143, 3143-3152.

[56] J. P. Chen, W. Y. Zhao, J. M. Jiang, X. L. Zhao, S. H. Zheng, Z. H. Pan, X. W. Yang. *Energy Storage Mater.,* **2023**, 59, 102767.

[57] J. Zhu, L. S. Hu, P. X. Zhao, L. Y. S. Lee, K. Y. Wong. *Chem. Rev.,* **2020**, 120, 851-918.

[58] J. M. Wei, M. Zhou, A. C. Long, Y. M. Xue, H. B. Liao, C. Wei, Z. C. J. Xu. *Nano-Micro Lett.,* **2018**, 10, 1-15.

[59] L. Y. Liu, Z. W. Hu, X. Wang, X. Y. Wang, Q. Q. Zheng, C. Han, X. Xu, H. K. Liu, S. X. Dou, W. J. Li. *J. Mater. Chem. A,* **2024**, 12, 28658-28681.

[60] A. Clarisza, H. K. Bezabh, S. K. Jiang, C. J. Huang, B. W. Olbasa, S. H. Wu, W. N. Su, B. J. Hwang. *ACS Appl. Mater. Interfaces,* **2022**, 14, 36644-36655.

[61] Q. S. Nian, W. D. Zhu, S. B. Zheng, S. Q. Chen, B. Q. Xiong, Z. H. Wang, X. J. Wu, Z. L. Tao, X. D. Ren. *ACS Appl. Mater. Interfaces,* **2021**, 13, 51048-51056.

[62] M. Kumar, T. C. Nagaiah. *Energy Storage Mater.,* **2022**, 49, 390-400.

[63] L. Chen, J. X. Zhang, Q. Li, J. Vatamanu, X. Ji, T. P. Pollard, C. Y. Cui, S. Hou, J. Chen, C. Y. Yang, L. Ma, M. S. Ding, M. Garaga, S. Greenbaum, H. S. Lee, O. Borodin, K. Xu, C. S. Wang. *ACS Energy Lett.,* **2020**, 5, 968-974.

[64] F. Wang, O. Borodin, T. Gao, X. L. Fan, W. Sun, F. D. Han, A. Faraone, J. A. Dura, K. Xu, C. S. Wang. *Nat. Mater.,* **2018**, 17, 543-549.

[65] C. Zhang, J. Holoubek, X. Y. Wu, A. Daniyar, L. D. Zhu, C. Chen, D. P. Leonard, I. A. Rodríguez-Pérez, J. X. Jiang, C. Fang, X. Ji. *Chem. Commun.,* **2018**, 54, 14097-14099.

[66] D. Kundu, S. H. Vajargah, L. W. Wan, B. Adams, D. Prendergast, L. F. Nazar. *Energy Environ. Sci.,* **2018**, 11, 881-892.

[67] X. S. Xie, S. Q. Liang, J. W. Gao, S. Guo, J. B. Guo, C. Wang, G. Y. Xu, X. W. Wu, G. Chen, J. Zhou. *Energy Environ. Sci.,* **2020**, 13, 503-510.

[68] Z. M. Zhao, J. W. Zhao, Z. L. Hu, J. D. Li, J. J. Li, Y. J. Zhang, C. Wang, G. L. Cui. *Energy*

Environ. Sci., **2019**, 12, 1938-1949.

[69] X. Q. Zhu, Z. M. Xu, T. Zhang, J. Zhang, Y. F. Guo, M. H. Shan, K. H. Wang, T. N. Shi, G. S. Cui, F. Wang, G. Y. Xu, M. F. Zhu. *Adv. Funct. Mater.,* **2024**, 34, 2407262.

[70] A. L. Xia, X. M. Pu, Y. Y. Tao, H. M. Liu, Y. G. Wang. *Appl. Surf. Sci.,* **2019**, 481, 852-859.

[71] Y. Tian, Y. L. An, C. L. Wei, B. J. Xi, S. L. L. Xiong, J. K. Feng, Y. T. Qian. *ACS Nano,* **2019**, 13, 11676-11685.

[72] A. Xia, X. Pu, Y. Tao, H. Liu, Y. Wang. *Appl. Surf. Sci.,* **2019**, 481, 852-859.

[73] Z. Zhou, Y. Zhang, P. Chen, Y. Wu, H. Yang, H. Ding, Y. Zhang, Z. Wang, X. Du, N. Liu. *Chem. Eng. Sci.,* **2019**, 194, 142-147.

[74] L. Dong, W. Yang, W. Yang, H. Tian, Y. Huang, X. Wang, C. Xu, C. Wang, F. Kang, G. Wang. *Chem. Eng. J.,* **2020**, 384, 123355.

[75] M. Liu, X. Pu, Z. Cong, Z. Liu, T. Liu, Y. Chen, J. Fu, W. Hu, Z. L. Wang. *ACS Appl. Mater. Interfaces,* **2019**, 11, 5095-5106.

[76] Y. Zeng, X. Zhang, R. Qin, X. Liu, P. Fang, D. Zheng, Y. Tong, X. Lu. *Adv. Mater.,* **2019**, 31, 1903675.

[77] W. Xu, K. Zhao, W. Huo, Y. Wang, G. Yao, X. Gu, H. Cheng, L. Mai, C. Hu, X. Wang. *Nano Energy,* **2019**, 62, 275-281.

[78] C. Li, X. Shi, S. Liang, X. Ma, M. Han, X. Wu, J. Zhou. *Chem. Eng. J.,* **2020**, 379, 122248.

[79] R. Zhang, X. R. Chen, X. Chen, X. B. Cheng, X. Q. Zhang, C. Yan, Q. Zhang. *Angew. Chem. Int. Ed.,* **2017**, 129, 7872-7876.

[80] A. Pei, G. Zheng, F. Shi, Y. Li, Y. Cui. *Nano Lett.,* **2017**, 17, 1132-1139.

[81] Q. Zhang, J. Luan, Y. Tang, X. Ji, H. Wang. *Angew. Chem. Int. Ed.,* **2020**, 59, 13180-13191.

[82] Z. Zhao, J. Zhao, Z. Hu, J. Li, J. Li, Y. Zhang, C. Wang, G. Cui. *Energy & Environmental Science,* **2019**, 12, 1938-1949.

[83] A. Mitha, A. Z. Yazdi, M. Ahmed, P. Chen. *ChemElectroChem,* **2018**, 5, 2409-2418.

[84] Z. M. Zhao, J. W. Zhao, Z. L. Hu, J. D. Li, J. J. Li, Y. J. Zhang, C. Wang, G. L. Cui. *Energy Environ. Sci.,* **2019**, 12, 1938-1949.

[85] J. J. Zhang, L. H. Mao, Z. G. Xia, M. Q. Fan, Y. P. Deng, Z. W. Chen. *Adv. Funct. Mater.,* **2024**, 35, 2412547.

[86] T. C. Liu, Y. Xu, H. Y. Fang, L. Chen, J. D. Ying, M. Guo, Y. Q. Wang, Q. Shen, X. S. Wang, Y. Wang, Z. X. Yu. *J. Mater. Chem. A,* **2024**, 12, 2283-2293.

[87] T. Foroozan, V. Yurkiv, S. Sharifi-Asl, R. Rojaee, F. Mashayek, R. Shahbazian-Yassar. *Acs Applied Materials & Interfaces,* **2019**, 11, 44077-44089.

[88] J. Y. Gong, J. H. Ying, X. J. Jia, R. H. Su, T. S. Zhao, H. R. Jiang. *Chem. Eng. J.,* **2024**, 480, 148267.

[89] D. Yuan, J. Zhao, H. Ren, Y. Chen, R. Chua, E. T. J. Jie, Y. Cai, E. Edison, W. Manalastas Jr, M. W. Wong. *Angew. Chem. Int. Ed.,* **2021**, 133, 7289-7295.

[90] C. Lu, H. Zhou. *Sci. Bull.,* **2020**, 65, 1524-1526.

[91] R. F. Ashton, M. T. Hepworth. *Corrosion,* **1968**, 24, 50-53.

[92] D. Abayarathna, E. Hale, T. O'Keefe, Y.-M. Wang, D. Radovic. *Corros Sci,* **1991**, 32, 755-768.

[93] J. Zheng, Q. Zhao, T. Tang, J. Yin, C. D. Quilty, G. D. Renderos, X. Liu, Y. Deng, L. Wang, D. C. Bock. *Science,* **2019**, 366, 645-648.

[94] Y. Yang, C. Liu, Z. Lv, H. Yang, Y. Zhang, M. Ye, L. Chen, J. Zhao, C. C. Li. *Adv. Mater.,* **2021**, 33, 2007388.

[95] W. Zhao, I. P. Perera, H. S. Khanna, Y. Dang, M. Li, L. F. Posada, H. Tan, S. L. Suib. *ACS A.E.M,* **2024**, 7, 1172-1181.

[96] H. He, H. Tong, X. Song, X. Song, J. Liu. *J. Mater. Chem. A* **2020**, 8, 7836-7846.

[97] D. Xie, Z. W. Wang, Z. Y. Gu, W. Y. Diao, F. Y. Tao, C. Liu, H. Z. Sun, X. L. Wu, J. W. Wang, J. P. Zhang. *Adv. Funct. Mater.,* **2022**, 32, 2204066.

[98] L. Chen, Y. Ruan, G. Zhang, Q. Wei, Y. Jiang, T. Xiong, P. He, W. Yang, M. Yan, Q. An. *Chem. Mater.,* **2019**, 31, 699-706.

[99] Y. Zhang, Z. Cao, S. Liu, Z. Du, Y. Cui, J. Gu, Y. Shi, B. Li, S. Yang. *Adv. Energy Mater.,* **2022**, 12, 2103979.

[100] S. Xie, Y. Li, X. Li, Y. Zhou, Z. Dang, J. Rong, L. Dong. *Nano-Micro Lett.,* **2022**, 14, 39.

[101] F. Perera. *Int. J. Environ. Res. Public Health.,* **2018**, 15, 16.

[102] H. Kim, J. Hong, K.-Y. Park, H. Kim, S.-W. Kim, K. Kang. *Chem. Rev.,* **2014**, 114, 11788-11827.

[103] J. Hao, X. Li, X. Zeng, D. Li, J. Mao, Z. Guo. *Energy Environ. Sci.,* **2020**, 13, 3917-3949.

[104] Z. L. Xu, G. Yoon, K. Y. Park, H. Park, O. Tamwattana, S. J. Kim, W. M. Seong, K. Kang. *Nat. Commun.,* **2019**, 10, 2598.

[105] L. E. Blanc, D. Kundu, L. F. Nazar. *Joule,* **2020**, 4, 771-799.

[106] Y. Shao, F. Shen, Y. Shao. *ChemElectroChem,* **2021**, 8, 484-491.

[107] D. Kundu, B. D. Adams, V. Duffort, S. H. Vajargah, L. F. Nazar. *Nat. Energy.,* **2016**, 1, 16119.

[108] D. Han, Z. Wang, H. Lu, H. Li, C. Cui, Z. Zhang, R. Sun, C. Geng, Q. Liang, X. Guo. *Adv. Energy Mater.,* **2022**, 12, 2102982.

[109] F. Tao, Y. Liu, X. Ren, J. Wang, Y. Zhou, Y. Miao, F. Ren, S. Wei, J. Ma. *J. Energy Chem.,* **2022**, 66, 397-412.

[110] F. Tao, Y. Liu, X. Y. Ren, J. Wang, Y. Z. Zhou, Y. J. Miao, F. Z. Ren, S. Z. Wei, J. M. Ma. *J. Energy Chem.,* **2022**, 66, 397-412.

[111] J. X. Zheng, Y. Deng, W. Z. Li, J. F. Yin, P. J. West, T. Tang, X. Tong, D. C. Bock, S. Jin, Q. Zhao, R. Garcia-Mendez, K. J. Takeuchi, E. S. Takeuchi, A. C. Marschilok, L. A. Archer. *Sci. Adv.,* **2022**, 8, eabq6321.

[112] R. P. Oates, J. Murawski, C. Hor, X. Y. Shen, D. J. Weber, M. Oezaslan, M. S. P. Shaffer, I. E. L. Stephens. *J. Electrochem. Soc.,* **2022**, 169, 054516.

[113] A. Naveed, A. Ali, T. Rasheed, X. Wang, P. Ye, X. Li, Y. Zhou, S. Mingru, Y. Liu. *J. Power Sources,* **2022**, 525, 231122.

[114] M. Okubo, A. Sugahara, S. Kajiyama, A. Yamada. *Acc. Chem. Res.,* **2018**, 51, 591-599.

[115] A. VahidMohammadi, J. Rosen, Y. Gogotsi. *Science,* **2021**, 372, eabf1581.

[116] P. Zhang, Y. Peng, Q. Zhu, R. A. Soomro, N. Sun, B. Xu. *Energy Environ. Mater,* **2022**, 14, 16320-16329.

[117] X. Zhan, C. Si, J. Zhou, Z. Sun. *Nanoscale Horiz.,* **2020**, 5, 235-258.

[118] Y. Tian, Y. An, C. Wei, B. Xi, S. Xiong, J. Feng, Y. Qian. *ACS Nano.,* **2019**, 13, 11676-11685.

[119] X. He, J. Wu, Y. Chen, L. Zhang, X. Sheng. *Appl. Surf. Sci.,* **2022**, 603, 154455.

[120] C. L. Xie, Y. H. Li, Q. Wang, D. Sun, Y. G. Tang, H. Y. Wang. *Carbon Energy,* **2020**, 2,

540-560.

[121] J. Z. Yang, B. S. Yin, Y. Sun, H. G. Pan, W. P. Sun, B. H. Jia, S. W. Zhang, T. Y. Ma. *Nano-Micro Lett.,* **2022**, 14, 1-47.

[122] J. Q. Qin, H. D. Shi, K. Huang, P. F. Lu, P. C. Wen, F. F. Xing, B. Yang, M. Ye, Y. Yu, Z. S. Wu. *Nat. Commun.,* **2021**, 12, 5786.

[123] M. K. Peng, L. Wang, L. B. Li, X. N. Tang, B. Y. Huang, T. Hu, K. Yuan, Y. W. Chen. *Adv. Funct. Mater.,* **2022**, 32, 2109524.

[124] M. Peng, L. Wang, L. Li, X. Tang, B. Huang, T. Hu, K. Yuan, Y. Chen. *Adv. Funct. Mater.,* **2022**, 32, 2109524.

[125] G. S. Lee, T. Yun, H. Kim, I. H. Kim, J. Choi, S. H. Lee, H. J. Lee, H. S. Hwang, J. G. Kim, D. W. Kim, H. M. Lee, C. M. Koo, S. O. Kim. *ACS Nano,* **2020**, 14, 11722-11732.

[126] N. K. Manninen, R. E. Galindo, N. Benito, N. M. Figueiredo, A. Cavaleiro, C. Palacio, S. Carvalho. *J. Phys. Appl. Phys.,* **2011**, 44, 375501.

[127] T. H. Park, S. Yu, M. Koo, H. Kim, E. H. Kim, J.-E. Park, B. Ok, B. Kim, S. H. Noh, C. Park. *ACS Nano,* **2019**, 13, 6835-6844.

[128] J. Liebscher. *Eur. J. Org. Chem.,* **2019**, 2019, 4976-4994.

[129] T. Li, B. Ding, J. Wang, Z. Y. Qin, J. F. S. Fernando, Y. Bando, A. K. Nanjundan, Y. V. Kaneti, D. Golberg, Y. Yamauchi. *ACS Appl. Mater. Interfaces,* **2020**, 12, 14993-15001.

[130] M. H. Ryou, D. J. Lee, J. N. Lee, Y. M. Lee, J. K. Park, J. W. Choi. *Adv. Energy Mater.,* **2012**, 2, 645-650.

[131] Y. Zuo, K. Wang, P. Pei, M. Wei, X. Liu, Y. Xiao, P. Zhang. *Mater. Today Energy,* **2021**, 20, 100692.

[132] T. C. Liu, J. Hong, J. L. Wang, Y. Xu, Y. Wang. *Energy Storage Mater.,* **2022**, 45, 1074-1083.

[133] T. Chang, O. A. Moses, C. Tian, H. Wang, L. Song, G. Zhao. *Adv. Sci.,* **2021**, 8, 2003387.

[134] Y. Z. Zhang, Z. J. Cao, S. J. Liu, Z. G. Du, Y. L. Cui, J. N. Gu, Y. Z. Shi, B. Li, S. B. Yang. *Adv. Energy Mater.,* **2022**, 12, 2103979.

[135] X. T. Zhang, J. X. Li, D. Y. Liu, M. K. Liu, T. S. Zhou, K. W. Qi, L. Shi, Y. C. Zhu, Y. T. Qian. *Energy Environ. Sci.,* **2021**, 14, 3120-3129.

[136] X. Y. Luo, W. C. Peng, Y. Li, F. B. Zhang, X. B. Fan. *Green Energy Environ.,* **2022**, 7, 858-899.

[137] L. T. Ma, S. M. Chen, N. Li, Z. X. Liu, Z. J. Tang, J. A. Zapien, S. M. Chen, J. Fan, C. Y. Zhi. *Adv. Mater.,* **2020**, 32, 1908121.

[138] C.-H. Huang, Y.-L. Jan, W.-J. Chuang, P.-T. Lu. *Crystals,* **2018**, 8, 343.

[139] Z. L. Li, S. Ganapathy, Y. L. Xu, Z. Zhou, M. Sarilar, M. Wagemaker. *Adv. Energy Mater.,* **2019**, 9, 1900237.

[140] C. B.V. *Handbook of Monochromatic Xps Spectra*; Commercially Pure Binary Oxides, XPS International Inc., 754 Leona Lane, *Mountain View*, 1999.

[141] T. Eom, J. H. Y. Lee, S. Lee, B. Ozlu, S. Kim, D. C. Martin, B. S. Shim. *ACS Appl. Polym. Mater.,* **2022**, 4, 5319-5329.

[142] X. D. Zhu, X. Y. Li, M. L. K. Essandoh, J. Tan, Z. Y. Cao, X. Zhang, P. Dong, P. M. Ajayan, M. X. Ye, J. F. Shen. *Energy Storage Mater.,* **2022**, 50, 243-251.

[143] D. Kundu, S. H. Vajargah, L. Wan, B. Adams, D. Prendergast, L. F. Nazar. *Energy Environ. Sci.,* **2018**, 11, 881-892.

[144] J. Cao, D. D. Zhang, Y. L. Yue, R. Chanajaree, S. M. Wang, J. T. Han, X. Y. Zhang, J. Q. Qin, Y. H. Huang. *Nano Energy,* **2022**, 93, 106839.

[145] J. Li, Q. Lin, Z. Zheng, L. Cao, W. Lv, Y. Chen. *ACS Appl. Mater. Interfaces,* **2022**, 14, 12323-12330.

[146] X. S. Xie, S. Q. Liang, J. W. Gao, S. Guo, J. B. Guo, C. Wang, G. Y. Xu, X. W. Wu, G. Chen, J. Zhou. *Energy Environ. Sci.,* **2020**, 13, 503-510.

[147] A. Naveed, H. Yang, J. Yang, Y. Nuli, J. Wang. *Angew. Chem. Int. Ed.,* **2019**, 58, 2760-2764.

[148] C. Shen, X. Li, N. Li, K. Y. Xie, J. G. Wang, X. R. Liu, B. Q. Wei. *ACS Appl. Mater. Interfaces,* **2018**, 10, 25446-25453.

[149] P. C. Liang, J. Yi, X. Y. Liu, K. Wu, Z. Wang, J. Cui, Y. Y. Liu, Y. G. Wang, Y. Y. Xia, J. J. Zhang. *Adv. Funct. Mater.,* **2020**, 30, 1908528.

[150] W. J. Fan, F. Liu, Y. Liu, Z. X. Wu, L. L. Wang, Y. Zhang, Q. H. Huang, L. J. Fu, Y. P. Wu. *Chem. Commun.,* **2020**, 56, 2039-2042.

[151] K. N. Zhao, C. X. Wang, Y. H. Yu, M. Y. Yan, Q. L. Wei, P. He, Y. F. Dong, Z. Y. Zhang, X. D. Wang, L. Q. Mai. *Adv. Mater. Interfaces,* **2018**, 5, 7.

[152] N. N. Zhang, S. Huang, Z. S. Yuan, J. C. Zhu, Z. F. Zhao, Z. Q. Niu. *Angew. Chem.-Int. Edit.,* **2021**, 60, 2861-2865.

[153] X. Zhu, X. Li, M. L. K. Essandoh, J. Tan, Z. Cao, X. Zhang, P. Dong, P. M. Ajayan, M. Ye, J. Shen. *Energy Storage Mater.,* **2022**, 50, 243-251.

[154] C. Li, S. Jin, L. A. Archer, L. F. Nazar. *Joule,* **2022**, 6, 1733-1738.

[155] X. F. Zhang, L. Zhang, X. Y. Jia, W. Song, Y. C. Liu. *Nano-Micro Lett.,* **2024**, 16, 75.

[156] M. Zhou, Y. Chen, G. Z. Fang, S. Q. Liang. *Energy Storage Mater.,* **2022**, 45, 618-646.

[157] C. H. Nie, G. L. Wang, D. D. Wang, M. Y. Wang, X. R. Gao, Z. C. Bai, N. A. Wang, J. Yang, Z. Xing, S. X. Dou. *Adv. Energy Mater.,* **2023**, 13, 2300606.

[158] Y. C. Liang, D. T. Ma, N. Zhao, Y. Y. Wang, M. Yang, J. B. Ruan, G. H. Yang, H. W. Mi, C. X. He, P. X. Zhang. *Adv. Funct. Mater.,* **2022**, 32, 2112936.

[159] M. Fayette, H. J. Chang, X. L. Li, D. Reed. *ACS Energy Lett.,* **2022**, 7, 1888-1895.

[160] R. Z. Zhao, X. S. Dong, P. Liang, H. P. Li, T. S. Zhang, W. H. Zhou, B. Y. Wang, Z. D. Yang, X. Wang, L. P. Wang, Z. H. Sun, F. X. Bu, Z. W. Zhao, W. Li, D. Y. Zhao, D. L. Chao. *Adv. Mater.,* **2023**, 35, 2209288.

[161] S. Chen, Y. F. Xia, R. Zeng, Z. Luo, X. X. Wu, X. Z. Hu, J. Lu, E. Gazit, H. G. Pan, Z. J. Hong, M. Yan, K. Tao, Y. Z. Jiang. *Science Advances,* **2024**, 10, eadn2265.

[162] H. M. You, Y. Yoon, J. Ko, J. Back, H. Kwon, J. W. Han, K. Kim. *Langmuir,* **2024**, 40, 1961-1970.

[163] X. H. Zheng, Z. C. Liu, J. F. Sun, R. H. Luo, K. Xu, M. Y. Si, J. Kang, Y. Yuan, S. Liu, T. Ahmad, T. L. Jiang, N. Chen, M. M. Wang, Y. Xu, M. Chuai, Z. X. Zhu, Q. Peng, Y. H. Meng, K. Zhang, W. P. Wang, W. Chen. *Nat. Commun.,* **2023**, 14, 76.

[164] H. C. Tao, Z. H. Hou, L. L. Zhang, X. L. Yang, L. Z. Fan. *Chem. Eng. J.,* **2022**, 450, 138048.

[165] P. Xiong, Y. Kang, H. Yuan, Q. Liu, S. H. Baek, J. M. Park, Q. Dou, X. Han, W. S. Jang, S. J. Kwon, Y. M. Kim, W. Li, H. S. Park. *Appl. Phys. Rev.,* **2022**, 9, 011401.

[166] A. Balandin. *Advances in catalysis,* **1969**, 19, 1-210.

[167] F. Wan, X. Z. Zhou, Y. Lu, Z. Q. Niu, J. Chen. *ACS Energy Lett.,* **2020**, 5, 3569-3590.

[168] C. C. Fan, W. J. Meng, D. S. Li, L. Jiang. *Energy Storage Mater.,* **2023**, 56, 468-477.

[169] D. Koo, B. Kwon, J. Lee, K. T. Lee. *Chem. Commun.,* **2019**, 55, 9637-9640.

[170] Q. Li, A. Chen, D. H. Wang, Y. W. Zhao, X. Q. Wang, X. Jin, B. Xiong, C. Y. Zhi. *Nat. Commun.,* **2022**, 13, 3699.

[171] H. Ooka, J. Huang, K. S. Exner. *Front. Energy Res.,* **2021**, 9, 654460.

[172] T. T. Wang, P. J. Wang, L. Pan, Z. X. He, L. Dai, L. Wang, S. D. Liu, S. C. Jun, B. A. Lu, S. Q. Liang, J. Zhou. *Adv. Energy Mater.,* **2023**, 13, 2203523.

[173] S. B. Wang, Q. Ran, R. Q. Yao, H. Shi, Z. Wen, M. Zhao, X. Y. Lang, Q. Jiang. *Nat Commun.,* **2020**, 11, 1634.

[174] J. X. Zheng, Z. H. Huang, Y. Zeng, W. Q. Liu, B. B. Wei, Z. B. Qi, Z. C. Wang, C. Xia, H. F. Liang. *Nano Lett.,* **2022**, 22, 1017-1023.

[175] N. N. Zhang, S. Huang, Z. S. Yuan, J. C. Zhu, Z. F. Zhao, Z. Q. Niu. *Angew. Chem. Int. Ed.,* **2021**, 60, 2861-2865.

[176] W. Han, L. Xiong, M. Wang, W. Seo, Y. Liu, S. T. U. Din, W. Yang, G. Liu. *Chem. Eng. J.,* **2022**, 442, 136247.

[177] D. Xie, Z. W. Wang, Z. Y. Gu, W. Y. Diao, F. Y. Tao, C. Liu, H. Z. Sun, X. L. Wu, J. W. Wang, J. P. Zhang. *Adv. Funct. Mater.,* **2022**, 32, 2204066.

[178] Y. Z. Wang, T. C. Guo, J. Yin, Z. N. Tian, Y. C. Ma, Z. X. Liu, Y. P. Zhu, H. N. Alshareef. *Adv. Mater.,* **2022**, 34, 2106937.

[179] T. T. Wang, P. J. Wang, L. Pan, Z. X. He, L. Dai, L. Wang, S. D. Liu, S. C. Jun, B. A. Lu, S. Q. Liang, J. Zhou. *Adv. Energy Mater.,* **2023**, 13, 2203523.

[180] Q. L. Zhang, J. R. Liang, M. C. Li, J. L. Qin, Y. J. Zhao, L. T. Ren, W. Liu, C. K. Yang,

X. M. Sun. *Chem. Eng. J.,* **2023**, 474, 145981.

[181] J. N. Hao, B. Li, X. L. Li, X. H. Zeng, S. L. Zhang, F. H. Yang, S. L. Liu, D. Li, C. Wu, Z. P. Guo. *Adv. Mater.,* **2020**, 32, 2003021.

[182] Y. Yang, C. Y. Liu, Z. H. Lv, H. Yang, Y. F. Zhang, M. H. Ye, L. B. Chen, J. B. Zhao, C. C. Li. *Adv. Mater.,* **2021**, 33, 2007388.

[183] X. Wang, J. P. Meng, X. G. Lin, Y. D. Yang, S. Zhou, Y. P. Wang, A. Q. Pan. *Adv. Funct. Mater.,* **2021**, 31, 2106114.

[184] H. Yu, D. Chen, Q. Li, C. Yan, Z. Jiang, L. Zhou, W. Wei, J. Ma, X. Ji, Y. Chen. *Adv. Energy Mater.,* **2023**, 13, 2300550.

[185] M. Fu, Q. Zhao, K. Long, Q. Li, G. c. Kuang, L. Zhou, W. Wei, X. Ji, L. Chen, Y. Chen. *Adv. Funct. Mater.,* **2024**, 34, 2311680.

[186] H. M. Yu, D. P. Chen, X. Y. Ni, P. Qing, C. S. Yan, W. F. Wei, J. M. Ma, X. B. Ji, Y. J. Chen, L. B. Chen. *Energy Environ. Sci.,* **2023**, 16, 2684-2695.

[187] A. S. Rosen, S. Vijay, K. A. Persson. *Chem. Sci.,* **2023**, 14, 1503-1511.

[188] H. J. Tian, G. X. Feng, Q. Wang, Z. Li, W. Zhang, M. Lucero, Z. X. Feng, Z. L. Wang, Y. N. Zhang, C. Zhen, M. Gu, X. N. Shan, Y. Yang. *Nat. Commun.,* **2022**, 13, 7922.

[189] G. M. Hobold, K. H. Kim, B. M. Gallant. *Energy Environ. Sci.,* **2023**, 16, 2247-2261.

[190] C. Heubner, S. Maletti, O. Lohrberg, T. Lein, T. Liebmann, A. Nickol, M. Schneider, A. Michaelis. *Batteries Supercaps,* **2021**, 4, 1310-1322.

[191] K. H. Chen, K. N. Wood, E. Kazyak, W. S. LePage, A. L. Davis, A. J. Sanchez, N. P. Dasgupta. *J. Mater. Chem. A,* **2017**, 5, 11671-11681.

[192] K. Xu, X. H. Zheng, R. H. Luo, J. F. Sun, Y. R. Ma, N. Chen, M. M. Wang, L. Song, Q.

B. Zhao, W. Chen. *Mater. Today Energy,* **2023**, 34, 101284.

[193] S. Y. Xie, Y. Li, X. Li, Y. J. Zhou, Z. Q. Dang, J. H. Rong, L. B. Dong. *Nano-Micro Lett.,* **2022**, 14, 39.

[194] X. F. Zhang, L. Zhang, X. Y. Jia, W. Song, Y. C. Liu. *Nano-Micro Lett.,* **2024**, 16, 45.

[195] Z. Q. Wei, S. X. Wang, D. D. Li, S. Yang, S. D. Guo, G. M. Qu, Y. H. Yang, H. F. Li. *Energy Environ. Sci.,* **2024**, 17, 5440-5450.

[196] S. Y. Li, J. Fu, G. X. Miao, S. P. Wang, W. Y. Zhao, Z. C. Wu, Y. J. Zhang, X. W. Yang. *Adv. Mater.,* **2021**, 33, 2008424.

[197] Q. Zhang, J. Y. Luan, X. B. Huang, Q. Wang, D. Sun, Y. G. Tang, X. B. Ji, H. Y. Wang. *Nat. Commun.,* **2020**, 11, 3961.

[198] H. Yu, Y. X. Zeng, N. W. Li, D. Y. Luan, L. Yu, X. W. Lou. *Sci. Adv.,* **2022**, 8, eabm5766.

[199] Y. X. Zeng, X. Y. Zhang, R. F. Qin, X. Q. Liu, P. P. Fang, D. Z. Zheng, Y. X. Tong, X. H. Lu. *Adv. Mater.,* **2019**, 31, 1903675.

[200] G. H. Zhang, X. N. Zhang, H. Z. Liu, J. H. Li, Y. Q. Chen, H. G. Duan. *Adv. Energy Mater.,* **2021**, 11, 2003927.

[201] L. Hong, X. M. Wu, L. Y. Wang, M. Zhong, P. Y. Zhang, L. S. Jiang, W. Huang, Y. L. Wang, K. X. Wang, J. S. Chen. *ACS Nano,* **2022**, 16, 6906-6915.

[202] X. T. Zhang, J. X. Li, Y. F. Liu, B. A. Lu, S. Q. Liang, J. Zhou. *Nat. Commun.,* **2024**, 15, 2735.

[203] Z. C. Qi, T. Xiong, Z. G. Yu, F. B. Meng, B. Chen, H. Xiao, J. M. Xue. *J. Power Sources,* **2023**, 558, 232628.

[204] X. Guo, S. C. Zhang, H. Hong, S. X. Wang, J. X. Zhu, C. Y. Zhi. *iScience,* **2025**, 28,

111751.

[205] Z. Qi, T. Xiong, Z. G. Yu, F. Meng, B. Chen, H. Xiao, J. Xue. *J. Power Sources,* **2023**, 558, 232628.

[206] B. E. Hawkins, D. E. Turney, R. J. Messinger, A. M. Kiss, G. G. Yadav, S. Banerjee, T. N. Lambert. *Adv. Energy Mater.,* **2022**, 12, 2103294.

[207] J. Y. Yu, Z. Z. Song, Q. Qi, X. B. Hui, Y. Y. Ma, F. Y. Chen, K. Qi, Q. Meng, R. J. Li, L. Y. C. Zhuang, K. C. Chan, Z. B. Chen, B. Y. Xia, Z. L. Xu. *Angew. Chem. Int. Ed.,* **2025**, 64, e202423236.

[208] Y. Gao, N. T. Yang, F. Bu, Q. H. Cao, J. Pu, Y. X. Wang, T. Meng, J. P. Chen, W. B. Zhao, C. Guan. *Energy Environ. Sci.,* **2024**, 17, 1894-1903.

[209] R. T. Guo, X. Liu, K. Ni, F. J. Xia, H. Z. Zhang, Y. Liu, X. Z. Dai, L. T. Shi, X. P. Wang, C. H. Han, L. Q. Mai, C. J. Niu. *Energy Environ. Sci.,* **2025**, 18, 2353-2364.

[210] Y. D. Hu, P. Y. Wang, M. Z. Li, Z. X. Liu, S. Q. Liang, G. Z. Fang. *Energy Environ. Sci.,* **2024**, 17, 8078-8093.

[211] Z. F. Yang, C. Hu, Q. Zhang, T. Q. Wu, C. L. Xie, H. Wang, Y. G. Tang, X. B. Ji, H. Y. Wang. *Angew. Chem. Int. Ed.,* **2023**, 62, e20230817.

[212] K. L. Guan, L. Tao, R. Yang, H. N. Zhang, N. Z. Wang, H. Z. Wan, J. Cui, J. Zhang, H. B. Wang, H. Wang. *Advanced Energy Materials,* **2022**, 12, 2103557.

[213] Y. F. Guo, C. Luo, M. F. Yang, H. R. Wang, W. W. Ma, K. K. Hu, L. Li, F. Wu, R. J. Chen. *Angew. Chem. Int. Ed.,* **2024**, 63, e202406597.

[214] L. Zhang, Y. Dai, C. Li, Y. Z. Dang, R. G. Zheng, Z. Y. Wang, Y. Wang, Y. H. Cui, H. Arandiyan, Z. P. Shao, H. Y. Sun, Q. C. Zhuang, Y. G. Liu. *Energy Storage Mater.,* **2024**, 69,

103378.

[215] Q. Li, A. Chen, D. H. Wang, Z. X. Pe, C. Y. Zhi. *Joule,* **2022**, 6, 273-279.

[216] H. B. He, J. Liu. *J. Mater. Chem. A,* **2020**, 8, 22100-22110.

[217] A. S. Chen, C. Y. Zhao, J. Z. Gao, Z. K. Guo, X. Y. Lu, J. C. Zhang, Z. P. Liu, M. Wang, N. N. Liu, L. S. Fan, Y. Zhang, N. Q. Zhang. *Energy Environ. Sci.,* **2023**, 16, 275-284.

[218] J. J. Dong, H. L. Peng, J. Wang, C. G. Wang, D. D. Wang, N. A. Wang, W. L. Fan, X. C. Jiang, J. Yang, Y. T. Qian. *Energy Storage Mater.,* **2023**, 54, 875-884.

[219] Z. Meng, Y. C. Jiao, P. Y. Wu. *Angew. Chem. Int. Ed.,* **2023**, 62, e202307271.

[220] Y. Xiang, Y. Zhong, P. P. Tan, L. Y. Zhou, G. J. Yin, H. W. Pan, X. Li, Y. Z. Jiang, M. W. Xu, X. Zhang. *Small,* **2023**, 19, 2302161.

[221] W. Xu, X. Liao, W. Xu, K. Zhao, G. Yao, Q. Wu. *Adv. Energy Mater.,* **2023**, 13, 2300283.

[222] H. Yan, S. Li, Y. Nan, S. Yang, B. Li. *Adv. Energy Mater.,* **2021**, 11, 2100186.

[223] J. F. Parker, C. N. Chervin, I. R. Pala, M. Machler, M. F. Burz, J. W. Long, D. R. Rolison. *Science,* **2017**, 356, 414-417.